https://doi.org/10.5194/egusphere-2026-4027
Preprint. Discussion started: 6 August 2026

Mechanical interaction of geometrically linked cracks and faults

Ludovico Manna[1*], Matteo Maino[1, 2], Leonardo Casini[3], Marcin Dabrowski[4]

[1] Department of Earth and Environmental Sciences, University of Pavia, Pavia, Italy

[2] Institute of Geosciences and Earth Resources of Pavia, C.N.R., Pavia, Italy

[3] Department of Chemical, Physical, Mathematical and Natural Sciences, University of Sassari, Sassari, Italy

[4] Computational Geology Laboratory, Polish Geological Institute – National Research Institute, Wrocław, Poland

Corresponding author:

Ludovico Manna, ludovico.manna01@universitadipavia.it

ORCiD:

Ludovico Manna: https://orcid.org/0009-0003-7952-157X

Matteo Maino: https://orcid.org/0000-0001-8766-8027

Leonardo Casini: https://orcid.org/0000-0002-6157-1865

Marcin Dabrowski: https://orcid.org/0000-0003-0309-8050

Abstract

Understanding how macroscopic fractures develop from interacting cracks is essential for describing brittle deformation in upper-crustal rocks. Although empirical failure criteria successfully describe fracturing in laboratory experiments, they do not explain how microcracks distributed within deforming rocks interact,

https://doi.org/10.5194/egusphere-2026-4027
Preprint. Discussion started: 6 August 2026

coalesce and organize into through-going fracture networks. In this study, we examine how the geometrical distribution of pre-existing cracks controls the local stress perturbations that may influence fracture formation. We use two-dimensional Finite Element Method-based numerical simulations to quantify the elastic stress field around isolated cracks, *en echelon* crack arrays and randomly distributed crack systems undergoing simple shear. The results show that crack orientation, and spacing strongly control the distribution of reduced compression, effective cohesion, and localized strain around crack tips, and determine whether local stress perturbations may promote or inhibit crack linkage. Favorably arranged crack arrays produce overlapping lobes of reduced compression and local principal stress trajectories that effectively connect neighboring crack tips, defining potential linkage paths oblique to the far-field maximum principal stress. These findings suggest that shear fractures primarily develop from the overlap of tensile stress perturbation regions around pre-existing cracks rather than being controlled solely by the far-field stress or the geometry of mode I cracks formed during early stages of deformation. In highly anisotropic crack configurations, the distribution forces shear fracture evolution and fault configurations along limited paths. Conversely, rocks with isotropic crack distributions tend to preferentially activate *en echelon* arrays oriented approximately at 30° relative to the far-field maximum principal stress, as predicted by the Coulomb criterion. This research demonstrates that the distribution, and orientation of the pre-existing cracks exert a first-order control over the mechanical evolution of shear fractures and faults, as well as the impact of crustal and hydrostatic pressure variations on the conditions for failure and crack opening in upper-crustal rocks.

1. Introduction

Brittle deformation is common in the upper crust, where both temperature and effective pressure are low. It typically occurs when stress exceeds rock strength (Segall and Pollard, 1983; Reches and Lockner, 1994; Price, 1966), although brittle creep may operate under subcritical stress levels (Brantut et al., 2013). Under brittle conditions, deformation is commonly accommodated by the development and propagation of fractures (Sibson, 1986). Fractures are generally classified into two main categories: shear fractures or faults,

https://doi.org/10.5194/egusphere-2026-4027
Preprint. Discussion started: 6 August 2026

dominated by offset parallel to the walls, and extension fractures or joints, with opening displacement perpendicular to their plane (e.g., Bahat, 1991; Bahat et al., 2005; Van der Pluijm and Marshak, 2004; Atkinson, 2015; Scholz, 2019). While the terms shear and extension fractures are primarily used by experimentalists to identify laboratory-scale structural discontinuities, the terms faults and joints are commonly used to describe the corresponding large-scale structures observed in the field (Fossen, 2016). Understanding the mechanisms of joint and fault formation is fundamental for predicting the mechanical evolution and permeability structure of the upper crust (e.g., Sibson, 1977; Handy et al., 2007; Wibberley et al., 2008). In particular, faults may act either as conduits or barriers to fluid transport, depending on their geometry (Chester and Logan, 1986; Hooper, 1991; Hickman et al., 1995; Caine et al., 1996; Gudmundsson et al., 2001). Moreover, since faults govern strain localization in the upper crust and play a key role in earthquake nucleation, understanding their formation is essential for seismic risk assessment (Thatcher, 1975; Carlson et al., 1994; Harris, 2017).

1.1 Introducing microcracks

Early theoretical calculations of tensile strength based on the breaking of crystal lattice yielded values several orders of magnitude higher than those required to fracture rock samples in laboratory tests (Orowan, 1949; Scholz, 2019 and references therein). This apparent paradox was resolved by recognizing that polycrystalline materials like rocks are largely inhomogeneous and, in particular, contain numerous microscopic, randomly distributed structural flaws such as pores and grain boundaries (Griffith, 1920; 1924). When these flaws have a planar geometry and lengths of millimeters or less, they are referred to as microcracks (Anders et al., 2014). Microcracks are typically saturated with liquids or gases (Brace et al., 1968; Zoback and Byerlee, 1976). Due to a prominent effect of stress concentration around favorably oriented cracks, failure can initiate locally and develop into a macroscopic fracture even if the far-field stress remains below the strength of the intact rock (Griffith, 1924; Pollard and Fletcher, 2005). When multiple cracks are closely spaced within a rock, they may interact, either promoting or inhibiting crack growth depending on their relative orientation and separation

(Nabavi et al., 2017; Healy et al., 2006; McBeck et al., 2021). Therefore, microcracks play a crucial role in controlling fracture nucleation and growth and, consequently, the macroscopic strength of rocks (Brace and Bombolakis, 1963; Vermilye and Scholz, 1998; Paterson and Wong, 2005; Healy et al., 2006; Anders et al., 2014; McBeck et al., 2023). The evolution and mechanical interaction of microcracks, however, strongly depend on the stress conditions, particularly on confining pressure (e.g., Brace et al., 1966).

At low confining pressures, multiple tensile (mode I) cracks and resulting macroscopic extension fractures parallel to the direction of $\vec{\sigma}_1^\infty$ accommodate most of the deformation, promoting axial splitting in uniaxial experiments (Tapponnier and Brace, 1976; Martel et al., 1988; Twiss and Moores, 1992; Bobet and Einstein, 1998; Moir et al., 2010; Renard et al., 2017; Renard et al., 2018; McBeck et al., 2021). As lithostatic pressure increases with depth, cracks tend to close and undergo frictional sliding along their contacting walls, marking the transition toward the formation of shear rather than extension fractures (Ramsey and Chester, 2004; Liu et al., 2022). At higher confining pressures, shear mode (mode II) cracks dominate microscopic brittle deformation, especially when the deforming rock is on the verge of macroscopic failure, as indicated by studies based on acoustic emission analysis (e.g., Stanchits et al., 2006; Graham et al., 2010).

1.2 Extension fractures

Laboratory observations show that extension fractures develop parallel to the far-field maximum principal stress $\vec{\sigma}_1^\infty$ (e.g., Lawn, 1993; Pollard and Fletcher, 2005; Jaeger et al., 2009). Extension fractures may form through the growth of mode I cracks (Tapponnier and Brace, 1976; Martel et al., 1988; Bobet and Einstein, 1998) under effective tensile stress, a condition that is rare and confined to the upper part of the Earth's crust (e.g., Nur, 1982). Under a tensile stress regime, mode I cracks can propagate in-plane, a process that has been extensively studied, both for subcritical (Obreimoff, 1930; Liebowitz, 1968; Evans, 1972; Atkinson, 1982) and dynamic conditions (Cook and Erdogan, 1972; Siegmund et al., 1997).

However, extension fractures can also form and propagate under remotely applied compressive stresses (Griffith, 1920; 1924; Nemat-Nasser and Horii, 1982). Theoretical (e.g., Hoek and Bieniawski, 1965; Maugis, 1992) and experimental (Orowan, 1949; Brace and Bombolakis, 1963) studies have shown that tensile

https://doi.org/10.5194/egusphere-2026-4027
Preprint. Discussion started: 6 August 2026

stresses may locally develop and concentrate at the tips of microcracks oriented obliquely to the direction of the major in-plane principal stress $\vec{\sigma}_1^{\infty}$. As a result of the local tension conditions in the microcrack tip zone, new cracks can initiate and develop into the so-called wing cracks (e.g., Ashby and Hallam, 1986; Cannon et al., 1990), which typically grow stably along curved paths, until their growth ceases once they align with the direction of $\vec{\sigma}_1^{\infty}$ (Brace and Bombolakis, 1963; Pollard and Fletcher, 2005; Price, 1966). The linkage of multiple oblique cracks through wing crack propagation can ultimately lead to the formation of macroscopic extension fractures parallel to $\vec{\sigma}_1^{\infty}$ (Nicholson and Pollard, 1985). The development of extension fractures under a compressive regime dominates brittle deformation at low confining pressure (up to ≈10 MPa), for which pore fluid pressure can sufficiently reduce the effective pressure (Paterson and Wong, 2005) and promote crack opening as well as lead to substantial tensile stress concentrations at the tips of favorably oriented cracks.

1.3 Shear fractures

Unlike opening cracks, shear cracks cannot grow through in-plane propagation (Brace and Bombolakis, 1963; Erdogan and Sih, 1963; Liu, 1985). The linkage of wing cracks developing from the tips of multiple pre-existing cracks has been suggested as the most plausible mechanism leading to crack coalescence into larger, system-spanning shear fractures (e.g., Brace et al., 1966; Scholz, 1968; Hallbauer et al., 1973; Horii and Nemat-Nasser, 1985; Petit and Barquins, 1988; Vermilye and Scholz, 1998; Healy et al., 2006; Renard et al., 2018; McBeck et al., 2026). Experimental observations indicate that shear fractures typically form in conjugate pairs and are oriented obliquely (typically at about 30-35°) relative to the direction of $\vec{\sigma}_1^{\infty}$ (e.g., Lawn, 1993; Pollard and Fletcher, 2005; Jaeger et al., 2009). These observations are formalized mathematically in the Mohr-Coulomb failure criterion, which applies in compressive stress regimes and adopts a linear relationship between shear and normal stress on a critically stressed failure plane. It is valid at high confining pressures (>3–4 MPa; Twiss and Moores, 1992) and predicts shear fractures oriented at approximately θ≈±30° to $\vec{\sigma}_1^{\infty}$. These angles are related to a material parameter, the angle of internal friction ϕ, which experimentally yields values of ≈30-35°, according to the following relation:

https://doi.org/10.5194/egusphere-2026-4027
Preprint. Discussion started: 6 August 2026

$$\theta = \frac{\pi}{4} - \frac{\phi}{2} \quad (1)$$

A fundamental theoretical attempt to describe the formation of shear fractures through the coalescence of mode I cracks, based on earlier theoretical studies (e.g., Brace et al., 1966; Scholz, 1968) was proposed by Reches and Lockner (1994). They suggested that in an intact rock without pre-existing flaws, tensile cracks form parallel to $\vec{\sigma}_1^{\infty}$ during the early stages of loading, and that tensile stress lobes elongating at approximately ±30° relative to the crack direction emanate from their tips. When cracks cluster at separations comparable to their lengths, the overlap of high local tensile stress regions between adjacent crack tips promotes the development of fracture arrays oriented at ≈±30° relative to $\vec{\sigma}_1^{\infty}$, thereby providing a fundamental theoretical explanation for the observed macroscopic internal friction angles.

A related study was conducted by Vermilye and Scholz (1998), who interpreted fault growth as the progressive development of tensile microfractures around propagating shear fracture tips. According to this study, brittle shear fractures do not advance simply as in-plane mode II cracks. Instead, fault-tip stress perturbations promote the nucleation, interaction and coalescence of mode I microfractures within the process zone. The accumulation of these tensile cracks provides a mechanism by which distributed microcracking can localize into a macroscopic shear fracture.

Healy et al. (2006) extended this concept proposing a three-dimensional model in which brittle shear fractures form through the interaction and coalescence of many tensile microcracks. Their results show that the geometry of the microcrack population and the elastic stress perturbations around individual cracks can control the position and orientation of the resulting shear fracture surfaces. Their model suggests that tensile crack interaction can generate more complex fracture patterns than those predicted by classical Mohr–Coulomb theory, particularly under three-dimensional stress states. This highlights the importance of considering not only the far-field stress, but also the geometry, orientation and spacing of interacting cracks.

However, all these models mainly consider the interaction between cracks parallel to $\vec{\sigma}_1^{\infty}$ and neglect differently oriented pre-existing flaws. Consequently, only a single possible orientation for shear fractures formed through crack coalescence is predicted, which contradicts field and laboratory observations

https://doi.org/10.5194/egusphere-2026-4027
Preprint. Discussion started: 6 August 2026

(Anderson, 1905; Peacock and Sanderson, 1995; Bobet and Einstein, 1998; Tang et al., 2001; Wong et al., 2001; Kim et al., 2003; 2004; Crider and Peacock, 2004; Chang et al., 2015; Zhou et al., 2015; Kanaya and Hirth, 2024). Moreover, recent work has shown that if clustered, interacting cracks parallel to $\vec{\sigma}_1^{\infty}$ are arranged in alternating left-right steps, the stress interference at their tips should favor the formation of new fractures parallel to $\vec{\sigma}_1^{\infty}$, rather than oblique shear fractures (McBeck et al., 2023). This underlines the importance of considering simplified but realistic geometrical arrangements of interacting cracks in brittle rocks, such as *en echelon* cracks.

1.4 *En echelon* cracks

En echelon arrays, consisting of closely-spaced cracks in a stepped configuration, are common features in upper-crustal rocks (Cosgrove and Engelder, 2004; de Joussineau and Aydin, 2007; Peacock et al., 2016; Sanderson and Peacock, 2019; Beach, 1975; Segall and Pollard, 1980; La Pointe and Hudson, 1985; Rothery, 1988). The regular geometry of *en echelon* crack arrays enables inferences regarding the tectonic stress during their formation (Roering, 1968; Jackson, 1991; Wiltschko et al., 2009). These interpretations mostly derive from field observations of vein and crack arrays mapped at the outcrop scale (Roering, 1968; Beach, 1975; Jackson, 1991; Peacock and Sanderson, 1995; Willemse, 1997; Kelly et al., 1998; Wiltschko et al., 2009). In shear zones, *en echelon* arrays progressively rotate and stretch during deformation producing sigmoidal vein geometries that serve as valuable kinematic indicators (Bons et al., 2012; Lisle, 2013). Nevertheless, kinematic analysis is not sufficient to explain the spacing, lengths, and geometry of *en echelon* cracks (Pollard and Fletcher, 2005; Seyum and Pollard, 2016). In fact, the magnitude of the near-tip stress of each crack in the array is perturbed by the neighboring cracks, to a degree which mainly depends on their overlap and orientation (Pollard et al., 1982; Du and Aydin, 1991; Mandal, 1995; Chau and Wang, 2001; Seyum and Pollard, 2016), and the interactions may lead to curved crack trajectories (Pollard et al., 1982; Du and Aydin, 1991; Chau and Wang, 2001; Seyum and Pollard, 2016). In *en echelon* crack arrays, bridges of wall rock experience highly concentrated strains and may ultimately fail, leading to the linkage of neighboring cracks (Nicholson and Pollard, 1985). These regular crack systems may therefore act as precursory structures to faults (de Joussineau and Aydin, 2007; Crider, 2015). Both in crystalline and sedimentary rocks, faults typically

https://doi.org/10.5194/egusphere-2026-4027
Preprint. Discussion started: 6 August 2026

develop through the linkage of pre-existing features such as cracks, mineral cleavages, veins and other types of discontinuities (Shipton and Cowie, 2001; de Joussineau and Aydin, 2007; Faulkner et al., 2010). This indicates that regular crack arrays play a crucial role in the incipient stages of macroscopic fault zone development (Kranz, 1979; Wong, 1982; Gottschalk et al., 1990; Moore and Lockner, 1995; Crider, 2015). Conversely, propagating faults control the growth and linkage of cracks in a highly-stressed process zone ahead of the fault tip (Granier, 1985; Cox and Scholz, 1988; Lockner et al., 1991; Moore and Lockner, 1995; Reches and Lockner, 1994).

1.5 Step faults

Step faults may be viewed as macro-scale analogues to the *en echelon* crack arrays observed at the micro-scale (Segall and Pollard, 1983; Pollard and Segall, 1987; Kim and Sanderson, 2005; Aydin et al., 2006; de Joussineau and Aydin, 2007; Nabavi et al., 2017; Faulkner et al., 2010). Although strike-slip faults may be observed as linear, continuous features at large scales, they typically consist of multiple, subparallel segments, separated by step-like bridges (Childs et al., 2009; Faulkner et al., 2010). These bridging segments interact producing local stress field perturbations, similarly to systems of *en echelon* cracks (Segall and Pollard, 1983; Pollard and Segall, 1987; Dasgupta and Mukherjee, 2017). The geometry of the steps is the key parameter governing fault segment interactions. Depending on the orientation of the fault segments relative to the direction of regional tectonic compression, extensional or contractional stepovers develop respectively for the step sense matching or opposite to the sense of fault slip (Biddle and Christie-Blick, 1985; Christie-Blick and Biddle, 1985; Woodcock and Fischer, 1986; Sylvester, 1988; Woodcock and Schubert, 1994; Westaway, 1995; Cunningham and Mann, 2007; Mann, 2007). Field, analytical, analogue, and numerical studies consistently demonstrated that the evolution of step faults depends on the overlap between fault segments, and their relative orientation (Rodgers, 1980; Mann et al., 1983; Pollard and Segall, 1987; Bürgmann and Pollard, 1994; Willemse et al., 1996; Kim and Sanderson, 2005; Li et al., 2009; Kristensen et al., 2008; Childs et al., 2009; Strijker et al., 2013; Nevitt et al., 2014; Nevitt, 2015).

https://doi.org/10.5194/egusphere-2026-4027
Preprint. Discussion started: 6 August 2026

1.6 Linear Elastic Fracture Mechanics

The mechanical description of crack growth is commonly addressed using Linear Elastic Fracture Mechanics (LEFM), which derives conceptually from Griffith's energy balance approach (Griffith, 1920; Atkinson, 2015 and references therein). Loading a crack embedded in an elastic medium results in stress diverging as $r^{-\frac{1}{2}}$ in the near-tip zone, where r is the distance from the crack tip (Irwin, 1957; Rice, 1968; Pollard and Fletcher, 2005; Atkinson, 2015; Price, 1966). To address the problem of this unphysical stress singularity inherent in linear elastic models of cracks, the stress intensity factor K is introduced in LEFM, a mode-sensitive quantity which remains finite and depends on loading conditions and crack geometry. Specifically, the near-tip stress tensor components σ_{ij} are defined as follows:

$$\sigma_{ij} = \frac{K f_{ij}(\vartheta)}{\sqrt{2\pi r}} \quad (2)$$

The indices i and j identify spatial components, σ_{ij} are stress tensor components at a (small) distance r from the tip and f_{ij} are angular functions of the polar angle ϑ measured from the crack tip. The mode I stress intensity factor K_I, for example, is:

$$K_I = \frac{\sigma_{ij}\sqrt{2\pi r}}{f_{ij}(\vartheta)} \quad (3)$$

In the framework of LEFM, crack propagation intensifies when K approaches the fracture toughness (K_C), a material parameter typically ranging between 1 and 3 $MPa \cdot m^{\frac{1}{2}}$ for rocks. In this case, crack growth is stable and is referred to as subcritical crack growth, where propagation velocity is proportional to the stress intensity factor (Brantut et al., 2013). If the stress intensity factor exceeds the fracture toughness, unstable growth occurs at velocities often comparable to the speed of sound in the medium (Irwin and de Wit, 1983, Atkinson, 2015).

https://doi.org/10.5194/egusphere-2026-4027
Preprint. Discussion started: 6 August 2026

1.7 Macroscopic failure criteria

Although LEFM provides a solid framework for the description of stress near a crack tip and subsequent crack growth, an alternative approach relies on macroscopic failure criteria to predict fracture nucleation. In this framework, a fracture is assumed to initiate when stresses satisfy a given mathematical criterion. The simplest is the tensile criterion, according to which failure occurs when the minimum principal stress exceeds tensile strength T_0 of the rock, that is:

$$\sigma_2 \leq -T_0 \quad (4)$$

The Mohr-Coulomb criterion, which relates the shear strength τ of a rock to the applied normal stress σ_n, is expressed as:

$$\tau = C + \mu\sigma_n = C + \tan\phi\,\sigma_n \quad (5)$$

where C is the cohesion, μ is the coefficient of internal friction and ϕ is the angle of internal friction of the rock. As introduced above, the Mohr–Coulomb criterion predicts failure on planes oriented at $\theta = \frac{\pi}{4} - \frac{\phi}{2}$ with respect to $\vec{\sigma}_1^{\infty}$. If the resolved shear stress on such planes exceeds the shear strength for the given stress state, a fracture is expected to nucleate. Both these macroscopic failure criteria allow the identification of potential fracture nucleation sites and fault orientations (e.g., Pollard and Fletcher, 2005; Jaeger et al., 2009; Fossen, 2016). Macroscopic failure criteria have been widely applied to large-scale geological problems, such as the prediction of dyke propagation paths and fault geometries (e.g., Pollard and Fletcher, 2005; Gudmundsson, 2011). If the rock contains a distribution of pre-existing flaws, these approaches can also be relevant at the meso- and micro-scale, where the failure criteria can be interpreted as an effective description of the collective behavior of interacting microcracks (e.g., Ashby and Sammis, 1990; Amitrano, 2003; Schmittbuhl et al., 2003).

1.8 Outlook

In this study, we examine the tendency for fracture formation in regions of reduced stress (potential effective tensile stress) due to the presence of preexisting cracks, under the hypothesis that large fracture networks, including faults, are controlled by stress perturbations generated by pre-existing cracks during elastic deformation. Using Finite Element Method-based simulations, we analyze stress and strain fields in systems containing *en echelon* and randomly distributed cracks, relying on macroscopic failure criteria to evaluate potential favorable conditions for brittle deformation.

2. Methods

We used a Matlab-based implementation of the Finite Element Method (FEM) for plane strain 2D linear elasticity to study the stress and strain fields around pre-existing cracks approximated by elliptical voids. We developed two different types of models: i) *en echelon* arrays of aligned cracks with varying separation and orientation relative to the major in-plane principal stress $\vec{\sigma}_1^{\infty}$, and ii) randomly located cracks with variable length and degree of their alignment. The second-order shape functions (interpolation space in the FEM formulation) (Hughes, 2003; Bathe, 2006) combined with unstructured, body-fitting triangular meshes allow for highly accurate solutions even in complex computational domains, including systems with internal discontinuities (Moës et al., 1999; Dabrowski et al., 2008; Chen, 2012; Zhao et al., 2018). We used six-node triangular elements, and the computational meshes were generated using the Triangle mesh generator, developed by Shewchuk (1996, 2002). The linear elastic models are formally scale-independent, and the spatial dimensions are non-dimensionalized using the crack length. The models and the obtained stress and strain fields can be upscaled or downscaled to the scale of interest in a straightforward manner (e.g., Goodier & Hodge Jr., 2016). Other studies (e.g., Chinnery, 1963; Resor and Flodin, 2010; Atkinson, 2015; Castelletto et al., 2017; Menegoni et al., 2024) have demonstrated that linear elastic models can be useful for evaluating stress conditions that are critical for localizing permanent strains, thereby contributing to the formation of geological structures at various scales, from small to large. All reported results are normalized: each stress and strain component locally computed using FEM is normalized by the representative background value, i.e., the principal value of stress and strain that would be attained in the absence of cracks.

The approach of using highly-elongated elliptical voids to approximate friction-less cracks in rocks has been adopted in multiple studies (e.g., Yang and Soh, 2002; Bertoldi et al., 2007; Niu et al., 2024). An analytical solution for the displacement and stress fields around an isolated and highly elongated elliptical void embedded in a medium undergoing homogeneous elastic deformation in the far field (e.g., Pollard, 1987; Meguid et al., 1991; Schmid and Podladchikov, 2003; Jaeger et al., 2009) provides valuable insights into the slip magnitude and stress concentration around friction-less cracks as well as an opportunity to test numerical codes. Although representing two-dimensional slit cracks as ellipses rather than sharp lines using the approach of contact elements (Johnson, 1987) is convenient for numerical modeling, caution must still be exercised against element interpenetration and overlap.

Slit cracks offer a versatile way to study different types of discontinuous structures within rocks. For example, multiple colinear cracks may represent rough fractures, which can be modeled as a series of thin voids representing the alternation of non-contacting wall patches and contact asperities (Feng and Gross, 2000; Myer, 2000). Models with randomly distributed but aligned cracks can be used to simulate mechanical effects related to bedding and schistosity in sedimentary and metamorphic rocks, respectively (e.g., Nicksiar and Martin, 2013). Similarly, a distribution of microscopic cracks that are randomly positioned and oriented can be used to model grain boundaries in granular and polycrystalline media or the random distribution of crystal lattice defects in undeformed magmatic rocks (Graham et al., 2010; Fattaruso et al., 2022).

The number of points used for discretizing input ellipses in each model was selected to optimize geometric resolution while avoiding excessive computational cost. The nodal coordinates are defined using an elliptic parametrization, such that all points on the ellipse satisfy $x_i = a\cos\eta_i$ and $y_i = b\sin\eta_i$, with $\eta_i = i * 2\pi/1000$, $i = 0, 1, 2, \dots, N_{ell} - 1$. In the *en echelon* crack models, which contain a limited number of cracks (10), the perimeter of each crack is discretized using N_{ell}=1000 nodal points. In contrast, in the randomly distributed crack models, which include a much larger number of cracks (500), each crack perimeter is

https://doi.org/10.5194/egusphere-2026-4027
Preprint. Discussion started: 6 August 2026

discretized using N_{ell}=360 nodes to limit computational cost while preserving sufficient numerical resolution (computational meshes exceeding 5 million triangular elements were used for the random models). The aspect ratio of the ellipses is set to 10000 in the *en echelon* crack models and to 1000 in the randomly distributed crack models.

3. Model setup

The structural geology and rock mechanics sign convention, in which compressive stresses are taken as positive, is adopted in this study. All the studied strain and stress distributions are obtained from two-dimensional, plane-strain numerical simulations, where the xy plane represents the modelled cross-section. The local magnitudes of the major and minor in-plane principal stresses are denoted as σ_1 and σ_2, respectively. Under plane strain conditions, the out-of-plane principal stress typically acts as the intermediate component, its magnitude depending on the Poisson's ratio and the nature of the far-field loading. The vectors indicating the local orientation of the principal stresses are labeled as $\vec{\sigma}_1$ and $\vec{\sigma}_2$, respectively.

We use P^{∞} to denote the far-field hydrostatic stress, which represents the action of the lithostatic pressure due to overburden weight. Because our objective is to investigate the stress perturbation due to the presence of cracks, the results are expressed in terms of reduced stresses, which are calculated by subtracting the lithostatic pressure, thus representing the non-lithostatic stress component. We assume sufficiently high pore fluid pressure in the cracks to maintain their aperture open. For pore fluid pressure approaching the lithostatic pressure, the reduced stress would directly correspond to the effective stress. The key stress quantity analyzed in each model is the reduced and normalized magnitude of the minor in-plane principal stress $\tilde{\sigma}_2 = (\sigma_2 - P^{\infty})/(\sigma_1^{\infty} - P^{\infty})$. Negative values of $\tilde{\sigma}_2$ indicate sublithostatic stress states, or potentially effective tension, whereas positive values correspond to elevated compression, with the least compressive principal stress locally exceeding the background lithostatic load. For crack systems that produce strongly negative local values of $\tilde{\sigma}_2$, we identify regions where the minor in-plane principal stress potentially approaches or exceeds the tensile strength of the rock. Therefore, it may lead to nucleation and growth of

https://doi.org/10.5194/egusphere-2026-4027
Preprint. Discussion started: 6 August 2026

tensional fractures, facilitating the coalescence of the pre-existing cracks or faults into either macroscopic fractures or larger-scale faults, respectively.

To evaluate the potential conditions for nucleation of shear fractures under different confining pressures P^{∞} and pore fluid pressures P_f, we rely on the following formulation of the Mohr-Coulomb macroscopic failure criterion:

$$\tau_m - (\sigma_m - P^{\infty})\sin(\phi) = (P^{\infty} - P_f)\sin(\phi) + C\cos(\phi) \quad (6)$$

where C is the cohesion, ϕ is the angle of internal friction (which is set to 35° in our models, a value consistent with experimental results for unweathered rocks),

$$\tau_m = \frac{\sigma_1 - \sigma_2}{2} \quad (7)$$

is half the local in-plane differential stress and

$$\sigma_m = \frac{\sigma_1 + \sigma_2}{2} \quad (8)$$

is the local in-plane mean stress. The calculation of the in-plane principal stress components allows us to evaluate the confining pressure- and fluid pressure-dependent normalized effective cohesion $\tilde{C}$, defined as:

$$\tilde{C} = [C + (P^{\infty} - P_f)\tan(\phi)]/(\sigma_1^{\infty} - P^{\infty}) = [\frac{\tau_m}{\cos(\phi)} - (\sigma_m - P^{\infty})\tan(\phi)]/(\sigma_1^{\infty} - P^{\infty}) \quad (9)$$

$\tilde{C}$ represents the stress threshold for activating shear fractures between pre-existing cracks for specific values of P^{∞} and P_f. If the rock cohesion for a specific stress state is not sufficiently high for the local value of $\tilde{C}$, conjugate shear fractures may develop at angles

$$\theta = \pm\left(\frac{\pi}{4} - \frac{\phi}{2}\right) \quad (10)$$

with respect to the local orientation of $\vec{\sigma}_1$.

We also analyze the distributions of the normalized first invariant of the strain tensor $\bar{I}_1 = tr(\bar{\boldsymbol{\varepsilon}})$ and of the normalized shear strain $\bar{\varepsilon}_{xy}$, to estimate local volumetric deformation and the local amplification of the far-

https://doi.org/10.5194/egusphere-2026-4027
Preprint. Discussion started: 6 August 2026

field shear deformation, respectively. Positive values of $\bar{I}_1$ represent dilation, whereas negative values represent contraction.

In all models, right-lateral simple shear deformation is applied to the system by prescribing a shear strain value of $\gamma = 10^{-3}$. Any initial stress variations due to the difference between the pore fluid pressure in the cracks and background lithostatic pressure are discarded. The material parameters representing the bulk properties of the rock undergoing elastic deformation were taken from Tal et al. (2018), which focuses on the nucleation of earthquakes on rough faults. The Young's modulus of the rock is set to 60 GPa, and the Poisson's ratio is 0.25. These values fall within the range of experimentally determined elastic parameters for the most common crustal rocks such as granite and limestone. The simple shear loading generates a 48 MPa differential stress $\sigma_1^\infty - \sigma_2^\infty$ in the far field, which corresponds to a 24 MPa deviatoric stress $\sigma_1^\infty - P^\infty$ that is equal to the reduced major in-plane principal stress. Nevertheless, the obtained stress magnitudes are presented as normalized and reduced stresses that are independent, for the analyzed setup, from the specific value of the Young's modulus and Poisson's ratio.

Elastic deformation and stress distributions in rocks with pre-existing cracks are simulated for two distinct geometries: i) *en echelon* array of cracks, and ii) randomly distributed cracks.

3.1 *En echelon* cracks

In the first model, we examine *en echelon* systems consisting of multiple slit cracks of the same orientation ϑ and a constant half-length a, whose centers are aligned along a straight line inclined at an angle φ. All angles are measured counterclockwise from the horizontal orientation that corresponds to the shear direction. The crack array is placed in the center of a square computational domain, with the side length L set to $1000 \cdot a$ to minimize the boundary effects (Fig. 1A). 10 cracks are used to form the array and the stress distributions are analyzed around the centrally located ellipses that are expected to approximate conditions for periodic *en echelon* crack arrays.

https://doi.org/10.5194/egusphere-2026-4027
Preprint. Discussion started: 6 August 2026

We performed four sets of parametric experiments. In the first set, we varied the normalized projected overlap d, defined as:

$$d = \frac{2a}{D|\cos(\varphi - \vartheta)|} \quad (11)$$

where D denotes the distance between the centers of adjacent cracks. In this set of experiments, we considered models with d ranging from 0.5 (minimum crack overlap, corresponding to a configuration, in which the projection of the distance between adjacent crack centers onto the crack direction equals twice the crack length) to 1.2 (Fig. 1A). A configuration with d=1 corresponds to the case where the projections of the crack tips onto the crack direction coincide into a single point, or, equivalently, the projected distance between the crack centers along the same direction equals the crack length. The crack orientation ϑ is set to 0°, and two symmetrical configurations with φ=±15° are considered. In the second set of experiments, we varied the inclination φ of the crack array over the ranges -45° to -5° (Fig. 1A) and, symmetrically, 5°-45°, including the collinear crack configuration (φ=0°). In this set, ϑ was fixed at 0° and d was set to 0.8 (Fig. 1A). In the third set, we varied the crack orientation ϑ between -45° and -5° and, symmetrically, 5°–45°, with φ fixed at 0° and d set to 0.9 (Fig. 1A). In the fourth set of experiments, we varied d between 0.8 (underlapping cracks) and 1.2 (overlapping cracks), and simultaneously varied ϑ and φ such that their difference ranged between -30° and 30° in 10° steps, while φ was set to 0°, ±10°, ±20° (Fig. 1B).

https://doi.org/10.5194/egusphere-2026-4027
Preprint. Discussion started: 6 August 2026

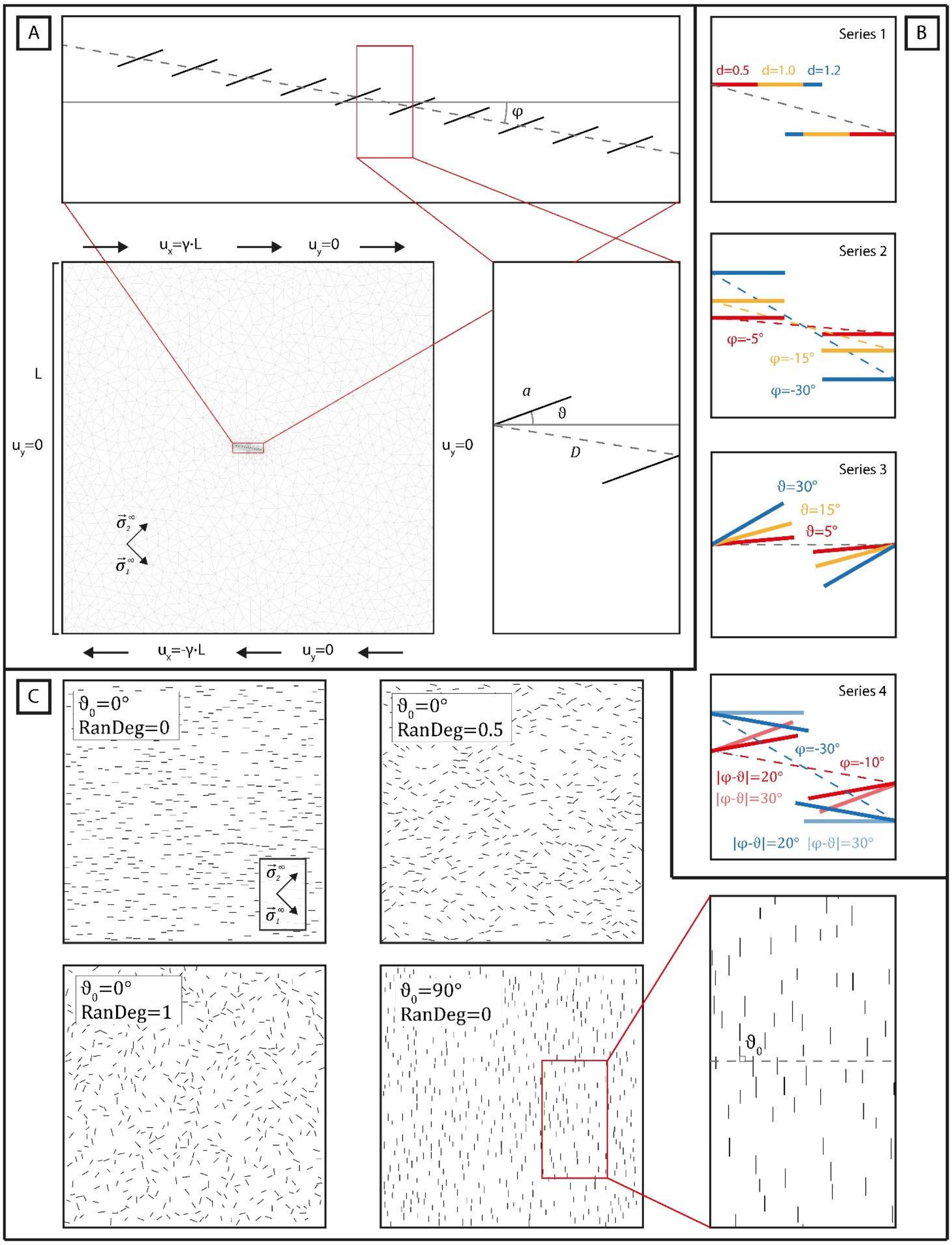

Fig. 1: (a) A square domain of width L with an embedded array of *en echelon* cracks in the center subject to simple shear. In the first inset, the *en echelon* array of 10 cracks is illustrated. The array forms an angle φ

https://doi.org/10.5194/egusphere-2026-4027
Preprint. Discussion started: 6 August 2026

with respect to the horizontal shear direction. In the second inset, the two central cracks in the system are shown. The crack half-length is a, the distance between their centers is D and their orientation with respect to the horizontal is ϑ. (b) Representative examples of model setups for the four sets of simulations with *en echelon* cracks. Series 1: variable projected overlap d. Series 2: variable array inclination φ. Series 3: variable crack orientation ϑ. Series 4: variable φ and $\varphi - \vartheta$. (c) Representative configurations of models with randomly distributed slit cracks. Both the crack orientation ϑ_0 and the degree of randomness in crack orientation $RanDeg$ are varied. In the inset, a local crack distribution in the model with $\vartheta_0 = 90°$ and $RanDeg = 0$ is illustrated.

3.2 Randomly distributed cracks

The second set of models consists of multiple, non-intercepting slit cracks of varying sizes, with crack half-length a randomly drawn from a uniform distribution spanning $0.5 \cdot 10^{-3}L$ to $10^{-2}L$. The cracks are randomly distributed in terms of their positions, and their orientations are either randomized to a varying degree or fully aligned (Fig. 1C). In the numerical procedure used for generating the input model, the crack length and orientation are first drawn from their distributions, and then the crack is randomly placed within the domain. If it overlaps with the previously added cracks or intersects the domain boundaries, a new random position for its center is generated. This random sequential addition procedure may result in a bias between the intended and resulting distribution of crack lengths and orientations. For example, longer cracks are more likely to be rejected due to the non-intersection constraint. However, this effect is expected to be small for the studied crack densities. The geometry of several model realizations is illustrated in Fig. 1C.

The geometrical distribution of cracks within the domain is controlled using two key parameters:

- Crack orientation
- Degree of randomness in crack orientation

When the degree of randomness is set to zero, all cracks are aligned in a specific direction, representing rocks with a strong structural anisotropy due to crack alignment. Slightly increasing the randomness parameter

https://doi.org/10.5194/egusphere-2026-4027
Preprint. Discussion started: 6 August 2026

results in a more realistic model, in which cracks maintain a preferred orientation but include small random deviations from the mean orientation (Fig. 1C). A maximum randomness value of 1 represents a fractured rock with an isotropic structure (Fig. 1C), or, if crack density is low, an intact rock with randomly distributed microcracks. The relationship between the trial orientation of the i-th crack ϑ_i and the degree of randomness of the system $RanDeg$ is described by the following equation:

$$\vartheta_i = \vartheta_0 + RanDeg \cdot \left(\pi \cdot RN_i(0{,}1) - \frac{\pi}{2}\right) \quad (12)$$

In this equation, ϑ_0 is a fixed angle representing the orientation of all cracks when $RanDeg$ is set to zero. $RN_i(0{,}1)$ is a random number uniformly distributed in the interval (0,1), varying for each crack. If $RanDeg$=0, all cracks are aligned and $\vartheta_i = \vartheta_0$ for all i (Fig. 1C). As $RanDeg$ increases, the angles ϑ_i are allowed to vary randomly within an interval proportional to $RanDeg$. When $RanDeg$=1, each ϑ_i is a completely random angle in the range $\left[\vartheta_0 - \frac{\pi}{2}, \vartheta_0 + \frac{\pi}{2}\right]$ (Fig. 1C).

Different models were analyzed by keeping the domain area fixed while varying the number of cracks. Here, we present the results for the models with the highest crack concentration, which embedded 500 cracks (Fig. 1C). The average crack non-dimensional density P_{22} of these models can be defined as (Sanderson and Nixon, 2015):

$$P_{22} = \frac{N l_c^2}{L^2} \quad (13)$$

where l_c is the mean crack length:

$$l_c = \frac{\sum_{i=1}^{N} 2a_i}{N} \quad (14)$$

and L is the length of a side of the domain. P_{22}=0.055. Despite the low crack density, mechanical interactions between cracks remain significant, meaning they cannot be treated as isolated cracks (Kachanov, 1992).

We analyzed a total of 16 configurations, varying the angle ϑ_0 over 0°, 45°, 90°, and -45° and $RanDeg$ over the values 0, 0.25, 0.5 and 1. The four configurations with $RanDeg$=1, although differing in details, effectively produce the same model, therefore the number of unique configurations is 13.

https://doi.org/10.5194/egusphere-2026-4027
Preprint. Discussion started: 6 August 2026

4. Results

In this section, we present the results of our numerical simulations. The first subsection revisits the classical results for isolated cracks. The second subsection presents the results for models with *en echelon* systems of slit cracks. In the third subsection, we examine the results of models with randomly distributed cracks.

4.1 Isolated crack

In this subsection, we examine the classical results on the distribution of the least compressive stress around an isolated crack with characteristic orientations, such as mode I and II. To isolate from the effects due to lithostatic load and the specific level of simple shear, we use the reduced and normalized minor in-plane principal stress magnitude $\tilde{\sigma}_2$. The results show that the mode I and II crack orientations generate distinctively shaped regions of reduced compressive stress, which may potentially correspond to sites of effective tensile stress.

Fig. 2 illustrates the stress distributions around two classes of cracks defined by their orientation: cracks parallel (Fig. 2A) and oblique (Fig. 2B) to the principal stress axes. Cracks parallel to the direction of major in-plane far-field principal stress $\vec{\sigma}_1^\infty$ are referred to as mode I cracks, whereas those oriented at ±45° are named mode II cracks.

For mode I cracks, regions of reduced compression, which could be associated with effectively tensile stress, preferentially occur in two symmetrical lobes emanating from the crack tips at a low angle relative to the crack elongation. For cracks oriented perpendicular to $\vec{\sigma}_1^\infty$, the effective tensile stress may develop within an elliptically shaped region located around their centers (Fig. 2A). Elevated compressive stresses concentrate within elliptically shaped regions enveloping mode I cracks and occur in single lobes radiating from the tips along the crack direction for cracks oriented perpendicular to $\vec{\sigma}_1^\infty$ (Fig. 2A).

In mode I orientation, we observe that the local trajectories of the major in-plane principal stress $\vec{\sigma}_1$ fan out around the crack tips, then progressively reconverge toward the crack and align with its major axis next to it (Fig. 2A). In contrast, for cracks oriented perpendicular to the far-field compression direction $\vec{\sigma}_1^{\infty}$, the local trajectories of the major in-plane principal stress curve toward the tips, while remaining perpendicular to the crack around its center (Fig. 2A).

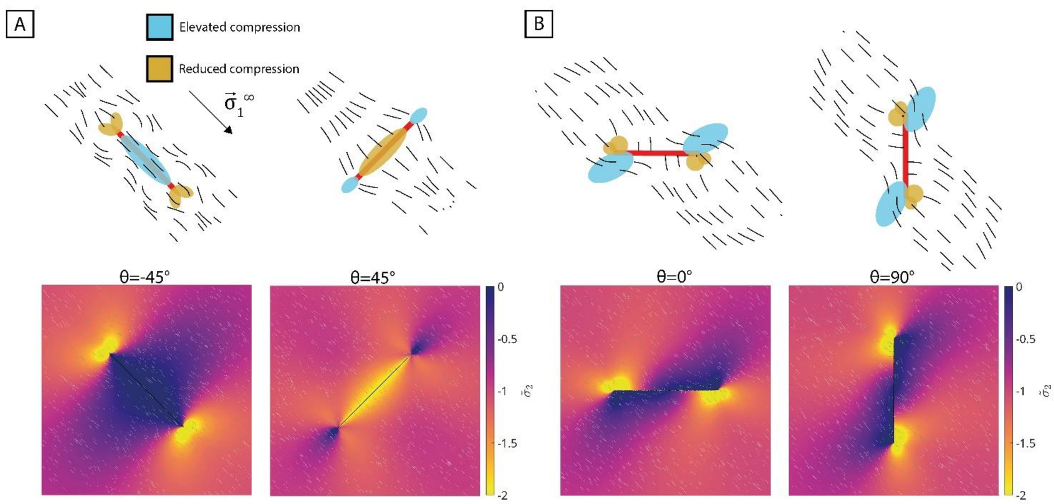

Fig. 2: Top: Schematic illustrations of reduced and elevated compressive stress regions around isolated mode I and II cracks. Bottom: Distributions of the minor in-plane principal stress magnitude $\tilde{\sigma}_2$. White and black lines indicate the local trajectories of the major in-plane principal stress $\vec{\sigma}_1$. (a) Mode I cracks oriented at 0° and 90° (left to right) relative to the direction of the far-field principal compression axis $\vec{\sigma}_1^{\infty}$. (b) Mode II cracks oriented at ±45° relative to $\vec{\sigma}_1^{\infty}$.

For the mode II cracks, which are oriented at ±45° relative to the direction of $\vec{\sigma}_1^{\infty}$, zones of reduced compression or potentially effective tensile stress concentrate in paired lobes that emanate asymmetrically from each crack tip towards the compressive quadrants of the far-field simple shear. The lobes are oriented at ±30° relative to $\vec{\sigma}_1^{\infty}$, forming angles of -15° and -75° relative to the crack direction (Fig. 2B). Single lobe-

https://doi.org/10.5194/egusphere-2026-4027
Preprint. Discussion started: 6 August 2026

shaped regions of elevated compression, elongating at approximately ±90° relative to $\vec{\sigma}_1^{\infty}$ are located on the opposite sides of the tip regions (Fig. 2B).

The local trajectories of the major in-plane principal stress $\vec{\sigma}_1$ deflect around mode II cracks, aligning with their orientation in the regions characterized by elevated compression and becoming sub-perpendicular to the crack in areas of reduced compressive stress (Fig. 2B).

4.2 *En echelon* cracks

In this set of numerical experiments, we simulated stress perturbation around *en echelon* crack arrays to assess their mechanical interaction and tendency for reactivation and potential coalescence into macroscopic fractures. We again focus on the reduced and normalized minor in-plane principal stress magnitude $\tilde{\sigma}_2$. We analyze how (i) the spatial distribution of potential sites of effective tension $\tilde{\sigma}_2$ (i.e., negative $\tilde{\sigma}_2$ values) between neighboring cracks, (ii) the local trajectories of the major in-plane principal stress $\vec{\sigma}_1$, (iii) normalized effective cohesion $\tilde{C}$, (iv) the normalized first invariant of the strain tensor $\bar{I}_1$ and (v) the normalized shear strain $\bar{\varepsilon}_{xy}$ vary as a function of three geometric parameters: the projected overlap between neighboring cracks along their major axis d, the orientation of the *en echelon* array φ with respect to the far-field major compression direction, and the inclination of the cracks ϑ within the array.

Fig. 3A illustrates the distribution of $\tilde{\sigma}_2$ around horizontally oriented cracks (ϑ=0°; mode II with respect to simple shear applied in the far field) arranged in arrays oriented at φ=±15° relative to the shearing direction, for d values ranging from 0.5 to 1.1. Equivalent configurations for vertical mode II cracks and for collinear model-oriented cracks are shown in Fig. A1. A systematic trend emerges: for φ=-15°, decreasing crack separation promotes the coalescence of reduced compressive stress zones between the crack tips (Fig. 3A). In contrast, for φ=15°, regions of elevated compression merge and amplify between adjacent crack tips (Fig. 3A).

https://doi.org/10.5194/egusphere-2026-4027
Preprint. Discussion started: 6 August 2026

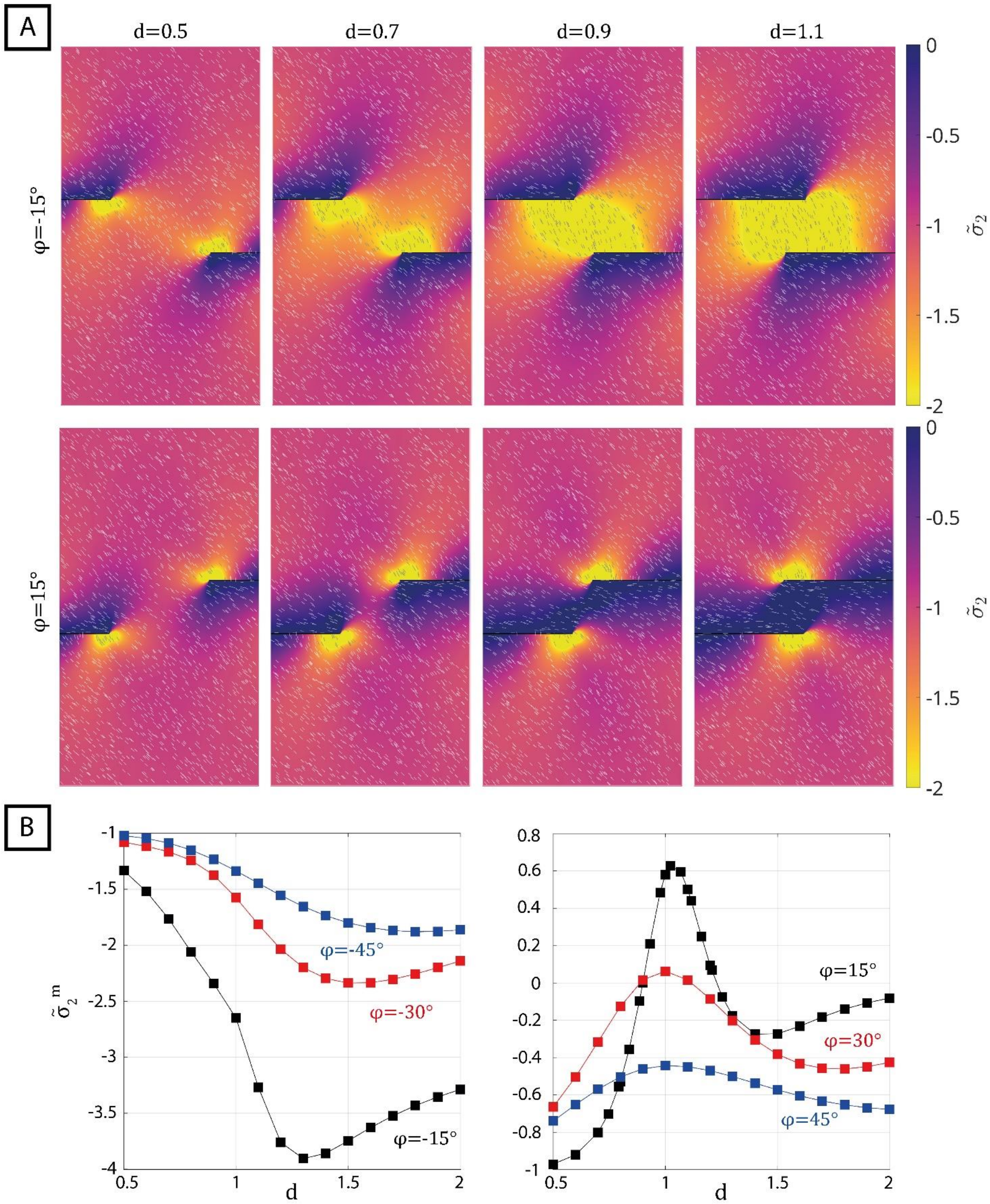

Fig. 3: (a) Magnitude of the minor in-plane principal stress $\tilde{\sigma}_2$ for different geometric configurations of *en echelon* crack arrays. Only the central unit cell is shown. Crack orientation: ϑ=0° (mode II cracks relative to far-field simple shear). In each row, the array orientation φ is fixed: -15° (top) and 15° (bottom). Along each

https://doi.org/10.5194/egusphere-2026-4027
Preprint. Discussion started: 6 August 2026

row, d varies from 0.5 to 1.1. White and black lines indicate the local trajectories of the major in-plane principal stress $\vec{\sigma}_1$. (b) Normalized and reduced minor in-plane principal stress magnitude $\tilde{\sigma}_2^m$ calculated at the midpoint between the neighboring crack tips in an array of *en echelon* cracks oriented at ϑ=0° as a function of the projected overlap d. Different colors represent different crack array orientations φ. The symmetrical configurations with φ =±15°, ±30°, and ±45° are illustrated in the right and left panel, respectively.

For the φ=-15° configuration, mechanical interaction between neighboring cracks is weak at d=0.5 (Fig. 3A). The shapes of the reduced compression lobes are similar to those of isolated cracks described in the previous section, and the deflection of $\vec{\sigma}_1$ is mostly limited to the immediate vicinity of the crack tips. At d=0.7, mechanical interaction between the neighboring cracks strengthens, and partial overlap of strongly depressed compressive stress regions ($\tilde{\sigma}_2 < -2$) is observed (Fig. 3A). In this configuration, the trajectories of $\vec{\sigma}_1$ slightly deflect between adjacent tips, particularly near the boundaries of the reduced compression regions, where they follow the contours of the $\tilde{\sigma}_2$ perturbation. The configuration with d=0.9 represents the most effective geometric arrangement for overlap of reduced compression (potentially effective tension) regions around individual crack tips, which merge into regular, elliptically shaped areas connecting adjacent tips (Fig. 3A). In this configuration, the trajectories of $\vec{\sigma}_1$ within the regions of reduced stress tend to align along the line linking neighboring crack tips. For d=1.1, interaction remains significant and strongly reduced compression regions are observed between adjacent tips. The local trajectories of $\vec{\sigma}_1$are approximately perpendicular to the cracks within the reduced compression regions and parallel to them in the elevated stress zones. For this configuration, the trajectories of $\vec{\sigma}_1$ no longer align with the line connecting the neighboring crack tips (Fig. 3A).

For φ=15°, interaction between reduced stress regions at adjacent crack tips is weak for d between 0.5 and 0.7 (Fig. 3A). Between the cracks, the local trajectories of $\vec{\sigma}_1$ are nearly perpendicular to the line connecting their neighboring tips, indicating conditions unfavorable for potential linkage development (Fig. 3A). As d

https://doi.org/10.5194/egusphere-2026-4027
Preprint. Discussion started: 6 August 2026

increases, elevated compression zone progressively builds and broadens between neighboring crack tips. Thus, for the array orientation of φ=15°, increasing crack clustering promotes elevated compression between their tips and creates unfavorable conditions for crack linkage (Fig. 3A).

Fig. 3B illustrates the dependence of $\tilde{\sigma}_2$ calculated at the midpoint between the tips of neighboring cracks ($\tilde{\sigma}_2^m$) on the projected overlap d for different values of φ. In the configurations with φ<0° (Fig. 3B, left panel), the obtained curves show that with increasing d $\tilde{\sigma}_2^m$ decreases super-linearly down to a minimum value and then gradually increases. The value of d that corresponds to the minimum $\tilde{\sigma}_2^m$ increases as array orientation departs from the horizontal shear direction (decreasing φ) (Fig. 3B). For φ=-30°, the minimal $\tilde{\sigma}_2^m$ value is attained for the projected overlap d equal to about 1.5. The arrays that align into the horizontal shear direction produce more pronounced minimum values of $\tilde{\sigma}_2^m$ (approximately -3.9).

For configurations with φ>0°, $\tilde{\sigma}_2^m$ increases as d increases, reaching a maximum at about d=1 for all the studied cases (Fig. 3B). The maximum values of $\tilde{\sigma}_2^m$ in the configurations with φ=15° and 30° are positive, indicating elevated compression at the midpoint between the tips of adjacent cracks (Fig. 3B). As d further increases, $\tilde{\sigma}_2^m$ decreases to a local minimum at a value of d that depends on the array orientation, and then increases again asymptotically to 0 (Fig. 3B). The local minimum of $\tilde{\sigma}_2^m$ stays above -1 in all configurations, indicating that the normalized and reduced minor in-plane principal stress magnitude in this region is higher than its background value.

Fig. 4 illustrates the distribution of the normalized effective cohesion $\tilde{C}$, the normalized first invariant of the strain tensor, $\bar{I}_1 = tr(\bar{\boldsymbol{\varepsilon}})$, and the normalized shear strain $\bar{\varepsilon}_{xy}$ around cracks oriented at ϑ=0° and arranged in arrays oriented at φ=-15°, for d values ranging from 0.8 to 1.1. The distribution of $\tilde{C}$ is asymmetrical around the crack tips. In the interior region between neighboring cracks, $\tilde{C}$ attains its highest values (over 60 MPa) within two lobe-shaped regions, while the lowest values are distributed in the exterior areas between the cracks. At d=0.8, the regions of high $\tilde{C}$ at the tips of individual cracks do not overlap, and $\tilde{C}$≈45 MPa at the midpoint between neighboring crack tips (Fig. 4). The lobe-shaped regions still do not overlap at d=0.9, but the interaction is stronger and $\tilde{C}$≈55 MPa at the midpoint (Fig. 4). At higher values of d, overlap between the

https://doi.org/10.5194/egusphere-2026-4027
Preprint. Discussion started: 6 August 2026

lobes of high $\tilde{C}$ is observed, and the entire region between the crack tips is characterized by values of $\tilde{C}$ that exceed 60 MPa (Fig. 4). In all configurations, one of the potential fracture directions is oriented at θ≈90°, indicating potential linkage between the tips of neighboring cracks in the neutral overlap configuration (d=1). The conjugate fracture orientation is θ≈-35°.

https://doi.org/10.5194/egusphere-2026-4027
Preprint. Discussion started: 6 August 2026

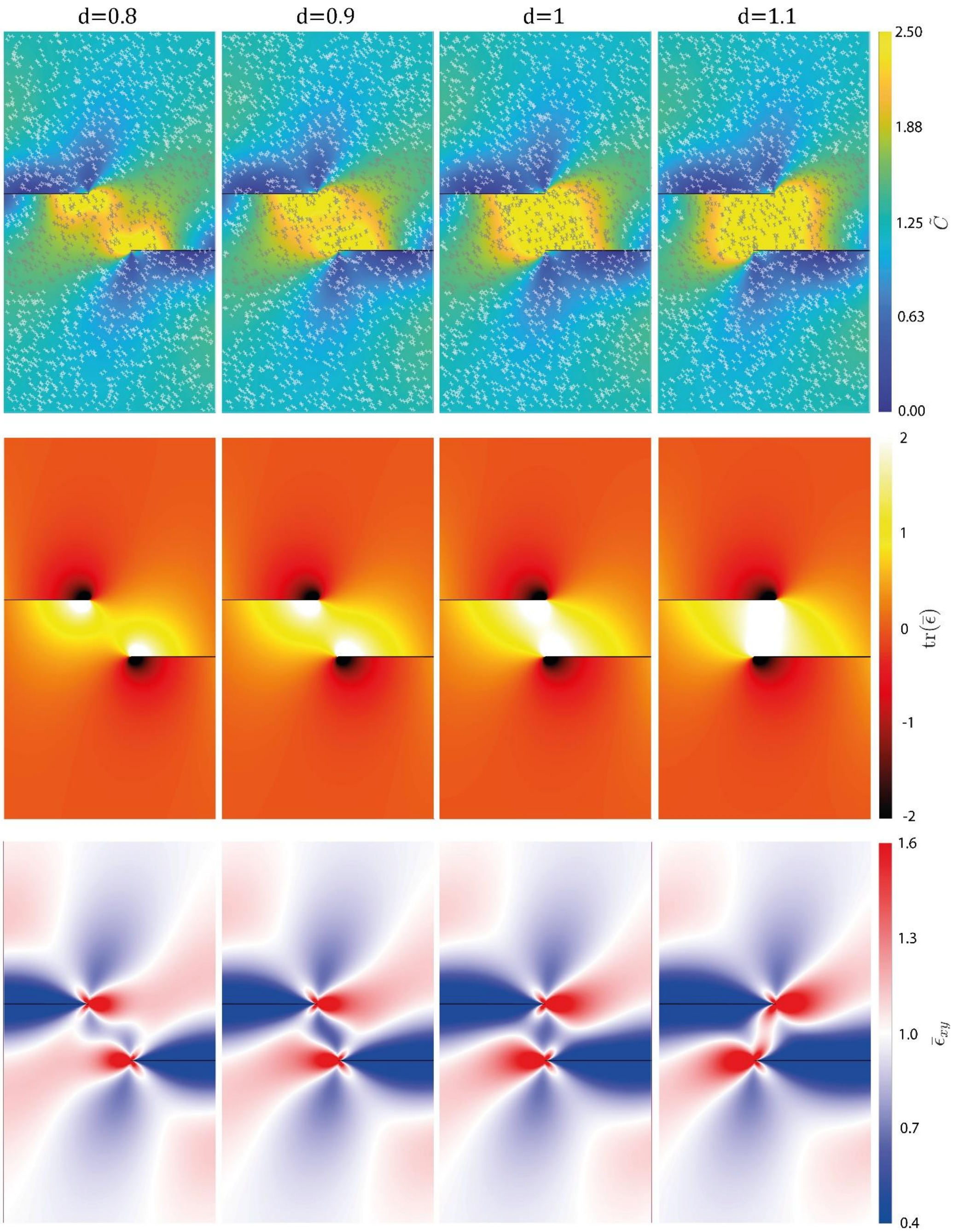

Fig. 4: Normalized effective cohesion $\tilde{C}$, normalized first strain invariant $\bar{I}_1$ and shear strain component $\bar{\varepsilon}_{xy}$ for different geometric configurations of *en echelon* crack arrays (from top to bottom row). The array

https://doi.org/10.5194/egusphere-2026-4027
Preprint. Discussion started: 6 August 2026

orientation is fixed at φ=-15°, and the crack orientation is set at ϑ=0°. The projected overlap d is varied in columns between 0.8 and 1.1. White and black lines in the first row indicate the potential orientations of conjugate shear fractures.

The first invariant $\bar{I}_1$, which represents the local volumetric strain, exhibits positive values corresponding to local dilation distributed within lobe-shaped regions between the tips of neighboring cracks, and negative values corresponding to local contraction distributed symmetrically with respect to the crack orientation. At d=0.8 the lobes of local dilation do not overlap (Fig. 4). A weak interaction is observed at d=0.9, and overlap between the lobes occurs at d=1.0 (Fig. 4). At d=1.1, the lobes completely overlap and merge into an elongated elliptical-rectangular region connecting the tips, where $\bar{I}_1$ reaches high positive values (Fig. 4).

The distribution of the shear strain component $\bar{\varepsilon}_{xy}$ is characterized by high values concentrated within lobes emanating from the crack tips and elongating in the crack direction, as well as two symmetrical, smaller lobes elongating obliquely relative to the crack and pointing towards the crack center. For underlapping cracks d=0.8, a weak interaction can be observed between the major lobes of high shear strain at the individual crack tips (Fig. 4). At increasing values of d between 0.9 and 1.0, regions of strain shadowing overlap, leading to the formation of a sigmoidal zone, where $\bar{\varepsilon}_{xy}$ is lower than its unit background value (Fig. 4). For overlapping cracks d=1.1, the smaller lobes of high $\bar{\varepsilon}_{xy}$ interact, and sigmoidal regions of high shear strain linking neighboring crack tips are observed (Fig. 4).

Fig. 5A presents the perturbation of $\tilde{\sigma}_2$ around cracks for configurations with the crack inclination fixed at ϑ=0° and the projected overlap between the cracks set to d=0.8, while the inclination of the crack array φ is varied. Fig. 5A shows configurations with φ ranging from -5° to -20° (top row) and the corresponding symmetrical configurations around $\vec{\sigma}_1^{\infty}$, with φ ranging from 5° to 20° (bottom row). The left-most panel displays the collinear crack configuration. Additional examples showing the effect of array orientation for vertical mode II cracks and collinear mode I-oriented cracks are reported in Fig. A2.

https://doi.org/10.5194/egusphere-2026-4027
Preprint. Discussion started: 6 August 2026

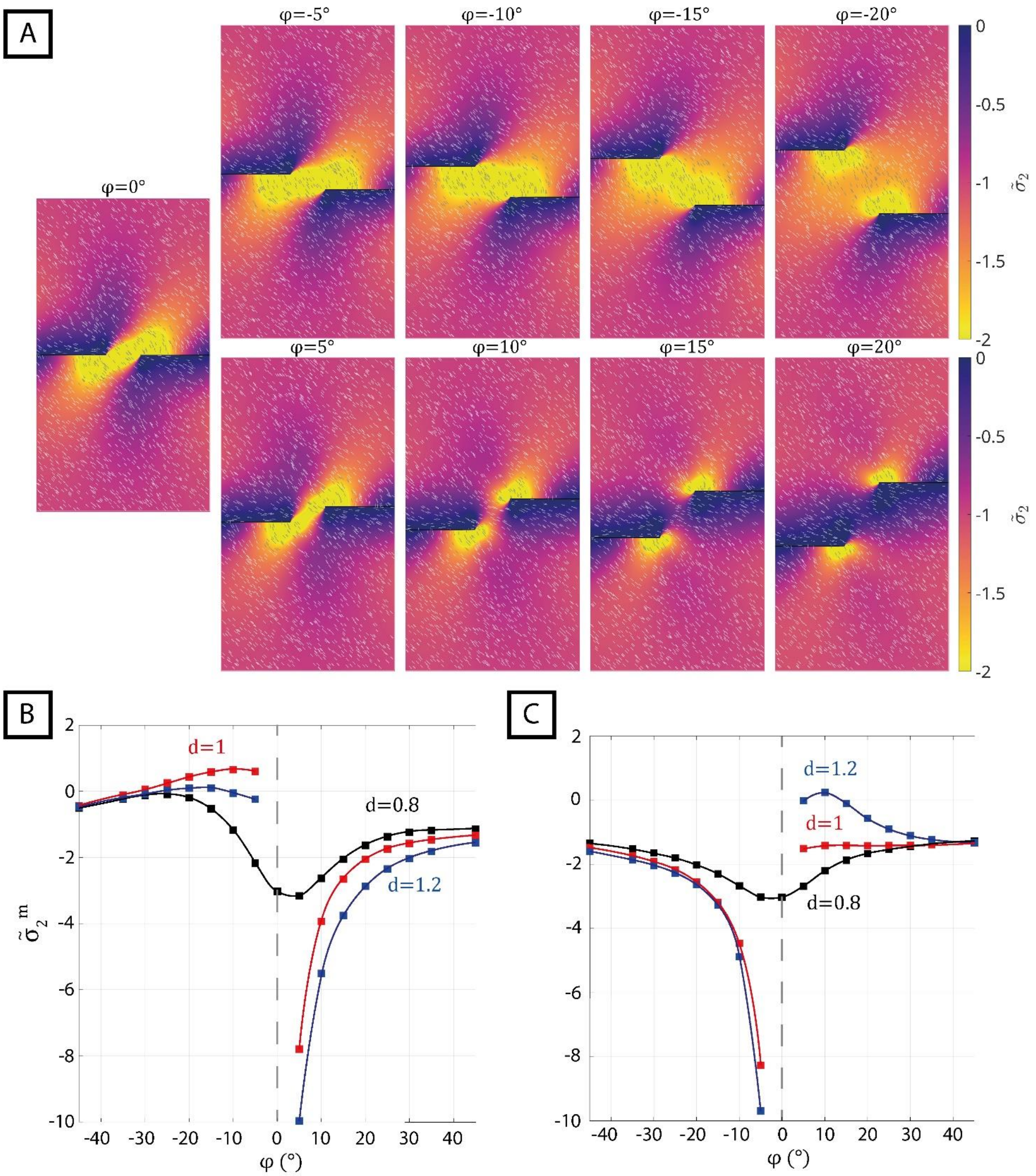

Fig. 5: (a) Normalized and reduced minor principal stress magnitude $\tilde{\sigma}_2$ for different geometric configurations of *en echelon* crack arrays. Only the central unit cell is shown. The crack orientation is fixed at ϑ=0°. The projected overlap is fixed at d=0.8. The crack array orientation φ is first set to 0° and then ranges from -5° to -20° (top row) and from 5° to 20° (bottom row). White and black lines indicate the local trajectories of the major in-plane principal stress $\vec{\sigma}_1$. B-C) Normalized and reduced minor in-plane principal stress magnitude $\tilde{\sigma}_2^m$ calculated at the midpoint between the two innermost cracks in an array of *en echelon* cracks. Different

https://doi.org/10.5194/egusphere-2026-4027
Preprint. Discussion started: 6 August 2026

colors represent different values of the projected overlap d: underlapping cracks (d=0.8), neutral cracks (d=1), and overlapping cracks (d=1.2). (b) The crack orientation is fixed at ϑ=0°, and the dependence of $\tilde{\sigma}_2^m$ on φ is illustrated. (c) The array orientation is fixed at φ=0°, and the dependence of $\tilde{\sigma}_2^m$ on ϑ is presented.

When the crack array is aligned with $\vec{\sigma}_1^\infty$, the distance between adjacent tips is increased and the interaction between regions of reduced compression near the crack tips is weakened. For φ=-5 to -10°, strong overlap of reduced compression regions is observed, but the local trajectories of $\vec{\sigma}_1$ are not favorable for the linkage between the adjacent tips (Fig. 5A). For φ =-15 to -20°, the reduced compression regions overlap and the local trajectories of $\vec{\sigma}_1$ tend to connect neighboring tips (Fig. 5A).

Reduced compression between adjacent crack tips is also observed for φ=5-10°, but in these configurations the local trajectories of $\vec{\sigma}_1$ are nearly perpendicular to the elongation of the discussed regions (Fig. 5A). The $\vec{\sigma}_1$ trajectories prominently deflect between the tips and tend to align with the crack orientation. As φ increases from 15° to 20°, regions of elevated compression develop between neighboring crack tips, with the local trajectories of $\vec{\sigma}_1$ aligning with the direction of $\vec{\sigma}_1^\infty$ (Fig. 5A).

For the φ=0° case, the lobe-shaped regions of reduced compression partially overlap within a zone elongating at approximately 30°, where the $\vec{\sigma}_1$ trajectories are roughly aligned with the direction of $\vec{\sigma}_1^\infty$ (Fig. 5A). The deflection of $\vec{\sigma}_1$ is more pronounced near the tips of the individual crack tips. The $\vec{\sigma}_1$ trajectories are approximately perpendicular to the cracks in the regions of reduced compression and parallel to them within regions of elevated compression.

Fig. 5B and C illustrate the dependence of $\tilde{\sigma}_2$ calculated at the midpoint between the tips of neighboring cracks, denoted by $\tilde{\sigma}_2^m$, for different values of d on the array orientation φ (Fig. 5B, with ϑ=0°), and on the crack orientation ϑ (Fig. 5C, with φ=0°). In the configurations with ϑ=0° (Fig. 5B), $\tilde{\sigma}_2^m$ increases gradually as φ increases from -45° to about -25° to -10° (depending on the projected overlap), reaching a maximum which, in the configurations with high overlap, is positive and therefore indicates local elevated compression. Beyond the maximum, $\tilde{\sigma}_2^m$ decreases as the array direction approaches the horizontal (Fig. 5B). For

https://doi.org/10.5194/egusphere-2026-4027
Preprint. Discussion started: 6 August 2026

underlapping cracks (d=0.8), the minimum $\tilde{\sigma}_2^m$ is reached at $\varphi \approx 5°$ (Fig. 5B). In the neutral and overlapping configurations (d=1.0 and d=1.2, respectively), $\tilde{\sigma}_2^m$ diverges to negative values as the cracks are brought towards contact, at low positive values of φ (Fig. 5B). For all the curves corresponding to different d values, $\tilde{\sigma}_2^m$ increases as φ increases, approaching its background value as φ approaches 45° (Fig. 5B).

In the configurations with φ=0° and variable ϑ, $\tilde{\sigma}_2^m$ decreases steeply as ϑ increases from -45° and approaches 0° (Fig. 5C). For low negative values of ϑ $\tilde{\sigma}_2^m$ diverges to $-\infty$, especially in the configurations with neutral and high overlap. As ϑ increases from 0° to higher positive values, $\tilde{\sigma}_2^m$ reaches a maximum in the configurations with d=1.0 and d=1.2 (in the latter case, the maximum is positive, indicating elevated compression) (Fig. 5C). For all configurations with different values of d, $\tilde{\sigma}_2^m$ approaches its background value as ϑ approaches 45° (Fig. 5C).

Fig. 6 illustrates the distribution of $\tilde{C}$, $\bar{I}_1$ and $\bar{\varepsilon}_{xy}$ around underlapping cracks (d=0.8) oriented at ϑ=0° and arranged in arrays oriented at φ angles ranging from 0° to -15°. Additional examples are illustrated in Figures A3, A4. For φ ranging from 0° to -10°, the lobe-shaped regions where $\tilde{C}$ exceeds 60 MPa at the tips of neighboring cracks overlap, merging into elliptical regions of high $\tilde{C}$ elongating along the line connecting the crack tips (Fig. 6). In these regions, the potential conjugate fracture orientations are θ≈-15° and -70° (Fig. 6). This indicate that potential crack linkage would be facilitated at low negative values of φ, where the line connecting the tips of neighboring cracks is approximately oriented at -15°. At φ=-15°, the regions of high $\tilde{C}$ do not overlap, although strong interaction is still observed (Fig. 6).

https://doi.org/10.5194/egusphere-2026-4027
Preprint. Discussion started: 6 August 2026

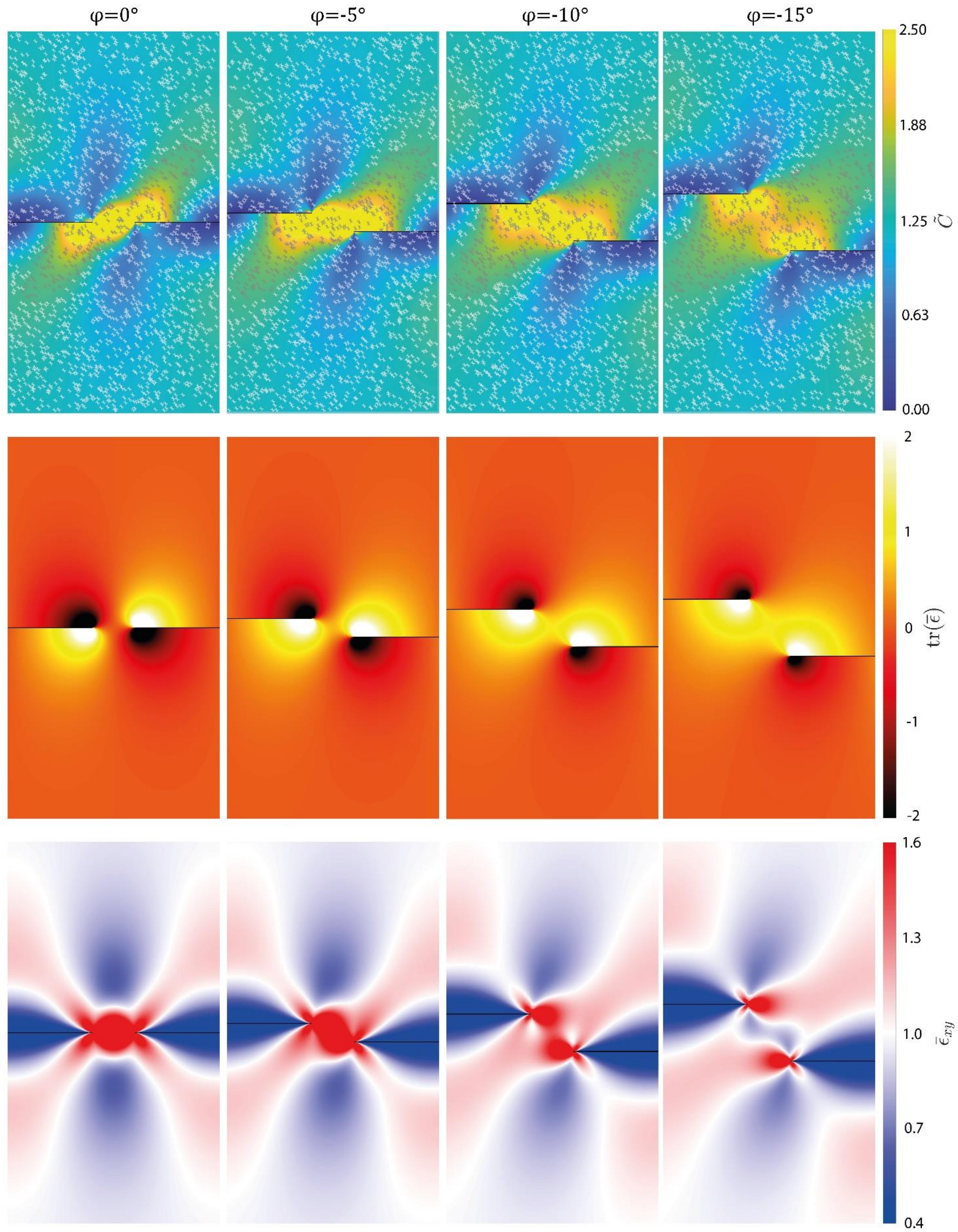

637

638 Fig. 6: Normalized effective cohesion $\tilde{C}$, normalized first strain invariant $\bar{I}_1$ and shear strain component $\bar{\varepsilon}_{xy}$

639 for different geometric configurations of *en echelon* crack arrays. The crack orientation is set at ϑ=0°, and the

https://doi.org/10.5194/egusphere-2026-4027
Preprint. Discussion started: 6 August 2026

projected overlap is fixed at d=0.8. The array orientation is varied between φ=0°, -5°, -10°, and -15°. White and black lines in the first row indicate the potential orientations of conjugate shear fractures.

In all four configurations, the lobe-shaped regions characterized by high volumetric dilation are confined to the tips of the individual cracks and show no evident overlap, although weak interaction is observed at φ=-10° and -15° (Fig. 6).

At φ=0°, the lobes characterized by high shear strain merge into an elliptical region (Fig. 6). This region of high $\bar{\varepsilon}_{xy}$ elongates between the tips of neighboring cracks at φ=-5°; in this configuration, it exhibits a sigmoidal shape (Fig. 6). At φ=-10°, the major lobes of concentrated $\bar{\varepsilon}_{xy}$ show no overlap, although interaction is still observed. At φ=-15° shear strain is low between the crack tips, and a clear overlap between areas of strain shadowing can be observed (Fig. 6).

Fig. 7A illustrates the dependence of $\tilde{\sigma}_2$ perturbation on the crack orientation ϑ in *en echelon* arrays with φ=0° and d=0.9. The values of ϑ range from -10° to -45° (top row) and, symmetrically with respect to the shearing direction, from 10° to 45° (bottom row). Further configurations illustrating the effect of crack orientation for selected array orientations are shown in Fig. A5.

https://doi.org/10.5194/egusphere-2026-4027
Preprint. Discussion started: 6 August 2026

656

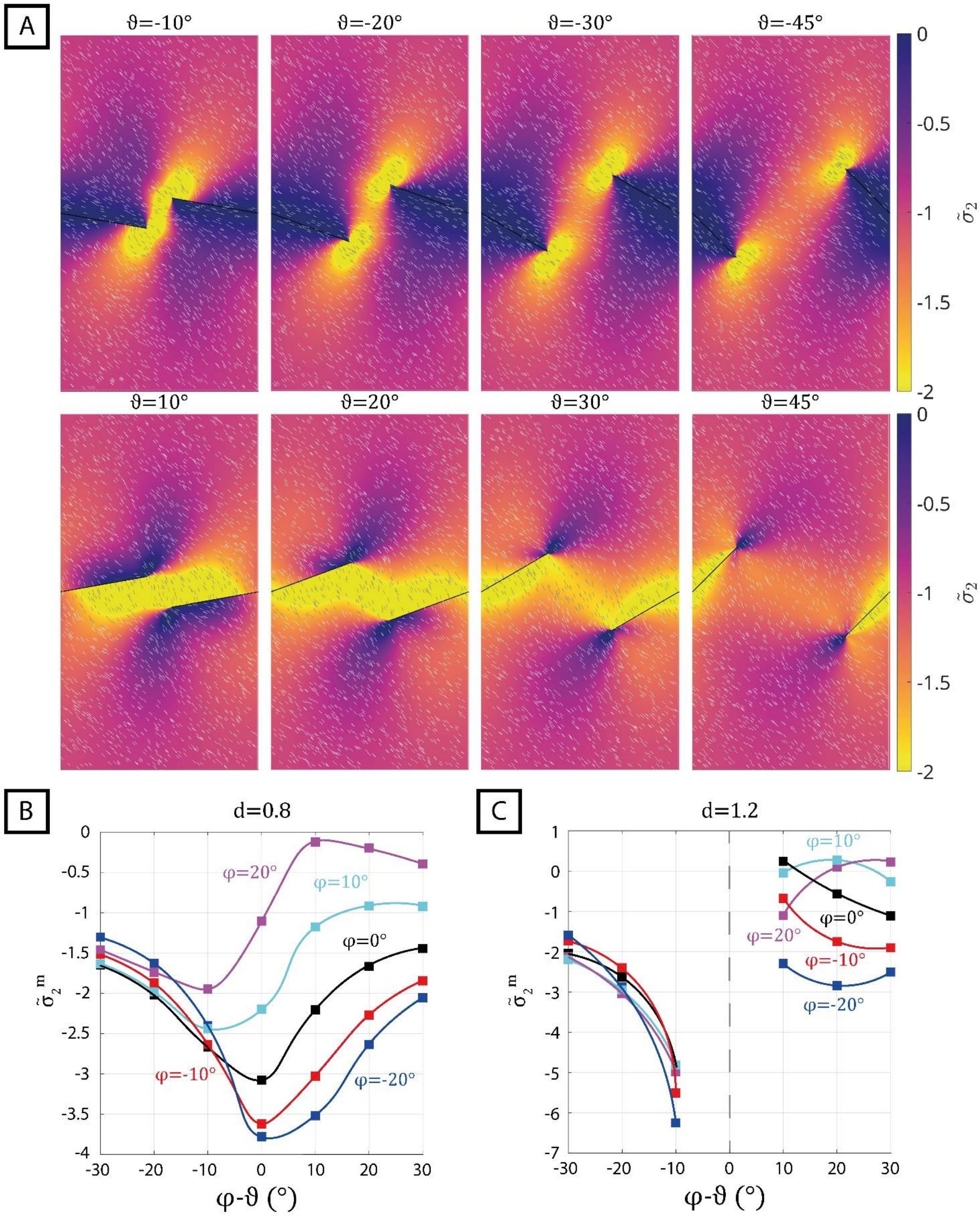

657

658 Fig. 7: (a) Magnitude of the minor in-plane principal stress $\tilde{\sigma}_2$ for different geometric configurations of *en*
659 *echelon* crack arrays. The crack array orientation is fixed at φ=0° and the projected overlap at d=0.9. The
660 crack orientation ϑ ranges from -10° to -45° along the top row and from 10° to 45° along the bottom row.
661 White and black lines represent the local trajectories of the major in-plane principal stress $\vec{\sigma}_1$. B-C)

Experimental curves describing the dependence of the normalized effective minor in-plane principal stress $\tilde{\sigma}_2$ calculated at the midpoint between the two innermost cracks ($\tilde{\sigma}_2^m$) in arrays of *en echelon* cracks on the difference between the array orientation φ and the crack orientation ϑ. Different colors represent different array orientations: φ=0°, 10°, 20°, -20°, and -10°. (b) The results for underlapping cracks (d=0.8), are illustrated. (c) The results for overlapping cracks (d=1.2) are presented.

For ϑ ranging from -10° to -20°, the regions of depressed compression between adjacent crack tips overlap, forming elongated areas oriented approximately between 35° and 45° (Fig. 7A). Although these crack orientations promote overlap of reduced compression regions, the trajectories of major principal stress $\vec{\sigma}_1$ tend to align with the cracks rather than in orientations favorable for linkage development between the neighboring tips (Fig. 7A). At ϑ=-30° and -45°, the reduced compression lobes cease to overlap, but oblique zones of weaker interaction persist, within which the local trajectories of $\vec{\sigma}_1$ are oriented at -45° (Fig. 7A).

In the counterpart symmetrical configurations, for ϑ=10° the reduced compression lobes overlap, but the local trajectories of $\vec{\sigma}_1$ show no alignment with the line connecting adjacent crack tips (Fig. 7A). For ϑ values between 20° and 30°, both the overlap of reduced compression regions and the orientation of $\vec{\sigma}_1$ suggest that these geometries are potentially favorable for crack linkage via tensile mechanism (Fig. 7A). For ϑ values over 30°, the separation between adjacent crack tips becomes too large for reduced compression lobes to overlap, although weak interactions can still be observed (Fig. 7A).

Fig. 8 illustrates the distribution of $\tilde{C}$, $\bar{I}_1$ and $\bar{\varepsilon}_{xy}$ around underlapping cracks (d=0.9) arranged in arrays oriented at φ=0°, with ϑ ranging between 0° and -30°. At ϑ=0° and -10°, overlap between regions of high $\tilde{C}$ is observed, within elliptical areas elongating between the crack tips, although in both configurations the local orientations of the potential conjugate fractures do not effectively connect the neighboring tips (Fig. 8). At ϑ=-20°, interaction is weaker, and $\tilde{C}$≈50 MPa at the midpoint between the tips (Fig. 8). At ϑ=-30°, the interaction is further weakened, with $\tilde{C}$≈40 MPa at the midpoint (Fig. 8).

https://doi.org/10.5194/egusphere-2026-4027
Preprint. Discussion started: 6 August 2026

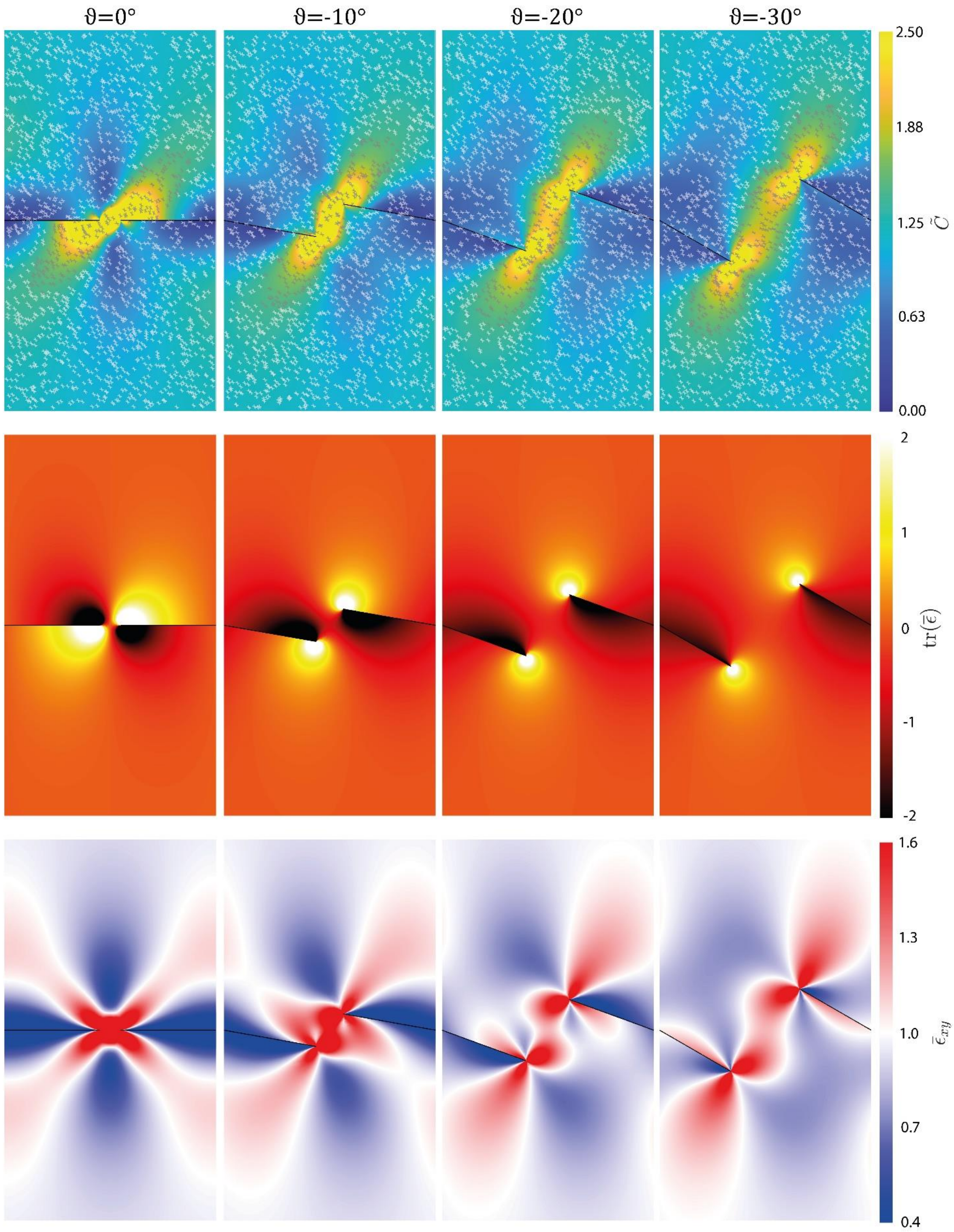

687

688 Fig. 8: Normalized effective cohesion $\tilde{C}$, normalized first strain invariant $\bar{I}_1$ and shear strain component $\bar{\varepsilon}_{xy}$
689 for different geometric configurations of *en echelon* crack arrays. The array orientation is set at φ=0°, and

https://doi.org/10.5194/egusphere-2026-4027
Preprint. Discussion started: 6 August 2026

the projected overlap is fixed at d=0.9. The crack orientation is varied between ϑ=0°, -10°, -20°, and -30°. White and black lines in the first row indicate the potential orientations of conjugate shear fractures.

No clear overlap between regions of localized dilation or contraction are observed, except for the configuration with ϑ=-10°, where weak overlap between compaction regions occurs (Fig. 8). At ϑ=-30°, approaching the configuration in which the cracks are aligned with the far-field orientation of the major principal stress, the lobes of high dilation tend to elongate from the tips in the crack direction, while contraction localizes along the major dimension of the cracks (Fig. 8).

At ϑ=0°, the lobes characterized by high $\bar{\varepsilon}_{xy}$ component of shear strain merge into an elliptical region (Fig. 8). At ϑ=-10°, the overlap is partial, and high $\bar{\varepsilon}_{xy}$ values concentrate within a figure-eight-shaped region (Fig. 8). For configurations with ϑ=-20° and -30°, the interaction weakens and relatively high shear strain localizes within a sigmoidal region connecting neighboring crack tips (Fig. 8).

Fig. 9 illustrates the dependence of the perturbation of $\tilde{\sigma}_2$ on the alignment between the crack orientation ϑ and the array orientation φ for overlapping crack configurations (d=1.2). Three array orientations are considered: φ=0°, 20°, and -20° (the latter two configurations are symmetrical with respect to the horizontal). For each array orientation, ϑ is varied accordingly, resulting in four configurations with φ- ϑ=30°, 10°, -10° and -30°.

https://doi.org/10.5194/egusphere-2026-4027
Preprint. Discussion started: 6 August 2026

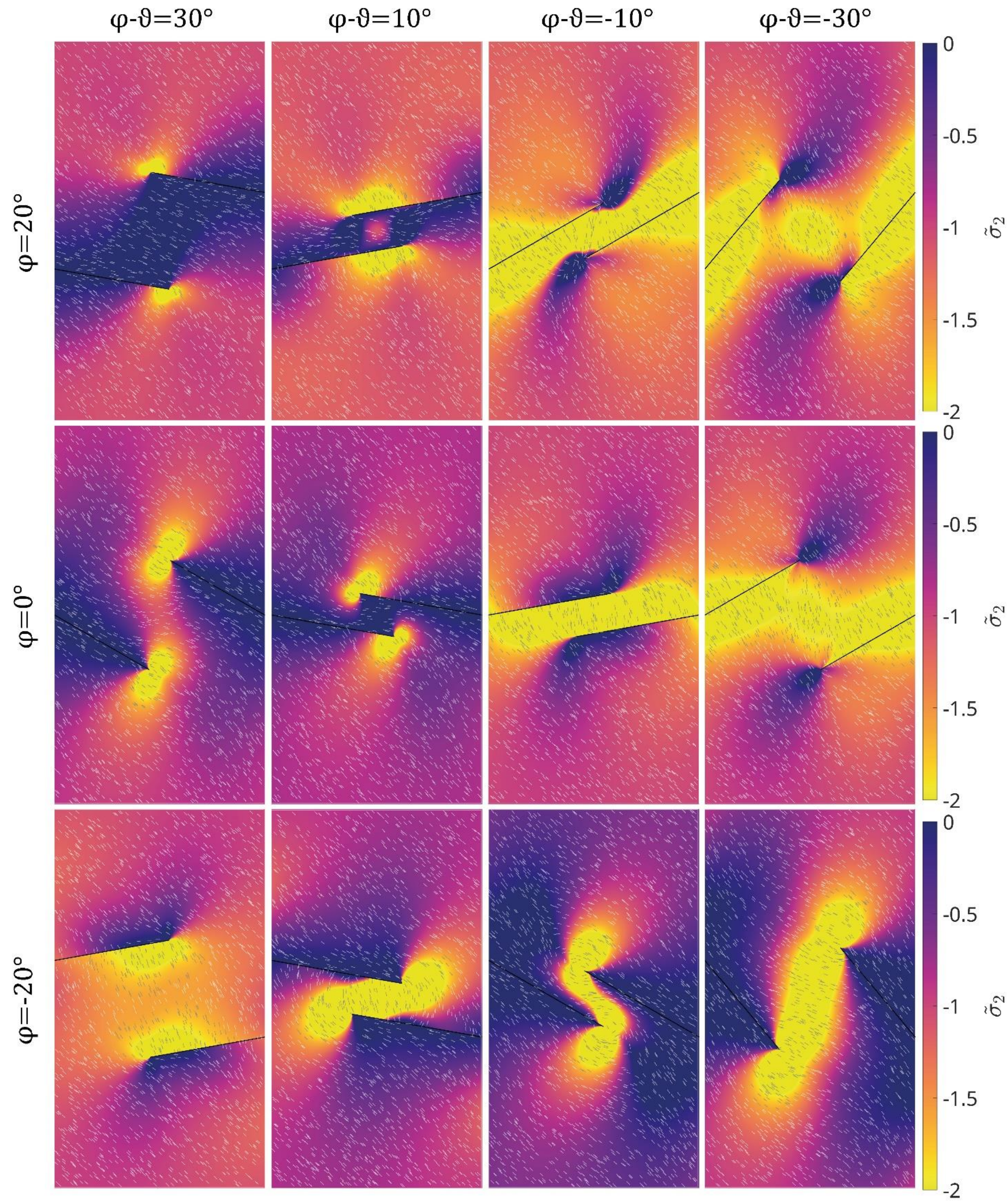

Fig. 9: Magnitude of the minor in-plane principal stress $\tilde{\sigma}_2$ for different geometric configurations of *en echelon* crack arrays. The crack array orientation varies between φ=20° (top row), φ=0° (middle row), and φ=-20° (bottom row). The projected overlap is fixed at d=1.2. The difference between φ and the crack orientation ϑ varies between 30°, 10°, -10°, -30°. White and black lines represent the local trajectories of the major in-plane principal stress $\vec{\sigma}_1$.

https://doi.org/10.5194/egusphere-2026-4027
Preprint. Discussion started: 6 August 2026

In the configuration with φ=20°, regions characterized by reduced compression are confined near the tips of the individual cracks for φ- ϑ=30° and 10°, while elevated compression occurs in the interior region between the cracks (Fig. 9). Within the high compression regions, the trajectories of major in-plane principal stress $\vec{\sigma}_1$ deflect and tend to align with the cracks. In the configuration with φ-ϑ=10°, a small circular region in which $\tilde{\sigma}_2$ is approximately equal to its background value is observed, because the lobes of elevated compression at the tips of neighboring cracks do not overlap effectively (Fig. 9). At φ-ϑ=-10°, the entire inner region between the overlapping cracks is characterized by strongly reduced compression (Fig. 9). Low values of $\tilde{\sigma}_2$ are also observed along the major dimension of the cracks. In this configuration, the local trajectories of $\vec{\sigma}_1$ connect the tips of neighboring cracks. At φ-ϑ=-30°, a similar stress distribution occurs, although the interacting lobes of elevated compression at the tips of the individual cracks break the continuity of the reduced compression region, which effectively localizes near the crack tips and within a circular region between them (Fig. 9). The local trajectories of $\vec{\sigma}_1$ align with the line connecting the tips of adjacent cracks.

In the configuration with φ=0° and φ-ϑ=30°, the lobes of reduced compression show no overlap, although weak interaction occurs (Fig. 9). At φ-ϑ=10°, elevated compression occurs in the inner region between the cracks. In both these configurations, the local trajectories of $\vec{\sigma}_1$ tend to align with the crack array. At φ-ϑ=-10° and -30°, the inner region between the cracks is characterized by reduced compression (Fig. 9). In the first configuration, the region of high $\tilde{\sigma}_2$ is rectangular, and the local trajectories of $\vec{\sigma}_1$ are approximately perpendicular to the crack orientations within it. In the latter configuration, the region of low $\tilde{\sigma}_2$ is less continuous and exhibits a sigmoidal shape (Fig. 9). In this case, the trajectories of $\vec{\sigma}_1$ connect the tips of neighboring cracks.

For φ=-20° and φ-ϑ=30°, the inner region between the tips of neighboring cracks is characterized by relatively low $\tilde{\sigma}_2$, although the lobes where it reaches its lowest values do not overlap (Fig. 9). The crack tips are not connected by the local trajectories of $\vec{\sigma}_1$, which tend to orient perpendicular to the cracks. At φ-ϑ=10°, the lobes of strongly reduced compression overlap, merging into an elliptical region that connects the tips of

https://doi.org/10.5194/egusphere-2026-4027
Preprint. Discussion started: 6 August 2026

neighboring cracks (Fig. 9). However, these tips are not effectively connected by the local trajectories of $\vec{\sigma}_1$. At φ-ϑ=-10° and -30° regions of reduced compression occur between the crack tips, in elliptical regions elongating approximately along the line connecting the tips (Fig. 9). In these configurations, the local trajectories of $\vec{\sigma}_1$ tend to align with the crack array.

Fig. 7B-C illustrate the dependence of $\tilde{\sigma}_2^m$ ($\tilde{\sigma}_2$ calculated at the midpoint between the tips of neighboring cracks) for different values of d and φ on the alignment between the array orientation and the crack orientation, that is, on the difference $\varphi - \vartheta$. In both the underlapping d=0.8 (Fig. 7B) and overlapping d=1.2 (Fig. 7C) configurations, $\tilde{\sigma}_2^m$ decreases steeply as $\varphi - \vartheta$ increases from -30° to 0°. For d=0.8, $\tilde{\sigma}_2^m$ reaches a minimum at a value of $\varphi - \vartheta$ that depends on φ, and then increases as $\varphi - \vartheta$ approaches 30° for all configurations with different φ (Fig. 7B). The configuration with φ=-20° yields the lowest values of $\tilde{\sigma}_2^m$. For d=1.2, at low positive values of $\varphi - \vartheta$, $\tilde{\sigma}_2^m$ gradually decreases as $\varphi - \vartheta$ increases in the configurations with φ=0°, -10° and -20°, and increases to positive $\tilde{\sigma}_2^m$ values, corresponding to elevated compression, in the configurations with φ=10° and 20° (Fig. 7C).

Fig. 10 illustrates the distribution of $\tilde{C}$, $\bar{I}_1$ and $\bar{\varepsilon}_{xy}$ around underlapping cracks (d=0.9) arranged in arrays oriented at φ=-30°, -10°, 10° and 30°, with $\varphi - \vartheta$ fixed at -10°. At φ=-30°, an elliptical region where $\tilde{C}$ exceeds 60 MPa elongates approximately perpendicular to the crack direction (Fig. 10). Within this region, one of the potential conjugate fracture orientations, θ≈-75°, is approximately aligned with the line connecting the neighboring crack tips. At φ=-10° the region of overlap between the lobes of high $\tilde{C}$ exhibits an elliptical shape and elongates between the crack tips (Fig. 10). In this configuration as well, one of the orientations, θ≈-50°, effectively connects the crack tips. At φ=10° and 30°, the lobes of high $\tilde{C}$ overlap and merge into sigmoidal-shaped regions, within which one of orientations θ≈-40° and -25°, respectively, are consistent with potential linkage between the cracks (Fig. 10).

https://doi.org/10.5194/egusphere-2026-4027
Preprint. Discussion started: 6 August 2026

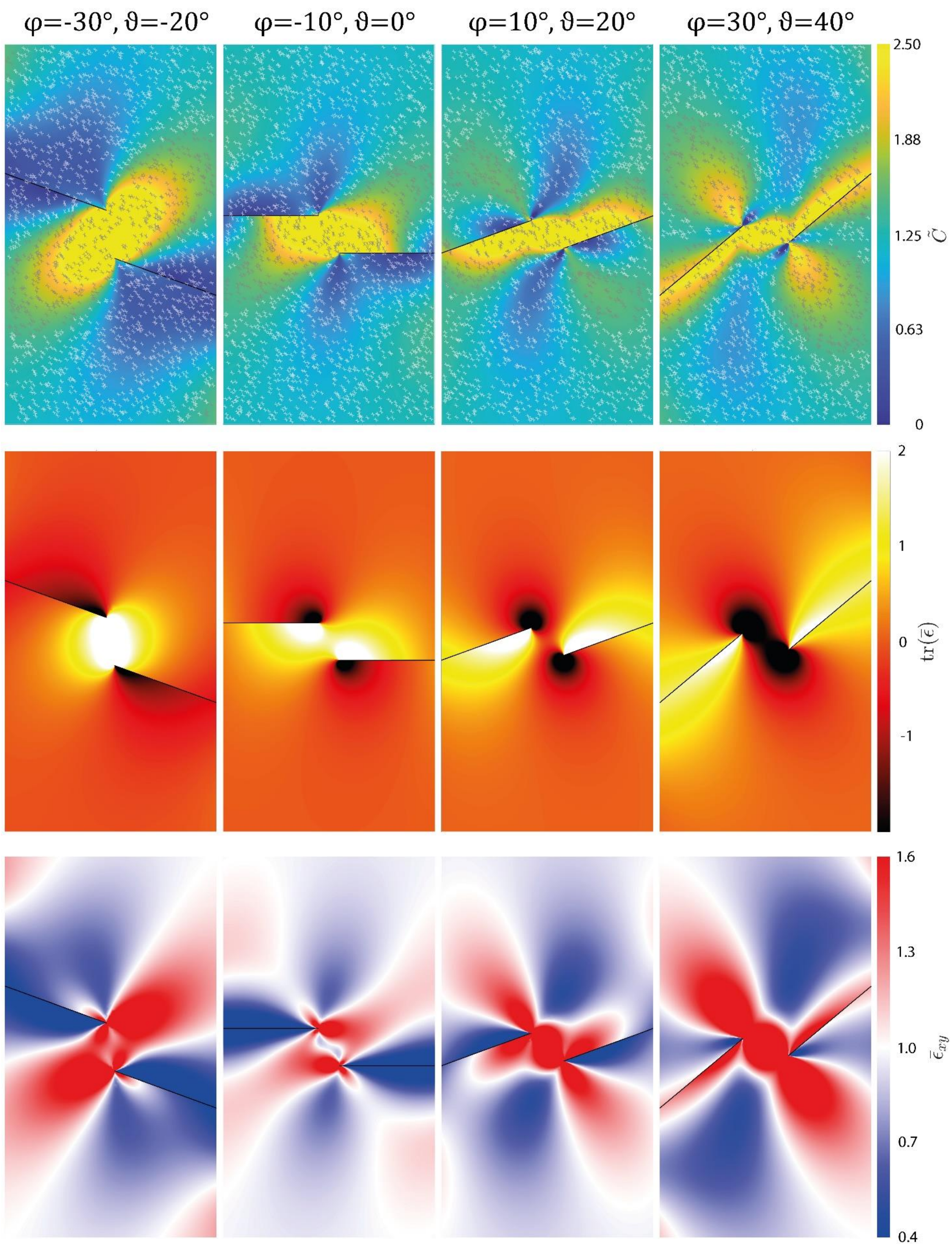

Fig. 10: Normalized effective cohesion $\tilde{C}$, normalized first strain invariant $\bar{I}_1$ and shear strain component $\bar{\varepsilon}_{xy}$ for different geometric configurations of *en echelon* crack arrays. The relative orientation between the array

https://doi.org/10.5194/egusphere-2026-4027
Preprint. Discussion started: 6 August 2026

and the cracks is set at $\varphi - \vartheta$=-10°, and the projected overlap is fixed at d=0.9. The array orientation is varied between φ=-30°, -10°, 10°, and 30°. White and black lines in the first row indicate the potential orientations of conjugate shear fractures.

An elliptical region of overlap between regions of localized dilation is observed at φ=-30°, while weaker interaction is observed at φ=-10° (Fig. 10). At φ=10°, weak contraction occurs in the region between the crack tips. A region of stronger contraction between the tips is observed at φ=30°. In the two latter configurations, dilation is confined near the tips of individual cracks, in the exterior region between them (Fig. 10).

At φ=-10° and -30°, the lobes of high $\bar{\varepsilon}_{xy}$ do not fully overlap, although large areas of $\bar{\varepsilon}_{xy}$ are observed in the exterior region between them (Fig. 10). Conversely, at φ=10° and 30°, a region of high $\bar{\varepsilon}_{xy}$ connects the tips of neighboring cracks. In these configurations, other lobe-shaped areas of high $\bar{\varepsilon}_{xy}$ occur, elongating in the direction of $\vec{\sigma}_1^{\infty}$ (Fig. 10).

Fig. 11 summarizes the results for the numerical experiments with *en echelon* crack arrays. The first general observation is that all the analyzed stress and strain quantities reach the highest values at the midpoints between neighboring crack tips in configurations with $d \geq 1$ (Fig. 11). Secondly, for overlapping cracks ($d > 1$), we observe similar magnitudes of $\tilde{\sigma}_2^m$, $\tilde{C}^m$, $\bar{I}_1^m$, and $\bar{\varepsilon}_{xy}^m$ compared to the neutral overlap configuration ($d = 1$), but the dependence of these quantities on φ and ϑ changes. As an example, $\bar{I}_1^m$ reaches its maximum value for $\varphi \approx \vartheta \approx -45°$ when $d = 1$, while it reaches the same values for $\varphi \approx \vartheta \approx 0°$ for $d = 1.2$ (Fig. 11C). The third general result from this set of experiments is that both the highest and lowest values of all the quantities we considered are reached when the cracks are aligned with the array orientation ($\varphi - \vartheta \approx 0°, \pm 180°$; Fig. 11).

https://doi.org/10.5194/egusphere-2026-4027
Preprint. Discussion started: 6 August 2026

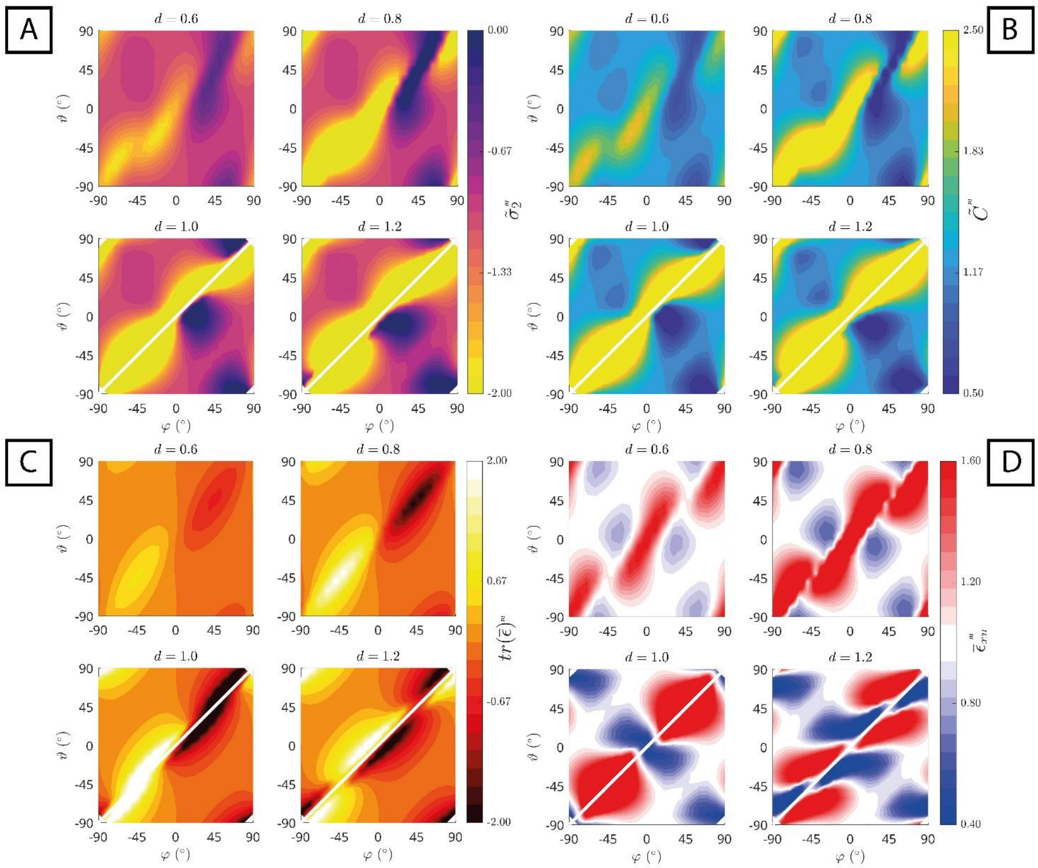

Fig. 11: Normalized magnitudes measured at the midpoint between the tips of neighboring cracks in the *en echelon* array of (a) the reduced minor in-plane principal stress $\tilde{\sigma}_2^m$, (b) the effective cohesion $\tilde{C}^m$, (c) the first invariant of the strain tensor $\bar{I}_1^m$, and (d) the shear strain component $\bar{\varepsilon}_{xy}^m$, for different values of φ, ϑ, and d.

4.3 Randomly distributed cracks

In this set of numerical experiments, we analyzed the spatial distribution around 500 cracks with random locations of the following quantities, each one normalized by its far-field value: the reduced minor in-plane stress magnitude $\tilde{\sigma}_2$, the effective cohesion $\tilde{C}$, the first strain tensor invariant $\bar{I}_1$, and the shear strain

https://doi.org/10.5194/egusphere-2026-4027
Preprint. Discussion started: 6 August 2026

component $\bar{\varepsilon}_{xy}$. We also analyzed the local trajectories of the major in-plane principal stress $\vec{\sigma}_1$ and the local orientations of the potential conjugate shear fractures inclined at $\theta = \pm\left(\frac{\pi}{4} - \frac{\phi}{2}\right) = \pm 27.5°$ relative to $\vec{\sigma}_1$. Among the 13 configurations that we simulated, we selected two for detailed analysis: (i) the configuration in which all cracks are horizontally aligned ($\vartheta_0 = 0°$ and $RanDeg = 0$), and (ii) the configuration in which all crack orientations are random ($RanDeg = 1$). For each model, we assess the mechanical interaction between cracks at three different scales: (i) the domain scale, (ii) an intermediate scale at which mechanical interactions between multiple cracks can be resolved and subsets of *en echelon* cracks can be analyzed, and (iii) the crack-length scale, at which interactions between a few cracks and the resulting perturbations of the stress and strain fields between adjacent crack tips can be investigated.

Fig. 12 illustrates the distributions of $\tilde{\sigma}_2$, $\tilde{C}$, $\bar{I}_1$, and $\bar{\varepsilon}_{xy}$ in the system with $\vartheta_0 = 0°$ and $RanDeg = 0$. Additional configurations with vertically and obliquely aligned cracks are shown in Figures A6 and A7. Inspection of the $\tilde{\sigma}_2$ distribution across the entire domain reveals regions of elevated compression elongating at angles of 40-45° (Fig. 12A). Smaller regions of reduced compression at the tips of individual crack tips overlap, elongating at angles between -10° and -18° (Fig. 12A). This type of mechanical interaction, caused by the overlap between the reduced-compression lobes at the crack tips that elongate at low angles relative to the crack direction, produces arrays of mechanically linked cracks oriented at approximately -15° (Fig. 12A). Due to the overlap between the reduced-compression lobes at the tips of individual cracks elongating at high angles relative to the crack direction, additional regions of potentially tensile stress develop at angles of 45-60°, connecting cracks in arrays oriented between -55° and -75° (Fig. 12A). However, we observe that only in arrays of cracks oriented at approximately -15° the local trajectories of $\vec{\sigma}_1$ effectively connect the tips of adjacent cracks, suggesting that extension fractures may promote crack coalescence in these regions (Fig. 12A, insets). In contrast, between cracks in arrays oriented at approximately -70°, the trajectories of $\vec{\sigma}_1$ tend to align with the direction of $\vec{\sigma}_1^{\infty}$, and fail to connect the tips of neighboring cracks (Fig. 12A, first inset).

https://doi.org/10.5194/egusphere-2026-4027
Preprint. Discussion started: 6 August 2026

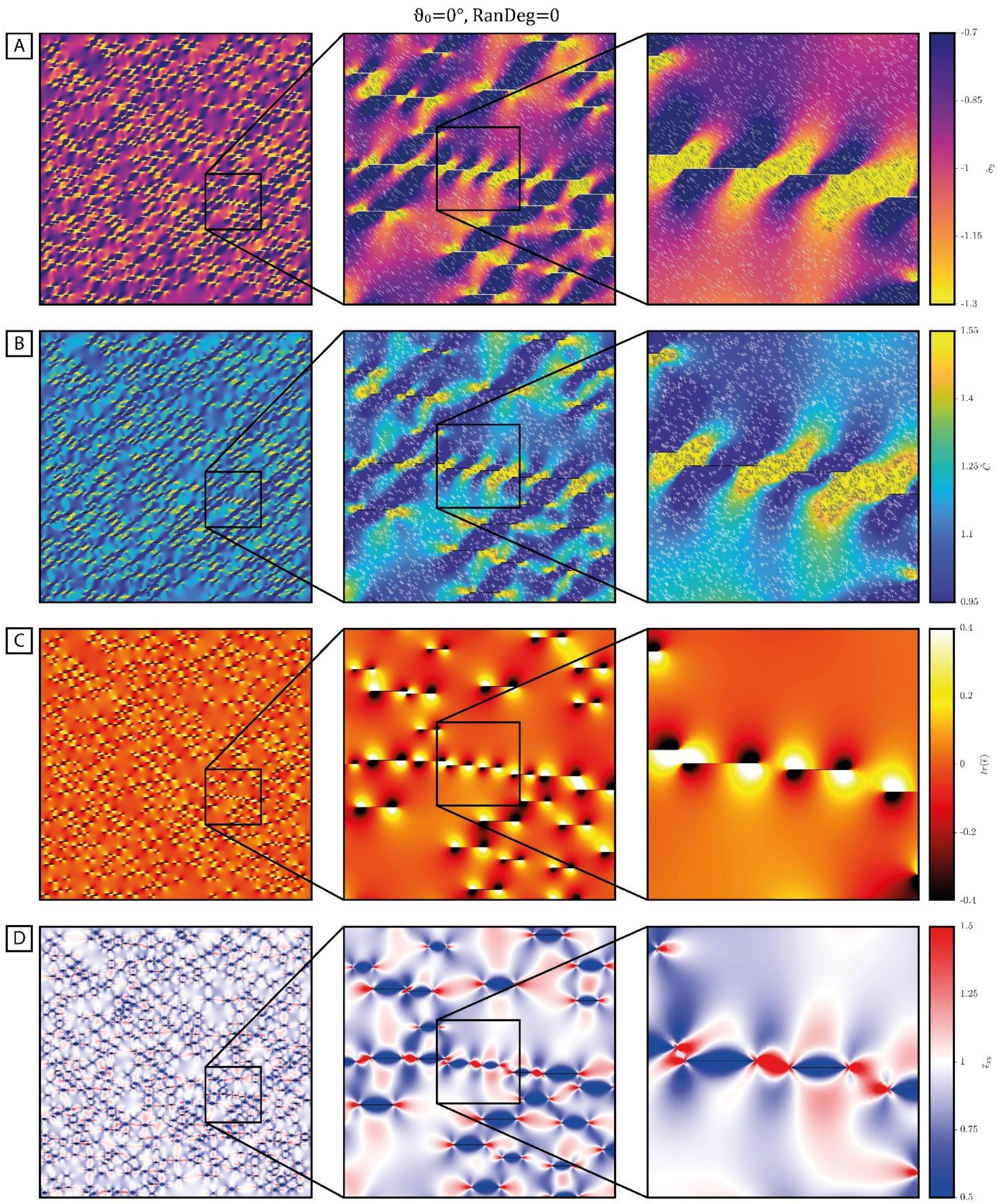

Fig. 12: Stress and strain fields in a system with 500 horizontally aligned cracks ($\vartheta_0 = 0°$ and $RanDeg = 0$) with random locations. In the first inset, a subdomain containing an *en echelon* array of cracks is illustrated. The second inset shows the interactions between the tips of a few cracks in the *en echelon* array. (a) Magnitude of the minor in-plane principal stress $\tilde{\sigma}_2$. White and black lines represent the local trajectories of

https://doi.org/10.5194/egusphere-2026-4027
Preprint. Discussion started: 6 August 2026

the major in-plane principal stress $\vec{\sigma}_1$. (b) Normalized effective cohesion $\tilde{C}$. White and black lines indicate the potential orientations of conjugate shear fractures. (c) Normalized first strain invariant $\bar{I}_1$. (d) Normalized shear strain $\bar{\varepsilon}_{xy}$.

Similarly, analysis of the $\tilde{C}$ distribution in this system reveals elongated regions of low $\tilde{C}$ values oriented at angles of 35-45° (Fig. 12B). We observe that the orientations of the regions formed by the overlap of high-$\tilde{C}$ lobes concentrated at the tips of individual cracks are similar to those associated with reduced compression. Lobes of high $\tilde{C}$ elongating at low angles relative to the crack direction link multiple cracks arranged in arrays oriented at approximately -15°, whereas lobes of high $\tilde{C}$ elongating at high angle relative to the crack direction mechanically link crack tips at angles of 60-70° (Fig. 12B). In this case, we also observe that the interaction associated with the high-angle lobes of elevated $\tilde{C}$ extends farther from the crack tips, connecting cracks separated by distances of 3-4 times the crack half-length (Fig. 12B). The local trajectories of potential shear fractures effectively connect the tips of adjacent cracks arranged in arrays oriented at approximately -10° to -15°, and those in arrays oriented at -60 to -70° when the crack separation is small (Fig. 12B, insets).

High values of $\bar{I}_1$ concentrate between cracks arranged in arrays oriented at angles between -10° and -40° (Fig. 12C). In this case, due to the different geometry of the regions of high volumetric dilation at the tips of individual cracks compared to those observed for $\tilde{\sigma}_2$ and $\tilde{C}$, interactions between cracks in arrays oriented at lower negative angles are much weaker (Fig. 12C). Symmetrically, volumetric contraction is observed between cracks arranged in arrays oriented at angles between 10° and 40° (Fig. 12C). The perturbation to the strain field appears to affect smaller regions around cracks than those observed for the stress field. Consequently, interactions between regions of high $\bar{I}_1$ require small crack separations and high overlap to occur (Fig. 12C, insets).

Elliptical regions of low $\bar{\varepsilon}_{xy}$ are observed along the major axes of the individual cracks (Fig. 12D). These regions of strain shadowing do not merge into longer regions with distinct orientations. In contrast, shear strain reaches high values between approximately collinear cracks arranged in arrays oriented between -10°

https://doi.org/10.5194/egusphere-2026-4027
Preprint. Discussion started: 6 August 2026

and 10°, forming long chains of mechanically interacting cracks (Fig. 12D). This observation is consistent with the fact that the largest regions of elevated $\bar{\varepsilon}_{xy}$ are shaped as lobes elongating parallel to the crack direction (Fig. 12D, insets). Because of the orientation of the two smaller, symmetrical lobes of high $\bar{\varepsilon}_{xy}$ that extend from the crack tips opposite to the crack direction, crack arrays oriented at ±45° can also interact through the development of narrower regions of elevated shear strain (Fig. 12D, insets).

Fig. 13 illustrates the distribution of $\tilde{\sigma}_2$, $\tilde{C}$, $\bar{I}_1$, and $\bar{\varepsilon}_{xy}$ in the system containing randomly located and randomly oriented cracks ($RanDeg = 1$). Additional configurations with intermediate degrees of crack alignment ($RanDeg = 0.25, 0.5$) are illustrated in Figures A8 and A9 In this configuration, analysis of the $\tilde{\sigma}_2$ distribution reveals multiple interference patterns. Sub-horizontally aligned cracks ($\vartheta_i \approx 0°$) arranged in arrays oriented at approximately -15°, and sub-vertically aligned cracks ($\vartheta_i \approx 90°$) arranged in arrays oriented at approximately -75°, interact through the overlap of regions of elevated $\tilde{\sigma}_2$ that emanate asymmetrically from their tips relative to the crack direction (Fig. 13A; see also Fig. 2B, Fig. 3A, and Fig. 5A). Cracks aligned with the orientation of $\vec{\sigma}_1^{\infty}$ and arranged in arrays oriented at angles ranging from -30° to -60° interact through the overlap of the symmetrical lobes at their tips, forming chains subparallel to the far-field maximum compressive stress (Fig. 13A; see also Fig. 2A). Cracks oriented at 45°, owing to the geometry of the regions of elevated $\tilde{\sigma}_2$ surrounding them (Fig. 2A), do not interact efficiently within long arrays. However, in some regions of the domain, the stress perturbations they induce may act as bridges that facilitate the overlap of regions of elevated $\tilde{\sigma}_2$ around differently oriented cracks (Fig. 13A). Analysis of the principal stress trajectories reveals that, in arrays of cracks with $\vartheta_i \approx 90°$ oriented at approximately -75°, the tips of adjacent cracks are effectively connected by the local trajectories of $\vec{\sigma}_1$, similarly to the arrays of cracks with $\vartheta_i \approx 0°$ oriented at approximately -15° discussed in the previous section (Fig. 13A, insets). In contrast, for cracks with $\vartheta_i \approx -45°$, the local trajectories connect neighboring crack tips only when cracks are nearly collinear, such that only arrays oriented at approximately -45° appear geometrically favorable for coalescence (Fig. 13A, insets).

https://doi.org/10.5194/egusphere-2026-4027
Preprint. Discussion started: 6 August 2026

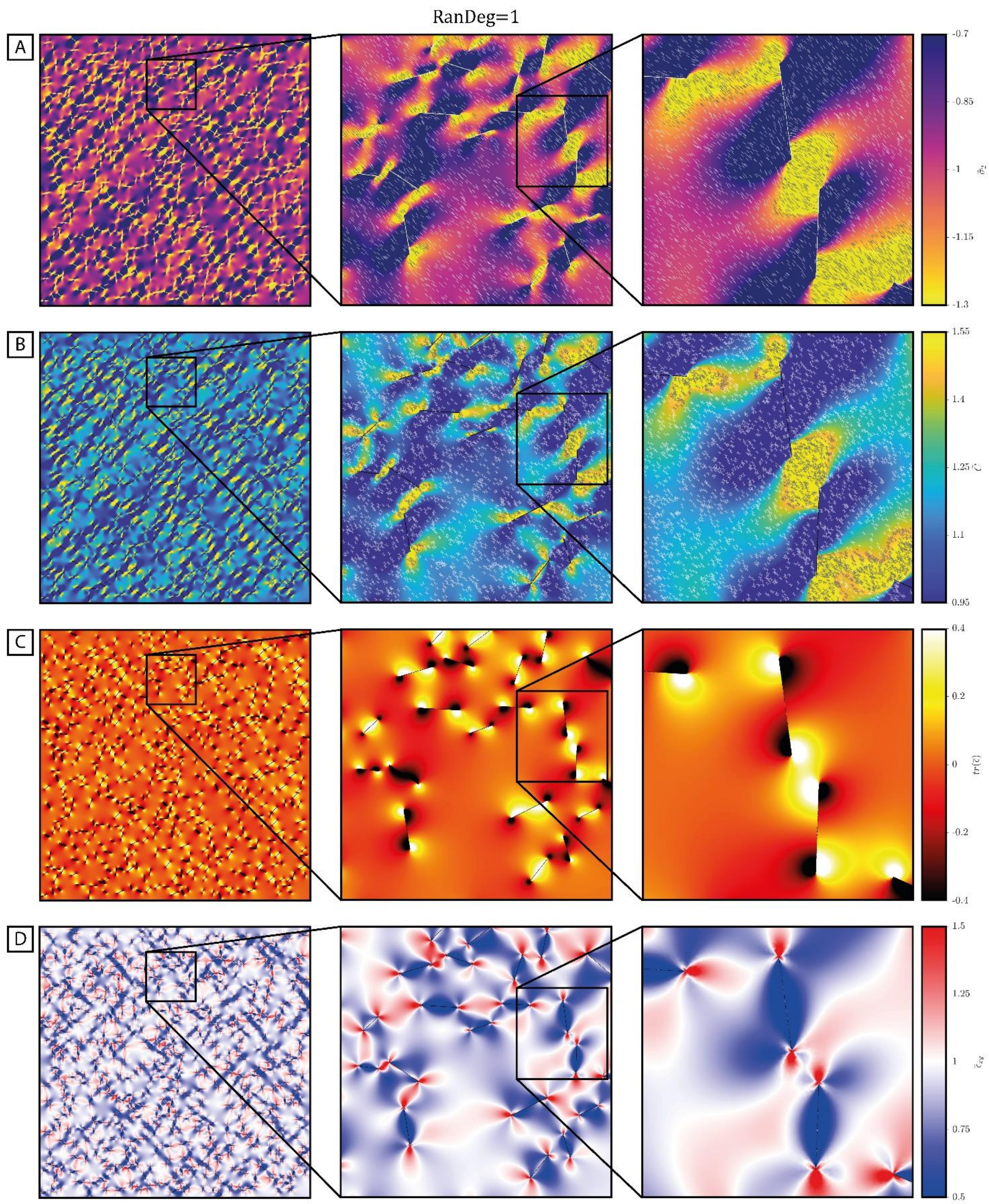

Fig. 13: Stress and strain fields in a system containing 500 randomly oriented cracks ($RanDeg = 1$) with random locations. In each row, the first inset illustrates a subdomain containing mechanically interacting cracks with different orientations. The second inset shows the interaction between the tips of two aligned cracks. (a) Magnitude of the minor in-plane principal stress $\tilde{\sigma}_2$. White and black lines represent the local

https://doi.org/10.5194/egusphere-2026-4027
Preprint. Discussion started: 6 August 2026

trajectories of the major in-plane principal stress $\vec{\sigma}_1$. (b) Normalized effective cohesion $\tilde{C}$. White and black lines indicate the potential orientations of conjugate shear fractures. (c) Normalized first strain invariant $\bar{I}_1$. (d) Normalized shear strain $\bar{\varepsilon}_{xy}$.

The distribution of $\tilde{C}$ is essentially similar to that of $\tilde{\sigma}_2$. Arrays of sub-horizontally and sub-vertically aligned cracks oriented at -15° and -75°, respectively, as well as arrays of nearly collinear cracks oriented at approximately -45° produce the greatest overlap between regions of elevated $\tilde{C}$ (Fig. 13B). We observe that the tips of cracks oriented at -45° and arranged in arrays oriented at approximately -15° and -75° are effectively connected by the orientations of the potential shear fractures that may develop within regions of elevated $\tilde{C}$ (Fig. 13B). In addition, horizontally oriented arrays of cracks with $\vartheta_i \approx 30°$ mechanically interact through the development of sigmoidal regions of elevated $\tilde{C}$, within which the orientations of potential shear fractures connect the tips of the neighboring cracks (Fig. 13B, first inset).

Volumetric dilation occurs in arrays of cracks with $\vartheta_i \approx \pm 45°$ oriented at approximately -45°. However, for arrays of cracks with $\vartheta_i \approx -45°$, the narrow, circular geometry of the regions of elevated dilation at their tips requires the cracks to be nearly collinear for the regions of high $\bar{I}_1$ to overlap effectively (Fig. 13C). In contrast, the regions of high $\bar{I}_1$ surrounding cracks with $\vartheta_i \approx 45°$ exhibit broader, elliptical shapes, producing wider perturbation regions in which the cracks do not need to be perfectly aligned within a straight array to interact mechanically (Fig. 13C). We also observe patterns similar to those identified for $\tilde{\sigma}_2$ and $\tilde{C}$: sub-horizontal cracks arranged in arrays oriented at approximately -15°, and sub-vertical cracks arranged in arrays oriented at approximately -75°, mechanically interact through overlap of regions of high $\bar{I}_1$ at their tips (Fig. 13C).

Shear strain tends to concentrate within single-lobe-shaped regions elongating in the crack direction from the tips of sub-horizontal and sub-vertical cracks. Therefore, these concentrations of $\bar{\varepsilon}_{xy}$ at the individual crack tips overlap efficiently when the cracks are arranged in sub-horizontal and sub-vertical arrays, respectively (Fig. 13D). Because the regions of elevated $\bar{\varepsilon}_{xy}$ at the tips of cracks oriented at $\vartheta_i \approx \pm 45°$ are

https://doi.org/10.5194/egusphere-2026-4027
Preprint. Discussion started: 6 August 2026

shaped as double lobes symmetrical with respect to the crack direction, the geometrically favorable array orientations for mechanical interaction are –15° and -75° for cracks with $\vartheta_i \approx -45°$, and 15° and 75° for cracks with $\vartheta_i \approx 45°$ (Fig. 13D).

5. Discussion

The presented numerical results provide valuable insight into how the mechanical interaction between pre-existing cracks depends on their geometry, orientation and spacing. In the following, we discuss the implications of local stress and strain perturbations for potential fracture nucleation, crack linkage and fault development in upper-crustal rocks. First, we consider how confining pressure and pore fluid pressure affect the conditions for crack closure and brittle failure. Then, we examine how geometrically controlled stress perturbations may promote or inhibit crack coalescence, and how crack-scale interactions can be related to the development of larger fracture networks and faults. Finally, we compare some of the model results with geological structures observed in nature.

5.1 From reduced to normalized effective stresses: the potential for tensile failure under crustal lithostatic and pore pressure conditions

In the presented models, stress values are reduced and normalized, allowing the results to be interpreted independently of a specific ambient stress magnitude. The confining lithostatic pressure component is subtracted to isolate the stress perturbation due to the presence of cracks under an increment of the far-field simple shear. Negative values of the reduced minor in-plane principal stress correspond to regions of reduced compression, which may embed sites of effective tension depending on the balance between confining pressure, local pore pressure and the applied far-field deviatoric stress. However, to assess whether a given value of reduced stress is sufficient to promote tensile crack growth or fracture nucleation, the normalized values must be converted into dimensional effective stresses based on the crustal depth ranges of interest.

https://doi.org/10.5194/egusphere-2026-4027
Preprint. Discussion started: 6 August 2026

A first-order conversion can be obtained by assuming a lithostatic pressure state, according to Heim's rule (Milnes, 1979), and upper-crustal rock densities of approximately 2600–2800 kg/m^3, that correspond to a lithostatic gradient of about 27 MPa/km. For a homogeneous hydrostatic pore pressure increasing at approximately 10 MPa/km, the background effective confining pressure is

$$P_{eff}\,[MPa] = P^{\infty} - P_f \approx 17 \cdot z\,[km] \quad (15)$$

Where z is depth expressed in kilometers and the resulting P_{eff} in MPa. This background effective pressure is independent of crack orientation, and the effective stresses at a given depth can be obtained by adding P_{eff} to the calculated reduced stresses upon scaling them with the postulated far-field shear stress.

For the elastic parameters and boundary conditions used in the present work, the prescribed increment of far-field simple shear produces a dimensional differential stress of 48 MPa. Therefore, a normalized reduced stress of a negative unit value ($\tilde{\sigma}_2 = -1$) corresponds to a local reduction of the minor in-plane principal stress of 24 MPa relative to the unperturbed background value due to the ambient lithostatic pressure. In contrast, positive values of $\tilde{\sigma}_2$ indicate elevated compression. Depending on the presumed depth and pore pressure conditions, the same reduced and normalized stress value may correspond to different effective stresses and mechanical outcomes.

Threshold values of $\tilde{\sigma}_2$ within regions of reduced compression include -2, -4, and -10. The value $\tilde{\sigma}_2 \approx -2$ corresponds to the threshold commonly used in maps of the spatial distribution of $\tilde{\sigma}_2$ magnitudes. Values around $\tilde{\sigma}_2 \approx -4$ represent the approximate minimum reached at the midpoint between neighboring underlapping cracks, $\tilde{\sigma}_2^m$, whereas values approaching $\tilde{\sigma}_2 \approx -10$ correspond to the strongest midpoint minima obtained for overlapping crack configurations. With the presumed far-field tectonic shear stress, which dictates the dimensional scaling adopted here, these values of $\tilde{\sigma}_2$ correspond to local reductions of the minor in-plane principal stress of approximately 48, 96 and 240 MPa, respectively.

Tensile failure can occur without fluid overpressure only where the local stress reduction is sufficiently large to overcome both the hydrostatic effective confining pressure and the tensile strength of the rock (Brace et al., 1968; Paterson and Wong, 2005; Brantut et al., 2013). Here, fluid overpressure refers to pore fluid

https://doi.org/10.5194/egusphere-2026-4027
Preprint. Discussion started: 6 August 2026

pressure exceeding the hydrostatic pressure at a given depth (Osborne and Swarbrick, 1997). Assuming a tensile strength of $T_0 = 10$ MPa representative for intact rocks (Miskovsky, 2011), the approximate condition for tensile failure under hydrostatic pore fluid pressure is

$$17 \cdot z\ [km] + 24\tilde{\sigma}_2\ [MPa] < -T_0\ [MPa] \quad (16)$$

Accordingly, a stress reduction of $\tilde{\sigma}_2 \approx -2$ may be sufficient to exceed the tensile strength only within the top 2 km of the crust (Fig. 14A). Values around $\tilde{\sigma}_2 \approx -4$, and especially $\tilde{\sigma}_2 \approx -10$, which are locally reached at the midpoints between cracks, may remain sufficient to promote tensile failure to greater depths (Fig. 14A). Between 5 and 10 km, values of $\tilde{\sigma}_2 \approx -2$ would require significant pore fluid overpressure, whereas values around $\tilde{\sigma}_2 \approx -4$ may induce tensile failure mainly in the shallower part of this interval (Fig. 14A). In contrast, values around $\tilde{\sigma}_2 \approx -10$ still exceed the tensile strength under hydrostatic conditions (Fig. 14A). At depths greater than 10 km, within typical upper-crustal seismogenic conditions (Faulkner et al., 2010), only values close to $\tilde{\sigma}_2 \approx -10$ would allow the stress state between cracks to approach effective tension without substantial overpressure, although some degree of overpressure would certainly be required below depths of approximately 12 km.

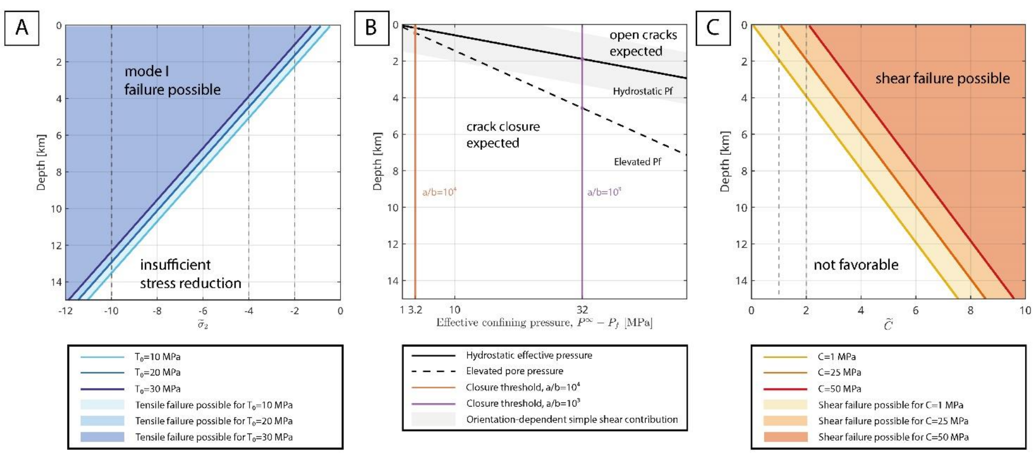

Fig. 14: Mechanical conditions for tensile failure, crack closure and shear failure under upper-crustal effective pressure conditions. (a) Critical magnitude of reduced and normalized minor in-plane principal stress, $\tilde{\sigma}_2$,

https://doi.org/10.5194/egusphere-2026-4027
Preprint. Discussion started: 6 August 2026

required for mode I tensile failure for $T_0 = 10, 20, 30$ MPa. The shaded regions represent stress conditions where tensile failure is possible, and vertical dashed lines show representative model outputs of $\tilde{\sigma}_2$. (b) Effective confining pressure ($P^{\infty} - P_f$) as a function of depth for hydrostatic pore pressure and for a possible elevated pore pressure gradient. The grey band illustrates the orientation-dependent simple shear contribution to the effective stress component acting normal to the crack walls. Vertical lines represent normal stress thresholds for crack closure (for cracks with aspect ratios $\frac{a}{b} = 10^4, 10^3$). (c) Critical reduced and normalized cohesion $\tilde{C}$ required for shear failure for rocks with cohesion of C=1, 25, and 50 MPa. Shaded regions indicate conditions where shear failure is possible. Vertical dashed lines mark representative model ranges of $\tilde{C}$.

In the shallow upper crust, or in deeper regions affected by elevated pore fluid pressure, the local reduction of the least compressive stress observed in the models may locally result in effective tensile stresses exceeding rock tensile strength, which promotes tensile fracture growth. For typical tectonic stress values up to a few tens of MPa, the moderate values of reduced $\tilde{\sigma}_2$ between -2 and -4 are mainly relevant at shallow depths, whereas the strongest local minima, approaching -10, may produce sites prone to tensile failure over a broader depth range. Since the values of $\tilde{\sigma}_2$ discussed here are evaluated at the midpoints between neighboring cracks, where the influence of individual crack-tip singularities is reduced, the analyzed potential for tensile linkage between multiple cracks is underestimated.

5.2 Crack closure and pore fluid pressure

A key assumption of the presented models is that cracks are represented as highly elongated, frictionless elliptical voids. This approximation builds on the classical framework of an elliptical hole in an infinite medium, in which local stress perturbations are controlled by the aspect ratio of the cavity and the far-field loads (Pollard and Segall, 1987; Jaeger et al., 2009). Elliptical voids approximate slit cracks in the limit of high aspect ratio, while avoiding the stress singularity associated with an ideal sharp crack tip, which is generally

https://doi.org/10.5194/egusphere-2026-4027
Preprint. Discussion started: 6 August 2026

difficult to resolve accurately in standard numerical models. In our study, this numerical approach is used to investigate the stress perturbations and interference introduced by persistently open cracks away from the immediate near-tip region. We therefore avoid directly addressing challenging processes such as partial or complete crack closure, contact mechanics between rough crack walls, frictional slip, and mineral sealing. Nonetheless, natural cracks in the upper crust may be voids, open and fluid-filled, closed or sealed by minerals, as well as undergoing frictional sliding, depending on the far-field loads and pore fluid pressure that determine the effective normal stress acting on the crack walls (Brace et al., 1968; Kranz, 1983; Brantut et al., 2013; Anders et al., 2014). The present results therefore describe the elastic stress field around mechanically open, traction-free cracks, but not around closed or partially closed cracks that can transmit normal stress and experience frictional slip. In the following, we inspect the limitations introduced by this assumption.

At first order, crack closure is governed by the effective normal stress acting across the crack walls:

$$\sigma'_n = \sigma_n - P_f \quad (17)$$

where σ_n is the total normal stress resolved across the crack and P_f is the internal pore fluid pressure. If $\sigma'_n > 0$, the crack is under effective compression and tends to close. If $\sigma'_n < 0$, pore fluid pressure exceeds the compression resolved at the crack walls, and hydraulic fracturing may occur at the crack tip. Thus, the simplest idealized condition to ensure crack opening would be the state of hydraulic overpressure $P_f > \sigma_n$ for all the cracks in the considered system, even though an elliptical crack with a finite initial aperture (aspect ratio) does not require the effective normal stress to vanish completely to remain partially open.

A more realistic condition for complete crack closure under the plane strain approximation builds on the elastic model (Jaeger et al., 2009):

$$\sigma_\perp^\infty = \frac{G}{1-\nu}\frac{b}{a} \quad (18)$$

https://doi.org/10.5194/egusphere-2026-4027
Preprint. Discussion started: 6 August 2026

where $\sigma_{\perp}^{\infty}$ is the far-field normal stress acting perpendicular to the crack walls that is sufficient for closing a slit crack of aspect ratio a/b, which is embedded in an elastic medium with shear modulus G and Poisson's ratio ν.

For the common elastic parameters of rocks that are invoked in this study, (E=60 GPa, ν=0.25), the shear modulus is G=24 GPa. Microcracks in rocks are typically highly elongated and under vanishing effective loads exhibit aspect ratios b/a in the range between 10^{-4} and 10^{-3} (Feves and Simmons, 1976; Kranz, 1983). Hence, the estimated far-field effective normal stress acting perpendicular to the crack walls needed for complete (all cracks within the postulated range of aspect ratios) crack closure yields:

$$\sigma_{\perp c}^{\infty} \approx 32\ MPa \quad (19)$$

Before considering the effects due to a tectonic increment of simple shear, this threshold can be compared with the background effective pressure introduced in Section 5.1. Under lithostatic loading and hydrostatic pore fluid pressure (Eq. 15), closure thresholds of 3.2 and 32 MPa are reached at approximate depths of

$$z_c \approx \frac{3.2}{17} \approx 0.2\ km \quad (20)$$

and

$$z_c \approx \frac{32}{17} \approx 1.9\ km \quad (21)$$

respectively. Thus, under hydrostatic pore pressure conditions, very thin cracks with $\frac{b}{a} \approx 10^{-4}$ are expected to close within the upper few hundred meters, whereas cracks with $\frac{b}{a} \approx 10^{-3}$ may remain partially open up to depths approaching 2 km (Fig. 14B). Cracks with larger apertures would require greater effective compression for complete closure.

At greater depths, maintaining open cracks requires pore fluid pressure above hydrostatic values, such that

$$P^{\infty} - P_f < \frac{G}{1-\nu}\frac{b}{a} \quad (22)$$

or equivalently,

https://doi.org/10.5194/egusphere-2026-4027
Preprint. Discussion started: 6 August 2026

$$P_f > P^{\infty} - \frac{G}{1-\nu}\frac{b}{a} \quad (23)$$

Fluid overpressure may occur if fractures are hydraulically isolated, permeability is reduced, or fluid production exceeds drainage (Brace et al., 1968; Kranz, 1983; Paterson and Wong, 2005; Brantut et al., 2013). This limitation is particularly relevant for *en echelon* crack systems, because mechanical models of *echelon* veins show that vein spacing, the relative orientation between veins and arrays, elastic stiffness, internal crack pressure, and the closing of intersecting pressure-solution seams can all influence crack opening and near-tip stress fields (Seyum and Pollard, 2016). In particular, the closing of pressure-solution seams may modify the mechanical interaction between adjacent open veins, alter the opening distribution along the veins, and promote straighter propagation paths.

In the present models, which simulate the stress field due to a simple shear increment of γ=10^{-3}, the induced far-field shear stress is approximately $\tau^{\infty} = G\gamma \approx 24\ MPa$.

The normal stress increment acting perpendicular to a crack is

$$\sigma_{\perp}^{\infty} = \sigma_1^{\infty}\cos^2\beta + \sigma_2^{\infty}\sin^2\beta \quad (24)$$

where σ_1^{∞} and σ_2^{∞} are the reduced major and minor in-plane far-field principal stresses, equal to 24 and -24 MPa, respectively, and β is the angle between the ellipse minor-axis direction, normal to the crack walls, and the far-field maximum compressive stress direction $\vec{\sigma}_1^{\infty}$.

Since $\vec{\sigma}_1^{\infty}$ is oriented at -45° under right-lateral simple shear, the angle ϑ between the major axis of the cracks and the horizontal is related to β as follows:

$$\beta = \vartheta - 45° \quad (25)$$

The tectonic normal-stress increment can therefore be written as

$$\sigma_{\perp}^{\infty} = G\gamma\sin 2\vartheta \quad (26)$$

https://doi.org/10.5194/egusphere-2026-4027
Preprint. Discussion started: 6 August 2026

For the $\frac{b}{a} \approx 10^{-4}$ cracks used in the *en echelon* models, and considering only the reduced far-field stress generated by the prescribed simple shear, and neglecting both confining pressure and pore fluid pressure, the closure threshold is exceeded for:

$$3.8° \lesssim \vartheta \lesssim 86.2° \quad (27)$$

When the depth-dependent background effective pressure is also included, the condition required to prevent complete closure becomes:

$$P_f > P^{\infty} + \sigma_{\perp}^{\infty}(\vartheta) - \frac{G}{1-\nu}\frac{b}{a} = P^{\infty} + G\gamma \sin 2\vartheta - \frac{G}{1-\nu}\frac{b}{a} \quad (28)$$

This relation shows that the pressure required to keep a crack open depends not only on depth and pore fluid pressure, but also on crack orientation, aspect ratio and elastic parameters of the rock undergoing deformation.

This distinction is important because open and closed cracks produce different near-tip stress fields. Open cracks concentrate tensile stresses and promote mode I crack propagation, whereas closed cracks may reactivate by frictional sliding or mixed-mode propagation, generating different wing crack angles (Brace and Bombolakis, 1963; Pollard and Fletcher, 2005; Lee et al., 2022).

It is also important to distinguish the role of pore pressure in macroscopic failure criteria from its role at the individual crack scale. In macroscopic failure criteria, pore pressure is usually treated as an isotropic contribution to the stress tensor $\boldsymbol{\sigma}'$:

$$\boldsymbol{\sigma}' = \boldsymbol{\sigma} - P_f\mathbf{I} \quad (29)$$

where $\mathbf{I}$ is the identity tensor. In this framework, pore pressure decreases the mean stress and shifts Mohr circles toward lower effective normal stress, without directly affecting the deviatoric stress tensor.

At the crack scale, pore fluid pressure acts as a normal traction on discrete crack walls, inducing elastic strain in the surrounding medium. Unless pore fluid pressure in all cracks exactly matches the ambient lithostatic pressure, producing purely volumetric deformation in a homogeneous material, this results in an elastic

https://doi.org/10.5194/egusphere-2026-4027
Preprint. Discussion started: 6 August 2026

perturbation in the surrounding medium which includes deviatoric components. Directly including internal crack pressure in the future models would allow for assessing the closure of individual cracks as well as quantifying the local stress perturbation associated with the difference between the pore fluid pressure and the overall lithostatic pressure.

5.3 Cohesion and pressure-dependent shear failure

As confining pressure increases, cracks tend to close, and frictional sliding is likely to occur. Shear failure is controlled by the balance between differential and normal stress, pore fluid pressure, cohesion and angle of internal friction (Brace and Bombolakis, 1963; Paterson and Wong, 2005; Brantut et al., 2013; Lee et al., 2022). The dependence of shear failure on pressure is consistent with laboratory observation showing that shear fracturing becomes increasingly important at higher confinement, particularly on the verge of macroscopic failure (Stanchits et al., 2006; Graham et al., 2010; McBeck et al., 2023). The interpretation of the obtained results depends on the comparison between the estimated local effective cohesion threshold values and realistic values of rock cohesion.

To evaluate potential shear failure in regions located between the cracks, we used the Mohr-Coulomb criterion with a representative angle of internal friction of $\phi = 35°$, consistent with typical values for unweathered upper-crustal rocks. The model output $\tilde{C}$ may be interpreted as the reduced and normalized value of the cohesion that a rock would need to avoid shear failure under a specific local stress state. Therefore, if the cohesion of the rock is lower than the dimensional value of $\tilde{C}$ for a given set of lithostatic and pore fluid pressures, shear fracture nucleation may occur along the orientations predicted by the Mohr-Coulomb criterion. Therefore, high values of $\tilde{C}$ identify regions where the local stress perturbation strongly favors shear failure.

Given the boundary conditions used in the present study, the conversion of $\tilde{C}$ to a dimensional cohesion threshold C_{eff} (in MPa) is performed as follows:

https://doi.org/10.5194/egusphere-2026-4027
Preprint. Discussion started: 6 August 2026

$$C_{eff}(z)[MPa] = 24 \cdot \tilde{C}\ [MPa] - \left(P^{\infty}(z) - P_f(z)\right)\tan\phi\ [MPa] \quad (30)$$

Where z is depth. Assuming, as in the previous section, an internal friction angle $\phi = 35°$, a lithostatic gradient of 27 MPa and hydrostatic pore fluid pressure of approximately 10 MPa, the expression for C_{eff} becomes:

$$C_{eff}(z)[MPa] \approx 24 \cdot \tilde{C}\ [MPa] - 12 \cdot z\ [km] \quad (31)$$

In the *en echelon* crack models, about 11% of the considered geometrical configurations lead to a value of $\tilde{C} < 1$ at the midpoint between neighboring cracks. These values correspond to local stress states that may be unfavorable for shear failure. In these configurations, the stress perturbation induced by the presence of the cracks tends to inhibit shear failure activation, particularly when confining pressure is considered. In most configurations (about 70% of the studied setups), $1 < \tilde{C} < 2$. These values of $\tilde{C}$ correspond to local stress states which may be moderately favorable for the activation of shear failure. These configurations may promote shear failure, especially where confinement is low, pore fluid pressure is elevated, or the host rock is poorly consolidated. The remaining configurations have $\tilde{C} > 2$, reaching values of up to 8 in a few configurations. These high values correspond to local stress states that may be favorable for shear failure development due to stress perturbations between the interacting microcracks. In these cases, the stress perturbation may promote shear failure even in rocks with relatively high cohesion, although effective pressure still controls the feasible depth range.

These ranges of $\tilde{C}$ can be compared with representative values of cohesion for different lithologies. Weak or highly damaged rocks may have cohesion values of the order of 1 MPa, as reported for low-strength wet mudstones (Winn et al., 2017). Moderately strong rocks may be represented by C≈25 MPa, consistent with cohesion values measured for intact mudstone, pyroclastic rocks or granite. Strong rocks may reach C≈50 MPa, as reported for measured values of high strength crystalline or diabase samples (Winn et al., 2017; Chen et al., 2023). These values are taken as reference cohesion levels to assess the possibility of shear failure at confining pressures and ranges of $\tilde{C}$.

https://doi.org/10.5194/egusphere-2026-4027
Preprint. Discussion started: 6 August 2026

In the shallow upper crust, between 0 and 5 km depth (corresponding to an increase of effective pressure from 0 to about 60 MPa under hydrostatic pore fluid pressure), for very weak or highly damaged rocks with C≈1 MPa, even model configurations that yield values of $\tilde{C} < 1$ may promote shear failure down to approximately 2 km depth, whereas the range $1 < \tilde{C} < 2$ may remain favorable down to approximately 4 km (Fig. 14C). For rocks of moderate cohesion (C≈25 MPa), configurations with $\tilde{C} < 1$ are insufficient to favor shear failure near the surface, whereas configurations with $1 < \tilde{C} < 2$ may promote it down to about 2 km (Fig. 14C). Stronger rocks (C≈50 MPa) generally require $\tilde{C} > 2$ to generate stress states favorable enough for shear failure within this depth range (Fig. 14C).

Between 5 and 10 km depth, the effective pressure term increases from about 60 to 120 MPa under hydrostatic pore fluid pressure. Therefore, configurations with $\tilde{C} < 1$ are not favorable for shear failure development, even in very weak rocks, whereas most configurations within the range $1 < \tilde{C} < 2$ become effective only if the rock is very weak, or for pore fluid pressure above hydrostatic values (Fig. 14C). For rocks of moderate cohesion, in this depth range, shear failure requires values close to $\tilde{C} \approx 2$ or even higher (Fig. 14C). Stronger rocks, with C≈50 MPa, require $\tilde{C} \gtrsim 4 - 7$, unless pore fluid pressure approaches lithostatic pressure (Fig. 14C).

At depths higher than 10 km, which correspond to the base of the typical seismogenic zone in the upper crust, the effective pressure correction is larger than 120 MPa. Therefore, configurations with $\tilde{C} < 4$ are not favorable for shear fracture nucleation under hydrostatic pore pressure and the presumed level of tectonic load (Fig. 14C). At these depths, shear failure in weak to moderately cohesive rocks requires either substantially higher values of $\tilde{C} > 5 - 6$ or pore fluid pressure significantly above hydrostatic values (Fig. 14C). Strong rocks, with C≈50 MPa, require values of $\tilde{C}$ close to the highest values observed in the models, approximately $\tilde{C} > 7$ at 10 km depth (Fig. 14C). At greater depths, even these configurations would require elevated pore fluid pressure, potentially approaching lithostatic pressure, to remain favorable for shear failure.

https://doi.org/10.5194/egusphere-2026-4027
Preprint. Discussion started: 6 August 2026

The dependence of the Mohr-Coulomb shear failure estimates on depth can be compared with that for mode I failure in Section 5.1. Under hydrostatic pore-pressure conditions, increasing depth corresponds to increased effective confining pressure, so larger stress perturbations are required to induce either tensile or shear failure (Brace and Bombolakis, 1963; Paterson and Wong, 2005; Jaeger et al., 2009; Brantut et al., 2013). For example, at 5 km, tensile failure for $T_0 = 10\ MPa$ requires approximately $\tilde{\sigma}_2 \lesssim -4$, whereas shear failure requires $\tilde{C} \gtrsim 2.5$ for a very weak rock with ($C \approx 1\ MPa$) and $\tilde{C} \gtrsim 3.5$ for a rock with ($C \approx 25\ MPa$). At 10 km, the corresponding thresholds increase to approximately $\tilde{\sigma}_2 \lesssim -7.5$, $\tilde{C} \gtrsim 5$, and $\tilde{C} \gtrsim 6$, respectively. Thus, the commonly observed range ($1 < \tilde{C} < 2$) is mainly relevant for shallow depths and rocks with low cohesion, whereas only the highest values of $\tilde{C}$ obtained in the models remain sufficient for shear failure near the base of the upper-crustal seismogenic zone under hydrostatic conditions. Poor fluid pressure above hydrostatic values reduces the effective normal stress and expands the depth range over which both tensile and shear failure may occur.

5.4 Geometry-controlled stress interference and crack coalescence

Our numerical results indicate that the geometry of pre-existing cracks strongly influences the location, magnitude and orientation of stress perturbations that may promote fracture nucleation and crack linkage. This is consistent with the general view that brittle failure in rocks is not controlled only by the far-field stress, but also by the local stress concentrations generated by flaws, pores, grain boundaries, cracks and other discontinuities (Griffith, 1920; Brace and Bombolakis, 1963; Pollard and Fletcher, 2005; Anders et al., 2014). This interpretation is also consistent with studies of fault process zones, where microfracture density and orientation are interpreted as records of altered stress fields around propagating fault tips (Vermilye and Scholz, 1998; Wilson et al., 2003; Mitchell and Faulkner, 2009).

The analysis of the *en echelon* models shows that arrays inclined at equal but opposite angles relative to the crack direction produce significantly different stress interactions between neighboring crack tips. For some geometries, decreasing separation promotes the overlap of regions of reduced compression between

https://doi.org/10.5194/egusphere-2026-4027
Preprint. Discussion started: 6 August 2026

adjacent crack tips. In these cases, the local stress state may approach effective tension if the reduction in the minor in-plane principal stress is sufficiently large relative to the confining and pore pressure conditions (see Sec. 5.1). This behavior agrees with the general crack interaction framework proposed by Reches and Lockner (1994), who argued that macroscopic shear fractures may originate from the overlap of tensile stress concentrations between cracks originated in mode I. However, our results extend this concept by demonstrating that favorable stress conditions are not restricted to cracks initially parallel to $\vec{\sigma}_1^{\infty}$. Instead, we argue that cracks with different orientations, especially mode II-oriented cracks, may generate asymmetric lobes of reduced compression, which are particularly effective in generating linking paths oblique relative to the direction of $\vec{\sigma}_1^{\infty}$. These regions of reduced compression are particularly important because they can define potential pathways for local mode I crack growth leading to macroscopic fracture linkage. This interpretation is consistent with experimental and theoretical studies in which macroscopic shear fractures develop through the interaction and coalescence of tensile microcracks, while in-plane mode II propagation is strongly inhibited (Brace et al., 1966; Scholz, 1968; Petit and Barquins, 1988; Reches and Lockner, 1994; Healy et al., 2006). Besides the magnitude of reduced compression that controls the potential of locally shifting the effective stress into the tensile regime, the orientation of the local principal stress trajectories is also essential to infer crack linkage, because mode I fractures are expected to propagate perpendicular to the local least compressive principal stress (parallel to the local maximum compressive principal stress). Therefore, direct tensile crack coalescence could be problematic within overlapping lobes of reduced compression with local $\vec{\sigma}_1$ trajectories that do not connect adjacent crack tips. This is consistent with Healy et al. (2006), who showed that the elastic interaction between finite three-dimensional mode I cracks may produce tensile linkage paths oblique to $\vec{\sigma}_1^{\infty}$. Our models show that comparable conditions may also develop around mode II-oriented cracks. A specific example is provided by horizontal cracks arranged in *en echelon* arrays at $\varphi = -15°$, for which overlapping lobes of reduced compression and local $\vec{\sigma}_1$ trajectories connect adjacent tips at intermediate values of crack separation (Figs. 3, 5).

The opposite behavior occurs in geometries where the region between adjacent cracks is characterized by elevated compression. In these configurations, decreasing crack separation does not necessarily promote

https://doi.org/10.5194/egusphere-2026-4027
Preprint. Discussion started: 6 August 2026

linkage. Instead, the interaction between crack tips may inhibit coalescence because of locally increased compression across the potential linkage region. This demonstrates that crack clustering is not automatically favorable for fault formation. Depending on their relative arrangement and orientation, closely spaced cracks may form mechanically linked arrays or represent regions of increased resistance to brittle deformation.

Models with randomly distributed cracks extend these observations to more realistic systems. Even in these models, in which cracks are not arranged into periodic arrays, favorable mechanical interactions emerge, where local crack subsets resemble *en echelon* geometries. In the models with aligned cracks, overlapping reduced-compression lobes define arrays oriented predominantly at approximately -10° to -18° relative to the crack direction, with additional alignments at higher angles. These orientations are compatible with common macroscopic shear-fracture orientations relative to $\vec{\sigma}_1^{\infty}$. This result provides a micro-mechanical analogue for field observations of faults initiating from sheared joints, *en echelon* joint zones, splays and discontinuous slip surfaces that progressively link with increasing deformation (Shipton and Cowie, 2001; Shipton and Cowie, 2003; de Joussineau and Aydin, 2007). These models suggest that apparently disordered crack systems may contain local geometrical arrangements that favor the early localization of fractures.

In the models with randomly oriented cracks, the most perturbed regions are associated with specific crack orientations and arrangements. In particular, regions of reduced compression surrounding the crack tips form around each isolated crack, but overlaps between these regions and pathways for potential macroscopic fracture coalescence ultimately only develop if multiple of these cracks are aligned and arranged in oriented arrays. In addition, only in a subset of these configurations also the local deflected trajectories of $\vec{\sigma}_1$ connect the tips of neighboring cracks, thus suggesting possible direct linkage. This is consistent with field studies of damage zones, which show that fracture density and fracture orientation vary systematically with distance from fault cores and with proximity to fault tips, auxiliary faults and geometrical irregularities (Wilson et al., 2003; Mitchell and Faulkner, 2009). It is also consistent with numerical models of off-fault damage, which show that local slip gradients and stress concentrations can lead to the formation of tensile fractures at some distance from the main fault surface (Savage and Cooke, 2010). Therefore, within an apparently disordered crack system, only subsets of favorably oriented and favorably positioned cracks may

https://doi.org/10.5194/egusphere-2026-4027
Preprint. Discussion started: 6 August 2026

control the initial localization of fracture growth. This may explain why macroscopic fault zones emerge from distributed damage while preserving preferred orientations.

These results suggest that the orientation of an emerging macroscopic fracture may be controlled by the spatial arrangement of mechanically interacting cracks and by the stress perturbations that they generate. The Mohr-Coulomb criterion can then be applied to the locally perturbed stress field to identify favorably oriented planes for shear failure or frictional sliding. The subsequent macroscopic fracture orientation may result from the progressive linkage of these locally favorable planes and pre-existing cracks, rather than being determined exclusively by the homogeneous far-field stress. This is compatible with the observation that shear fractures commonly form at angles predicted by frictional failure criteria, while supporting the interpretation that the underlying mechanisms may involve tensile stress concentration and crack coalescence (Reches and Lockner, 1994; Petit and Barquins, 1988; Healy et al., 2006; Vermilye and Scholz, 1998).

Regions of sufficiently reduced compression may promote mode I fracture growth, whereas regions with high values of $\tilde{C}$ identify locations where the local stress state may satisfy the Mohr–Coulomb criterion. The potential orientations of shear failure are defined relative to the local, rather than far-field, principal stress trajectories. Crack interaction may therefore control both where shear failure is possible and how the locally favorable failure planes are oriented between neighboring tips. Depending on crack geometry, effective pressure and rock strength, tensile and shear failure may act as alternative or complementary linkage mechanisms.

5.5 Bridging crack-scale linkage and step fault growth

The obtained results can be interpreted within a broader framework in which faults progressively develop from the interaction and linkage of structural discontinuities. Natural faults are not simple planar surfaces, but instead usually segmented slip surfaces separated by relay zones, crossed by Riedel shears, and surrounded by damage zones characterized by heterogeneous strain (Faulkner et al., 2010). In this context,

https://doi.org/10.5194/egusphere-2026-4027
Preprint. Discussion started: 6 August 2026

the crack interactions modelled in the present study may be regarded as a simplified mechanical analogue of composite fault zones. Local stress perturbations around the tips of discontinuities may promote the progressive linkage of initially isolated fractures into interconnected structures that accommodate large displacement.

At the process zone scale, the distribution of microfractures around natural faults provides an important analogue for the stress perturbation models presented here. Vermilye and Scholz (1998) showed that densities and orientations of fault-related microfractures are different from those of background microfractures, and interpreted them as products of the perturbed stress field around fault tips. Similarly, Wilson et al. (2003) reported analyses of samples from the Punchbowl fault, in the San Andreas system, and similarly showed that microfracture density and orientation anisotropy increases towards the fault core, suggesting that the fabric of damage zone records both early growth stages and later deformation associated with slip. In the study of Mitchell and Faulkner (2009), several possible mechanical processes contributing to off-fault damage are compared, including Andersonian microcrack coalescence and interaction between faults through wing-crack growth. These studies describe the decay of fault-related damage away from fault cores and tips, providing a field-scale analogue to the decay of stress perturbations away from isolated cracks or crack arrays illustrated in the present models.

The results can also be compared with numerical models in which off-fault damage is driven by local stress concentrations. Savage and Cooke (2010) showed that tensile fracture may form where tangential hoop stresses exceed the tensile strength of the rock, especially near rupture tips where slip gradients are elevated. It was also demonstrated that pre-existing damage contributed to localizing subsequent fracture growth. This is relevant to the present models because pre-existing cracks generate local stress perturbations that may promote either the nucleation of new fractures or the linkage of existing defects into larger structures. These newly formed structures may then further modify the stress field and create favorable pathways for subsequent deformation.

https://doi.org/10.5194/egusphere-2026-4027
Preprint. Discussion started: 6 August 2026

At the mesoscale, a bridge between distributed discontinuities to localized faults is illustrated in two studies by Shipton and Cowie (2001; 2003) about deformation bands and slip surfaces in sandstone. In faults surrounded by damage zones containing deformation bands and unconnected slip surfaces, measurable throw initiates when the connection between individual slip surfaces develops. Stress concentrations may develop around slipping surfaces, increasing shear stress on adjacent regions of the fault and ultimately favoring off-fault damage. In our models, we present stress perturbations around crack arrays, which may define favorable regions for linkage. In both the natural fault systems described by Shipton and Cowie (2001, 2003) and the crack arrays examined here, localized brittle structures do not form as continuous propagating structures, but emerge from the progressive connection of initially scattered discontinuities.

At larger scales, segmented faults and step fault systems show similarities with the presented *en echelon* models, especially in terms of the interaction between fault tips within regions of stress perturbation. Field studies indicate that faults may initiate from sheared joints, *en echelon* vein arrays and discontinuous slip surfaces, before these discrete sets of isolated discontinuities are linked into through-going faults (de Joussineau and Aydin, 2007; Peacock et al., 2017). Numerical models of step faults further show that spacing between fault segments and their degree of overlap strongly control stress perturbations, strain localization, and the development of damage zones between interacting faults (Nabavi et al., 2017; Nunes et al., 2025). These observations are consistent with our results, which demonstrate that crack linkage is controlled not only by their spacing, but by the combined effect of crack-tip separation and the orientation of individual cracks as well as their arrays.

The role of initial structure geometry in the evolution of fault zones and relay zones between fault segments has been discussed in multiple studies. Kristensen et al. (2008) framed the relay zone evolution as a process involving displacement transfer, breaching and eventual incorporation into fault-bounded lenses. Childs et al. (2009) proposed that segmentation and relay-zone geometry partly control the fault zone thickness. This is consistent with the present results, especially with the observation that even small variations in crack orientation, degree of overlap and array orientation strongly affect whether linkage between multiple cracks

https://doi.org/10.5194/egusphere-2026-4027
Preprint. Discussion started: 6 August 2026

is promoted or inhibited. At larger scales, similar geometrical variations may play a crucial role in the development of continuous faults from isolated segments through relay zones.

Comparison with geological structures suggests that different crack linkage mechanisms may be relevant to different fault-zone geometries. Where lobes of effective tensile stress overlap between neighboring discontinuities, linkage may occur through the formation of extensional bridges, pull-apart structures or breached relay zones, as observed in echelon vein arrays and segmented fault systems (Peacock and Sanderson, 1995; Kim et al., 2003; Sanderson and Peacock, 2019). In contrast, in regions where elevated compression concentrates, elevated shear stress may promote linkage through nucleation of shear fractures, for example along pressure-solution seams, cleavage surfaces or phyllosilicate-rich shear fabrics (Seyum and Pollard, 2016; Tesei et al., 2012; Sánchez-Roa et al., 2017).

Overall, the models show that the orientation and spacing of neighboring discontinuities control whether local stress perturbations promote or inhibit their linkage. At larger scales, progressive linkage of mechanically favorable discontinuities may contribute to the development of segmented fault zones and to their progressive evolution into continuous fault structures.

5.6 The role of geometry of pre-existing structures in the fault initiation

The obtained numerical results allow us to speculate on how pre-existing discontinuities influence the brittle faulting process. Rocks constituting the uppermost crust commonly exhibit dominant elastic and brittle (plastic) behavior as opposed to viscous flow of the lower crust (e.g., Nabavi et al., 2017; Casini et al., 2023). The stress field due to elastic deformations in rock media with pre-existing microcracks has a significant impact on the coalescence and growth of macroscopic fractures and, ultimately, faults (Reches and Lockner, 1994; Bobet and Einstein, 1998; Tang et al., 2001; Wong et al., 2001; Aydin and Schultz, 1990; Peacock and Sanderson, 1996; Crider and Peacock, 2004; Chang et al., 2015; Zhou et al., 2015; Scholz, 2019; Zhang et al., 2021; McBeck et al., 2023). Using the different synthetic crack network geometries modeled in this work, we demonstrated that the shape and extent of stress concentration regions are strongly influenced by the

https://doi.org/10.5194/egusphere-2026-4027
Preprint. Discussion started: 6 August 2026

arrangement of the cracks, as well as by their relative size and separation. Different crack array orientations result in variable patterns of stress and strain concentrations, the combination of which may control crack linkage and coalescence into larger fractures.

Fig. 15 compares different crack configurations identified in the numerical models with characteristic linking patterns observed in common geological structures. The rock architecture comprises a range of multi-scale discontinuities that can be approximated by the cracks in our model. These discontinuities span from the micro- to macro-scale, including mineral fabrics, grain boundaries and intragranular microfractures, cleavage and twins, veins and solution seams, bedding, joints and faults.

In *en echelon* arrays where the pre-existing crack set is aligned parallel to $\vec{\sigma}_1^{\infty}$, significant positive interference between regions of reduced compression occurs at angles oriented between 30° and 45° with respect to $\vec{\sigma}_1^{\infty}$, depending on the degree of crack overlap. Typical examples include extensional bridges between faults linked by wing cracks (Fig. 15A; Kim et al., 2003). If the pre-existing cracks are oriented perpendicular to $\vec{\sigma}_1^{\infty}$, the *en echelon* configurations broaden the region of reduced compression across the array, favoring the development of through-going fractures or faults within the pre-existing sets of veins or joints, possibly involving the rotation of these structures (Fig. 15B; e.g., Crider and Peacock, 2004).

However, the largest reductions in compression occur when cracks oriented at ±45° relative to $\vec{\sigma}_1^{\infty}$ are aligned along arrays at approximately 20-30° relative to σ_1 (Fig. 15C,D). Tensile linkage through these arrays may significantly enhance the likelihood of failure and fracture propagation. It should be emphasized that these new fractures opening within regions of reduced compression should be classified as mode I, even if their orientation (ca. 20-30° relative to $\vec{\sigma}_1^{\infty}$) is typical of mode II shear fractures. In other words, fractures forming at 30–35° from the $\vec{\sigma}_1^{\infty}$ direction, as commonly observed in experimental analyses (e.g., Paterson and Wong, 2005; McBeck et al., 2023), cannot be defined a priori as shear fractures. This suggests that mode I microcracks with variable orientations may contribute to the development of mode II macroscopic fractures, which are the most typical structures developing in rock media. The geometry of conjugate (Anderson, 1905) strike-slip, normal, and reverse fault zones represent excellent examples of this process (Fig. 15D). Because

https://doi.org/10.5194/egusphere-2026-4027
Preprint. Discussion started: 6 August 2026

regions of reduced compression appear to be favorable sites for crack opening and linkage, under a random distribution of pre-existing cracks, these geometrically arranged crack arrays are statistically more likely to initiate failure, thereby increasing the probability of fracture formation along these preferential directions. This provides a possible rationale for why, in rocks with a nearly isotropic distribution of discontinuities, the orientation of brittle structures tend to obey the Mohr-Coulomb criterion.

Although regions of reduced compression may represent favorable sites for crack opening and linkage, configurations that are unfavorable for the formation of extensional bridges may still promote fracture development through shear strain localization. Shear strain concentration may become important in contractional bridges or within dense arrays of planar discontinuities that are typical in rocks with strong planar anisotropies. Examples of contractional bridges include cleavage, stylolite, P-planes solution seams and faults with reverse motion bridging low-angle discontinuities (Fig. 15E,F). The overlap of shear strain lobes at these connections may promote rupture. Shear strain amplification can occur both in ascending stepover configurations or, more efficiently, along collinear cracks. The strongest amplification occurs in elongated lobes that branch out parallel to the crack, starting from its tips (Fig. 15E). It follows that the most favorable paths connecting high shear strain areas are vertical and horizontal collections of collinear cracks, along which rupture may be facilitated. Examples of these configurations include mode II fractures linking sets of pre-existing aligned cracks or grain boundaries, or B and Y plane shear zones (Fig. 15E, F). It should be noted that Y planes preferentially develop in phyllosilicate-rich shear zones (e.g., Tesei et al., 2012; Sanchez-Roa et al., 2017; Volpe et al., 2022), as these are dominated by minerals with platy morphologies, where the grain boundaries are commonly aligned along collinear layers.

https://doi.org/10.5194/egusphere-2026-4027
Preprint. Discussion started: 6 August 2026

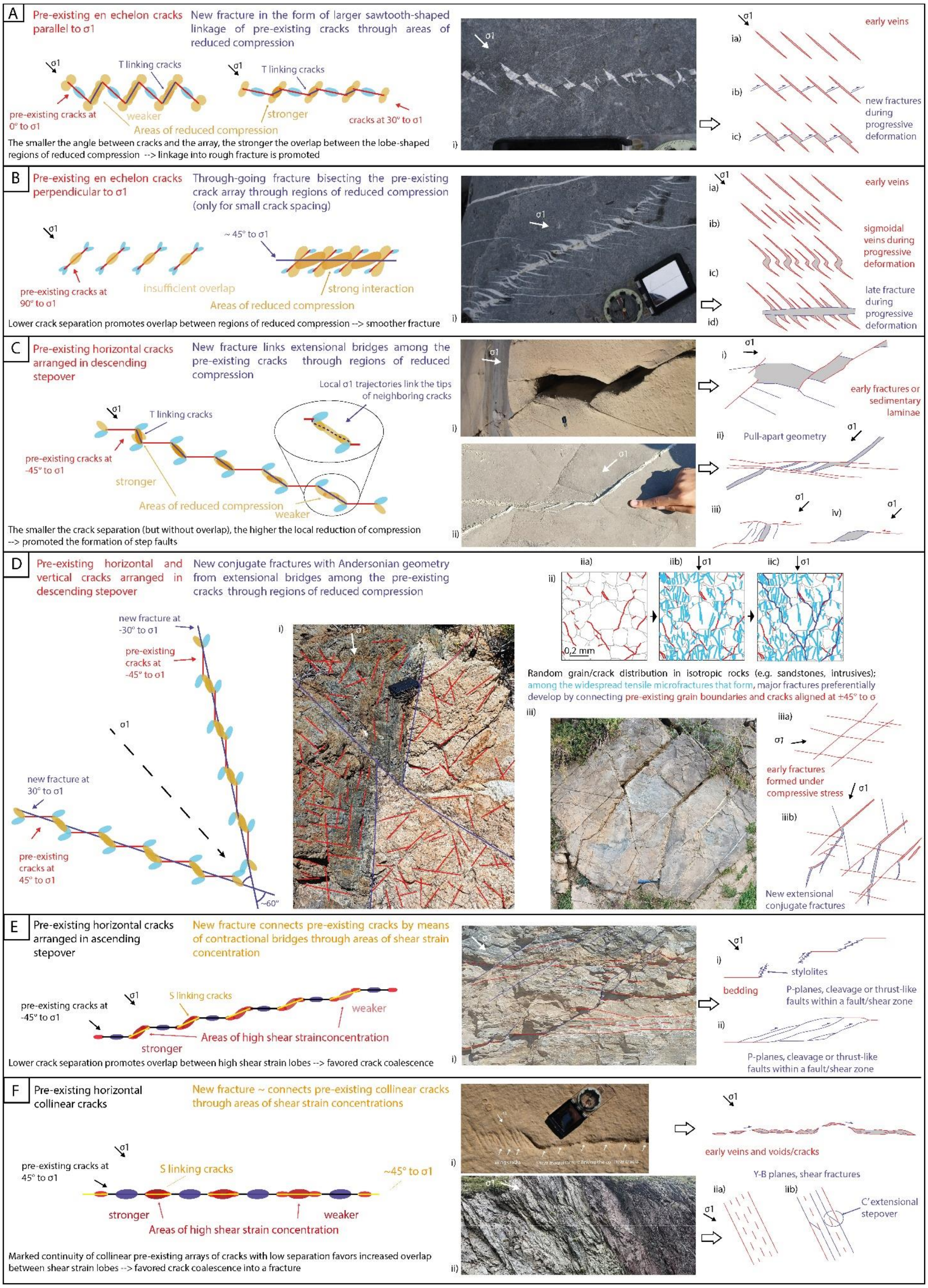

https://doi.org/10.5194/egusphere-2026-4027
Preprint. Discussion started: 6 August 2026

Fig. 15: Comparison between numerical simulations with field examples of fault zones developed through the coalescence of crack networks. (a) Overlap of reduced-compression lobes around *en echelon* cracks parallel to $\vec{\sigma}_1^\infty$ may promote rupture connecting crack tips, resulting in the possible formation of a sawtooth-shaped fracture. A similar geometry is shown in the photograph and associated evolutionary model of an array of calcite-filled pull-aparts linked by shear fractures in the Liassic limestones of Somerset, UK (Peacock and Sanderson, 1995; note that the fault zone is sinistral, but the image is mirrored vertically for an easier comparison; photograph courtesy of D.C.P. Peacock). (b) Overlap of reduced-compression lobes around *en echelon* cracks perpendicular to $\vec{\sigma}_1^\infty$ may promote coalescence through the middle of the crack array. A similar geometry is shown in the photograph (courtesy of D.C.P. Peacock), accompanied by an evolutionary model of an array of rotated *en echelon* calcite-filled veins in the Liassic limestones of Somerset, UK (Peacock and Sanderson, 1995). (c), (d) Overlap of reduced-compression lobes may locally weaken the rock, inducing potential rupture connecting neighboring crack tips. In (c) the configuration of reduced-compression bridges in a step fault is represented by the formation of pull-apart structures; photographs i) and iii) are from Gozo Island, Malta (Kim et al., 2003), ii) from the Ligurian Alps, Italy (Mueller et al., 2023), iv) from Cantil Valley, California, USA (Kim et al., 2004). In (d) the possible formation of conjugate fractures with the typical shear fracture orientation (±30° to $\vec{\sigma}_1^\infty$) but with mode I origin is shown. Bridges with reduced compression arise from random distribution of the pre-existing cracks, from where the arrays of cracks aligned at ±45° to $\vec{\sigma}_1^\infty$ are the most favorable geometrical configurations for the formation of conjugate fault systems following the Anderson (1905) rules. Examples are from a composite fabric of a dike intrusion within a metagranite (photograph from Tenda massif, Corsica, France), ii) a sequential mapping of grain-scale microfractures forming in samples experimentally deformed (modified from Kanaya and Hirth, 2024); tensile fracture (light blue lines) and the pre-existing favorably oriented grain boundaries (red lines) control the formation of the conjugate macroscopic shear fractures. iii) Another field example of sandstones from the Ligurian Alps, Italy (Mueller et al., 2023) showing the development of high-angle conjugate normal faults from the connection of pre-existing sets of conjugate thrust faults through calcite filled veins. Overlap of the shear strain lobes is displayed in (e), with the possible formation of shear fractures (±60° to $\vec{\sigma}_1^\infty$) linking contractional bridges in

https://doi.org/10.5194/egusphere-2026-4027
Preprint. Discussion started: 6 August 2026

limestones of the Ligurian Alps (Manna et al., 2023; Perozzo et al., 2024). (f) Arrays of collinear shear fractures (±45° to $\vec{\sigma}_1^{\infty}$) are shown in the photograph of a right-lateral fault from the west of Marsalforn, Gozo Island, Malta (courtesy of D.C.P. Peacock; Kim et al., 2003) and from a reverse fault in metapelites from the Ligurian Alps (Maino et al., 2020). In all schemes and photographs the pre-existing cracks or bedding are indicated with red lines, the linking new fractures with blue lines, except for the schemes illustrating the shear strain patterns, where pre-existing cracks are indicated with black lines and new fractures with yellow lines.

6. Conclusions

We used two-dimensional FEM-based linear elastic simulations to investigate how different geometries of pre-existing crack networks perturb the local stress and strain fields in a rock undergoing an increment of simple shear deformation. The models show that changes in shape, spacing and orientation of crack arrangements control the spatial distribution of stress and strain perturbations in the regions between neighboring cracks, determining mechanically favorable or unfavorable conditions for crack interaction and potential linkage. In fact, the numerical stress analysis reveals patterns of potentially tensile stress concentration that are closely related to the orientation of pre-existing cracks and may lead to the linkage of cracks into larger fractures. These patterns emerge in two classes of geometrical configurations: (i) *en echelon* cracks and (ii) randomly distributed cracks. From our study, we find that:

1. *En echelon* crack arrangements exhibit local trajectories of the major in-plane principal stress that effectively connect neighboring crack tips in specific configurations: approximately collinear mode I-oriented cracks, and conjugate mode II-oriented crack arrays in which horizontal cracks are arranged in arrays inclined at −15° and vertical cracks along arrays inclined at −75°. In the reference simple shear configuration considered here, where $\vec{\sigma}_1^{\infty}$ is oriented at −45°, these correspond in both cases to array orientations of about 30° from $\vec{\sigma}_1^{\infty}$. These configurations may be favorable for tensile failure-driven crack linkage and suggest that orientations typically associated with shear fractures, approximately ±30° relative to $\vec{\sigma}_1^{\infty}$ as prescribed by the Mohr–Coulomb criterion, may be explained through the preferential activation of crack arrangements that

https://doi.org/10.5194/egusphere-2026-4027
Preprint. Discussion started: 6 August 2026

most effectively reduce the far-field compression. In contrast, their symmetric counterparts relative to the crack orientation, such as horizontal cracks arranged in arrays oriented at 15° and vertical cracks arranged in arrays oriented at 75°, produce elevated compression between neighboring tips and local $\vec{\sigma}_1$ trajectories that do not connect the tips, thereby inhibiting linkage.

2. In randomly distributed crack systems, potential fracture pathways do not arise uniformly throughout the crack population. Instead, they emerge from subsets of cracks with orientation, spacing and relative position that promote the overlap of stress perturbation regions around their tips. This suggests that macroscopic fracture orientation may develop through the linkage of mechanically favorable crack clusters rather than from the homogeneous response of the entire crack population.

3. When the normalized and reduced stress perturbation values recorded for each geometrical configuration are converted to crustal pressure conditions, the depth range over which tensile failure, shear failure and open-crack conditions are possible depends on effective pressure, tensile strength, cohesion, pore fluid pressure and crack aspect ratio. Under hydrostatic pore-pressure conditions, increasing depth progressively restricts the conditions for tensile failure and crack opening, whereas elevated pore fluid pressure expands the depth range over which crack interaction may promote brittle failure. We argue that, under common upper-crustal pressure conditions, only the highest calculated stress perturbations may produce local effective tension. Therefore, the configurations in which compression is most effectively reduced may be the first to reactivate during deformation, leading to crack linkage and, ultimately, to the formation of shear fractures.

Overall, the results show that the orientation, spacing and spatial distribution of pre-existing cracks in a rock undergoing elastic deformation determine whether local stress perturbations promote or inhibit crack linkage. The geometrical arrangement of pre-existing cracks therefore is the dominant factor controlling how fracture networks develop, orient and evolve mechanically in the upper crust.

Appendix A

https://doi.org/10.5194/egusphere-2026-4027
Preprint. Discussion started: 6 August 2026

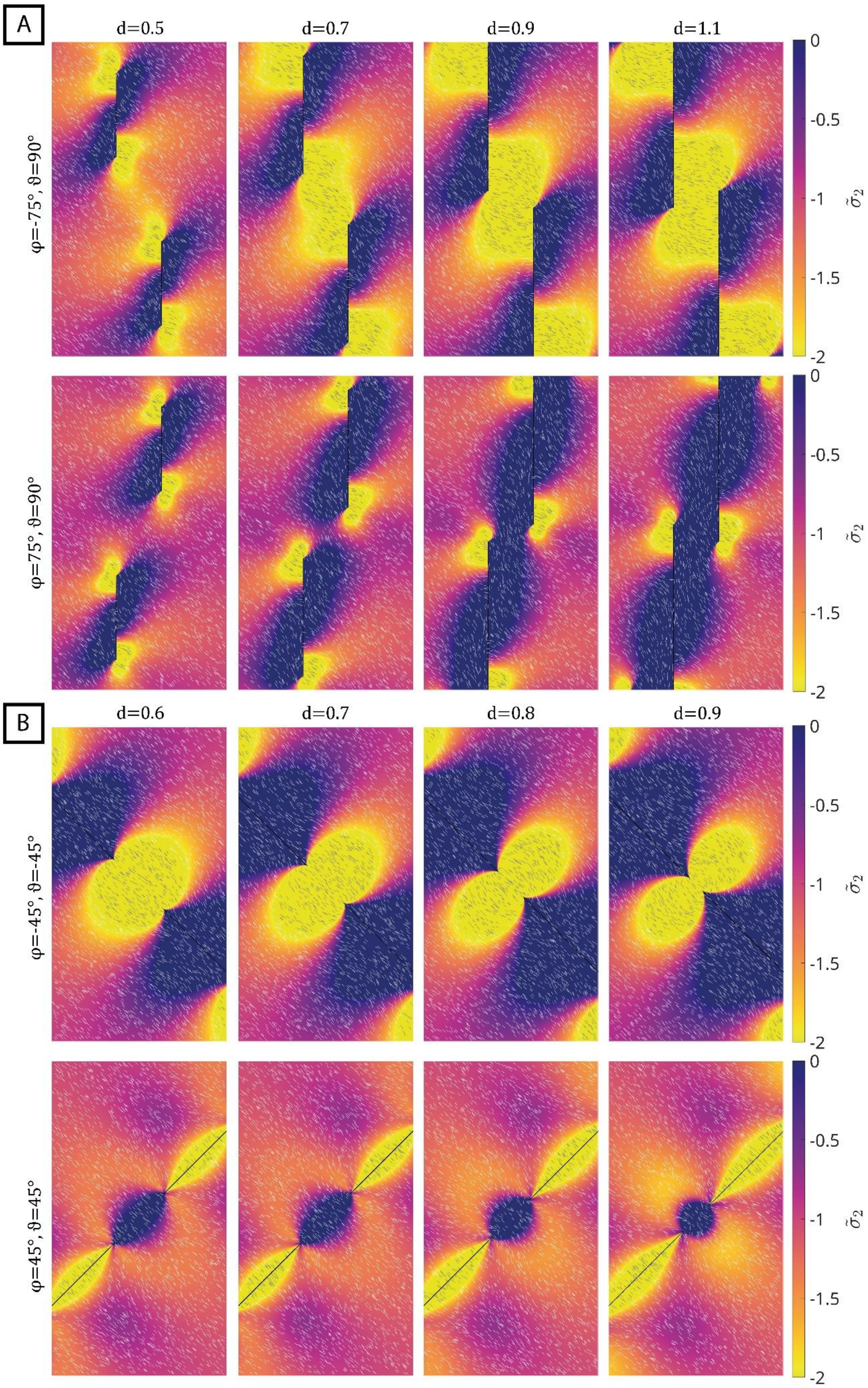

1461

https://doi.org/10.5194/egusphere-2026-4027
Preprint. Discussion started: 6 August 2026

Fig. A1: Magnitude of the minor in-plane principal stress $\tilde{\sigma}_2$ for different geometric configurations of *en echelon* crack arrays. Only the central unit cell is shown. White and black lines indicate the local trajectories of the major in-plane principal stress $\vec{\sigma}_1$. (a) Crack orientation: ϑ=90° (mode II cracks relative to far-field simple shear). In each row, the array orientation φ is fixed: -75° (top) and 75° (bottom). Along each row, d varies from 0.5 to 1.1. B) Crack orientation: ϑ=-45° (top row, mode I cracks relative to far-field simple shear), and ϑ=45° (bottom row). The array orientation φ is -45° (top) and 45° (bottom). Along each row, d varies from 0.6 to 0.9.

https://doi.org/10.5194/egusphere-2026-4027
Preprint. Discussion started: 6 August 2026

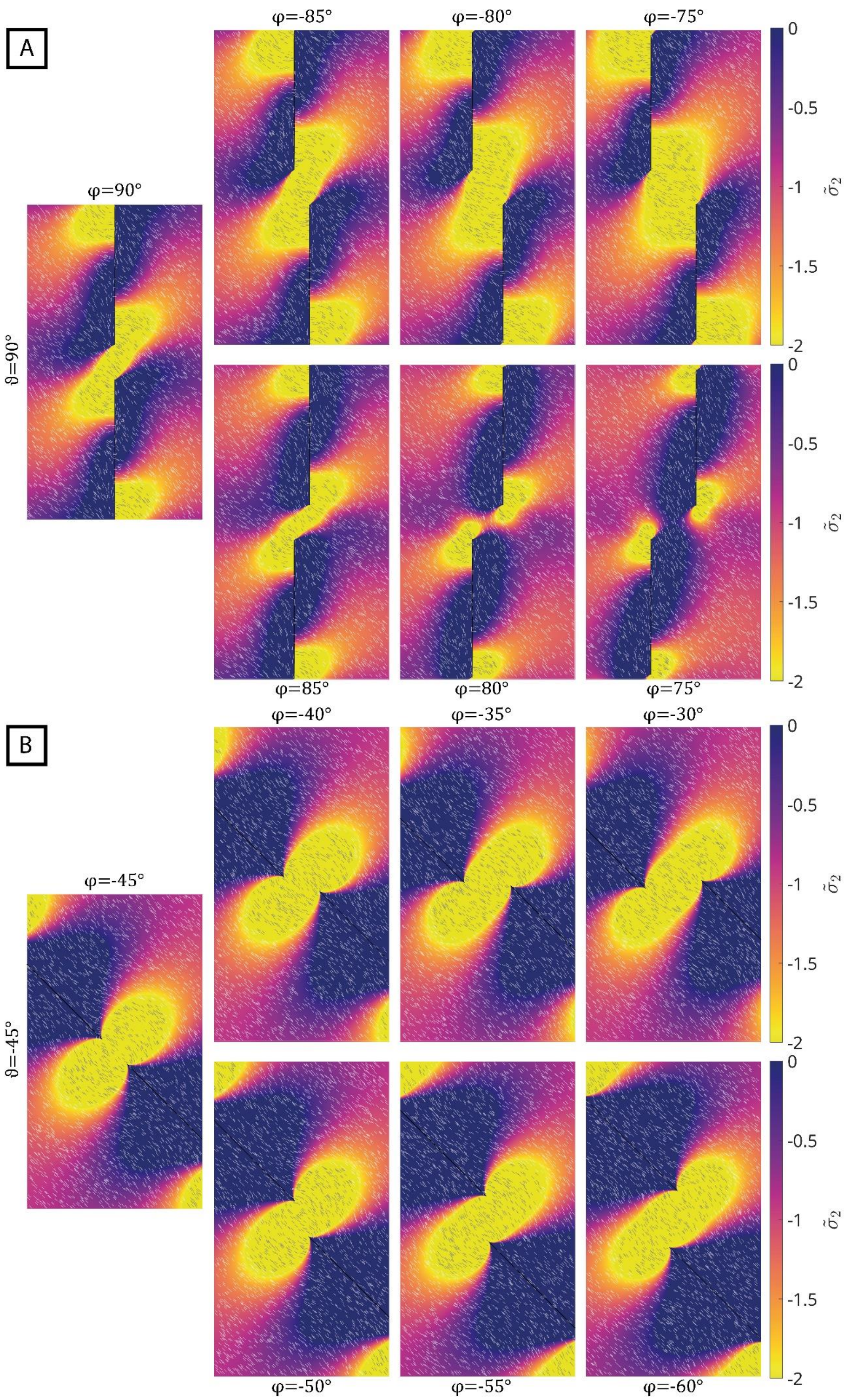

1470

https://doi.org/10.5194/egusphere-2026-4027
Preprint. Discussion started: 6 August 2026

Fig. A2: Normalized and reduced minor principal stress magnitude $\tilde{\sigma}_2$ for different geometric configurations of *en echelon* crack arrays. Only the central unit cell is shown. White and black lines indicate the local trajectories of the major in-plane principal stress $\vec{\sigma}_1$. (a) The crack orientation is fixed at ϑ=90°. The projected overlap is fixed at d=0.8. The crack array orientation φ ranges from -90° to -75° (top row) and from 90° to 75° (bottom row). B) The crack orientation is fixed at ϑ=-45°. The projected overlap is fixed at d=0.8. The crack array orientation φ ranges from -30° to -60°.

https://doi.org/10.5194/egusphere-2026-4027
Preprint. Discussion started: 6 August 2026

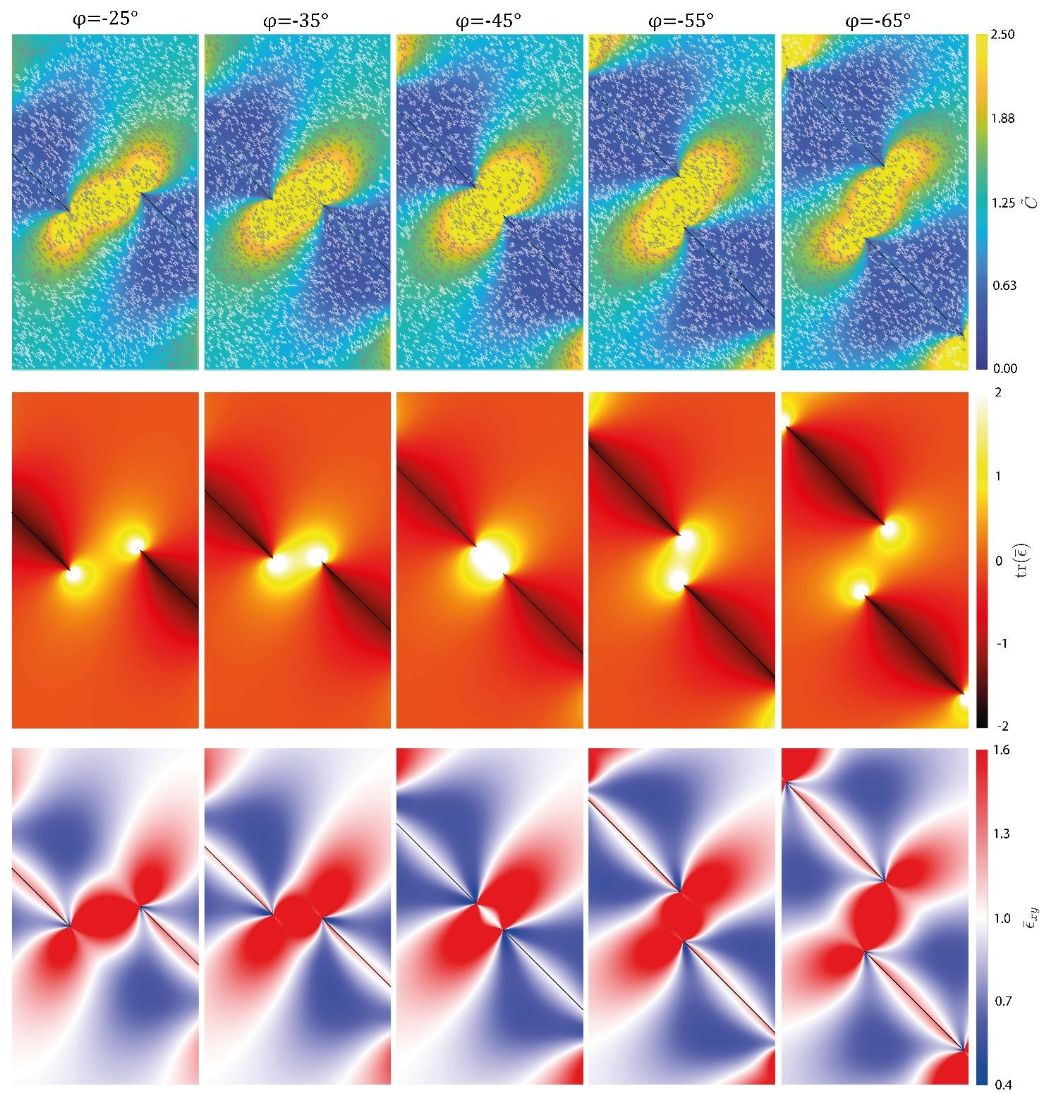

Fig. A3: Normalized effective cohesion $\tilde{C}$, normalized first strain invariant $\bar{I}_1$ and shear strain component $\bar{\varepsilon}_{xy}$ for different geometric configurations of *en echelon* crack arrays. The crack orientation is set at ϑ=-45°, and the projected overlap is fixed at d=0.8. The array orientation φ is varied between -25° and -65°. White and black lines in the first row indicate the potential orientations of conjugate shear fractures.

https://doi.org/10.5194/egusphere-2026-4027
Preprint. Discussion started: 6 August 2026

1484 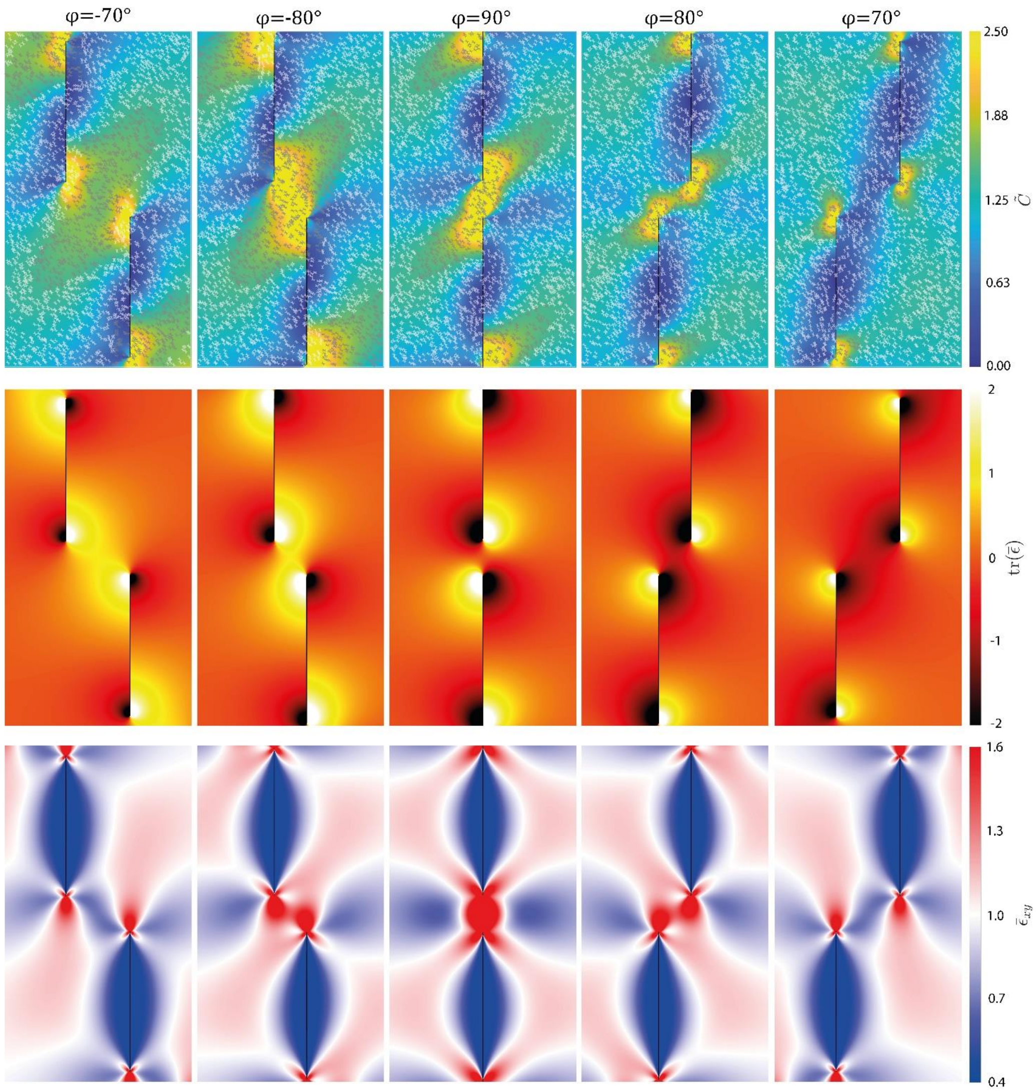

1485 **Fig. A4**: Normalized effective cohesion $\tilde{C}$, normalized first strain invariant $\bar{I}_1$ and shear strain component $\bar{\varepsilon}_{xy}$
1486 for different geometric configurations of *en echelon* crack arrays. The crack orientation is set at ϑ=90°, and
1487 the projected overlap is fixed at d=0.8. The array orientation φ is varied between -70° and -90° and,
1488 symmetrically, between 90° and 70°. White and black lines in the first row indicate the potential orientations
1489 of conjugate shear fractures.

1490

https://doi.org/10.5194/egusphere-2026-4027
Preprint. Discussion started: 6 August 2026

1491 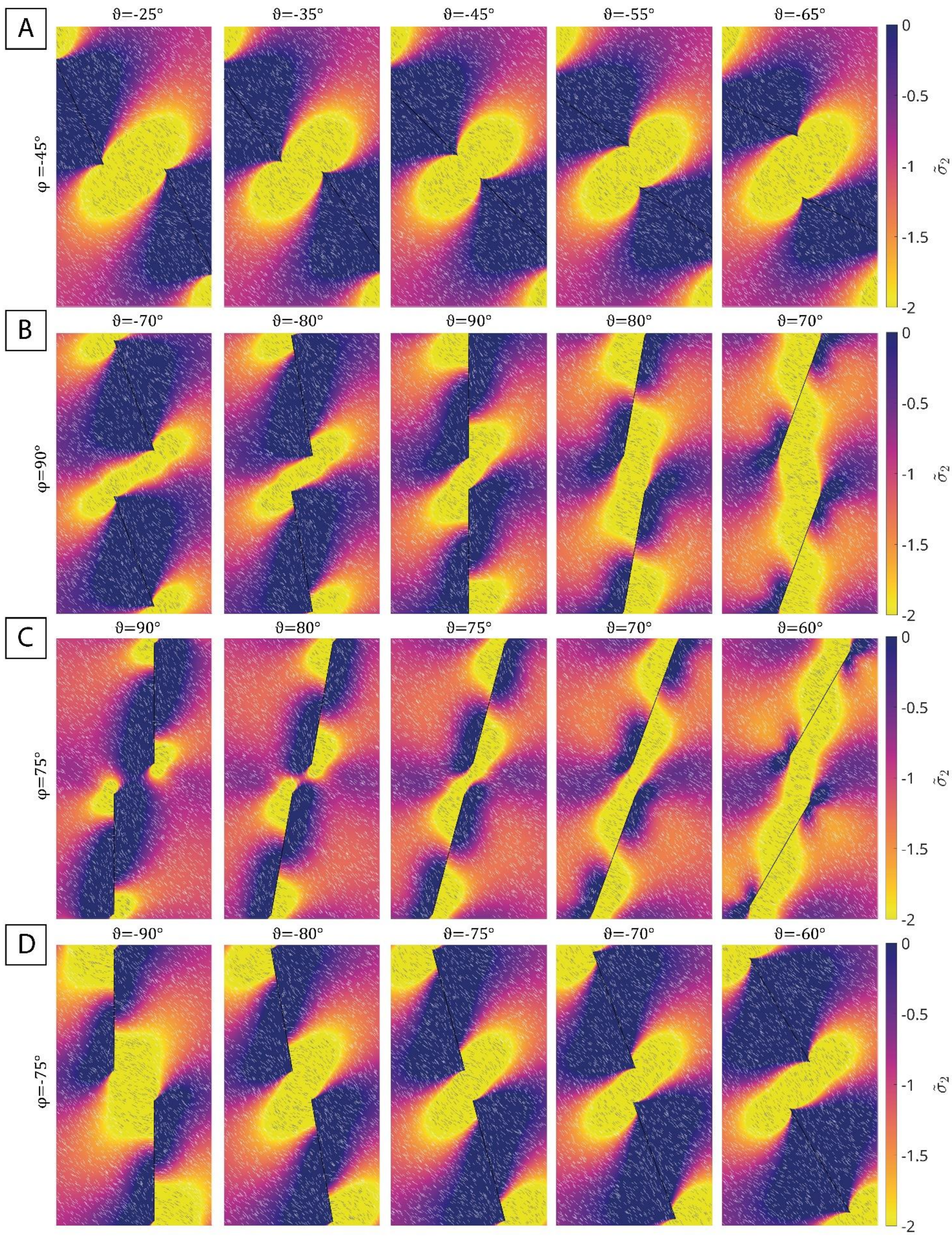

1492 **Fig. A5**: Magnitude of the minor in-plane principal stress $\tilde{\sigma}_2$ for different geometric configurations of *en*
1493 *echelon* crack arrays. The projected overlap is fixed at d=0.8. White and black lines represent the local

https://doi.org/10.5194/egusphere-2026-4027
Preprint. Discussion started: 6 August 2026

trajectories of the major in-plane principal stress $\vec{\sigma}_1$. (a) The crack array orientation is fixed at φ=-45°. The crack orientation ϑ ranges from -25° to -65°. B) The crack array orientation is fixed at φ=90°. The crack orientation ϑ ranges from -70° to -90° and, symmetrically, from 70° to 90°. C) The crack array orientation is fixed at φ=75°. The crack orientation ϑ ranges from 90° to 60°. D) The crack array orientation is fixed at φ=-75°. The crack orientation ϑ ranges from -90° to -60°.

https://doi.org/10.5194/egusphere-2026-4027
Preprint. Discussion started: 6 August 2026

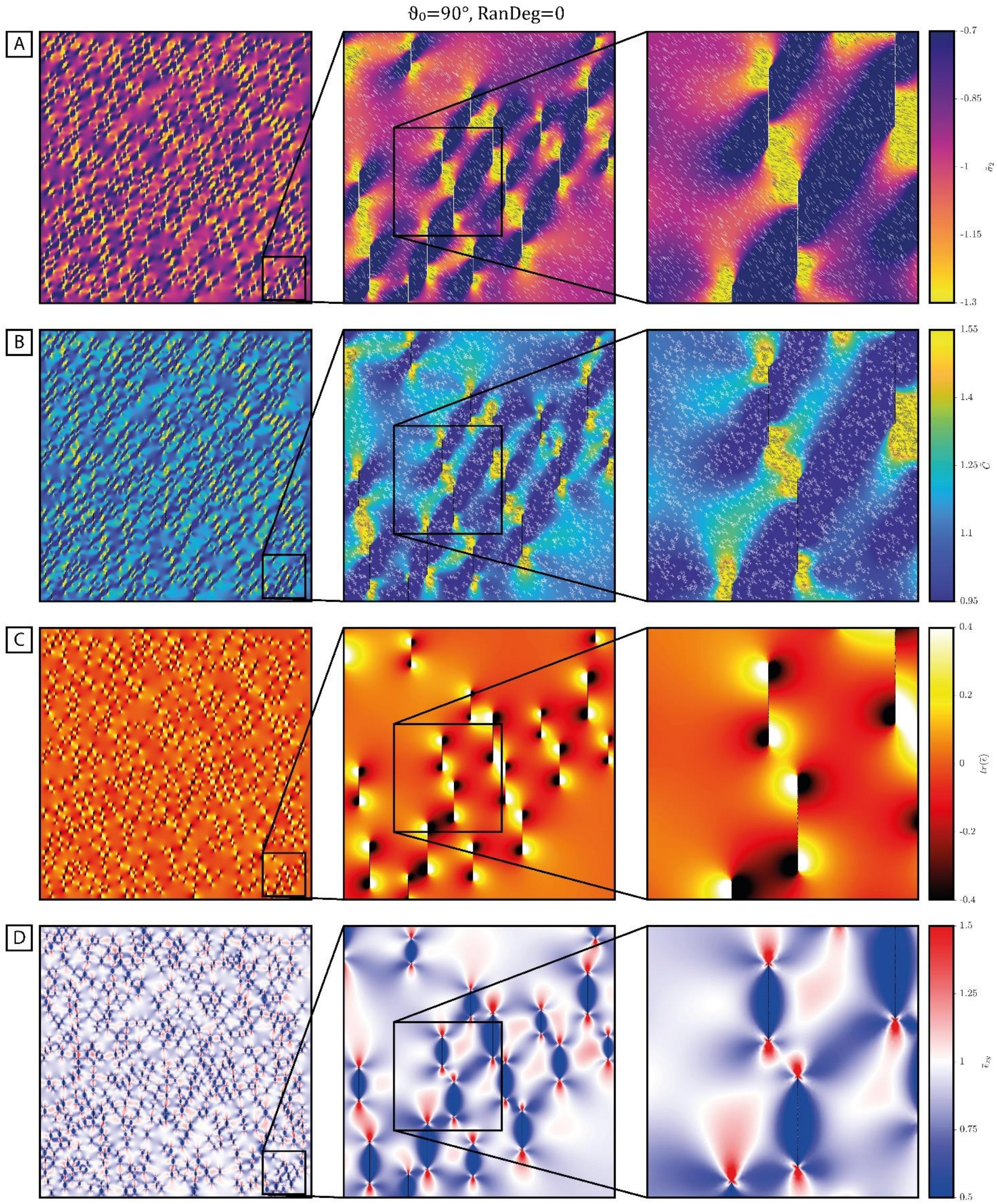

Fig. A6: Stress and strain fields in a system with 500 vertically aligned cracks ($\vartheta_0 = 90°$ and $RanDeg = 0$) with random locations. In the first inset, a subdomain containing multiple *en echelon* arrays of cracks is illustrated. The second inset shows the interactions between the tips of two cracks in an *en echelon* array. (a) Magnitude of the minor in-plane principal stress $\tilde{\sigma}_2$. White and black lines represent the local trajectories

https://doi.org/10.5194/egusphere-2026-4027
Preprint. Discussion started: 6 August 2026

of the major in-plane principal stress $\vec{\sigma}_1$. B) Normalized effective cohesion $\tilde{C}$. White and black lines indicate the potential orientations of conjugate shear fractures. C) Normalized first strain invariant $\bar{I}_1$. D) Normalized shear strain $\bar{\varepsilon}_{xy}$.

https://doi.org/10.5194/egusphere-2026-4027
Preprint. Discussion started: 6 August 2026

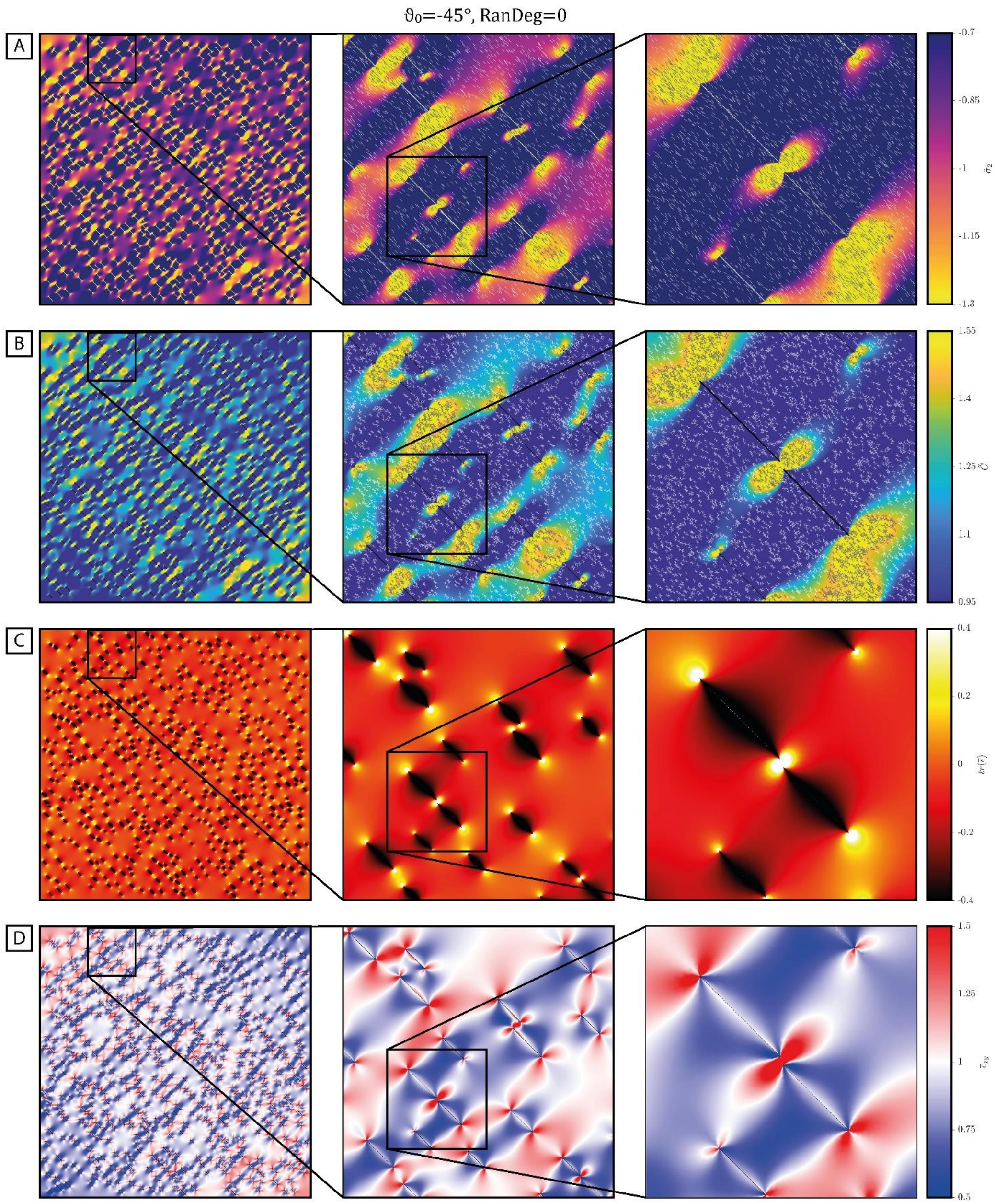

Fig. A7: Stress and strain fields in a system with 500 obliquely aligned cracks ($\vartheta_0 = -45°$ and $RanDeg = 0$) with random locations. In the first inset, a subdomain containing multiple *en echelon* arrays of cracks is illustrated. The second inset shows the interactions between the tips of two interacting cracks in an *en echelon* array. (a) Magnitude of the minor in-plane principal stress $\tilde{\sigma}_2$. White and black lines represent the

https://doi.org/10.5194/egusphere-2026-4027
Preprint. Discussion started: 6 August 2026

local trajectories of the major in-plane principal stress $\vec{\sigma}_1$. B) Normalized effective cohesion $\tilde{C}$. White and black lines indicate the potential orientations of conjugate shear fractures. C) Normalized first strain invariant $\bar{I}_1$. D) Normalized shear strain $\bar{\varepsilon}_{xy}$.

https://doi.org/10.5194/egusphere-2026-4027
Preprint. Discussion started: 6 August 2026

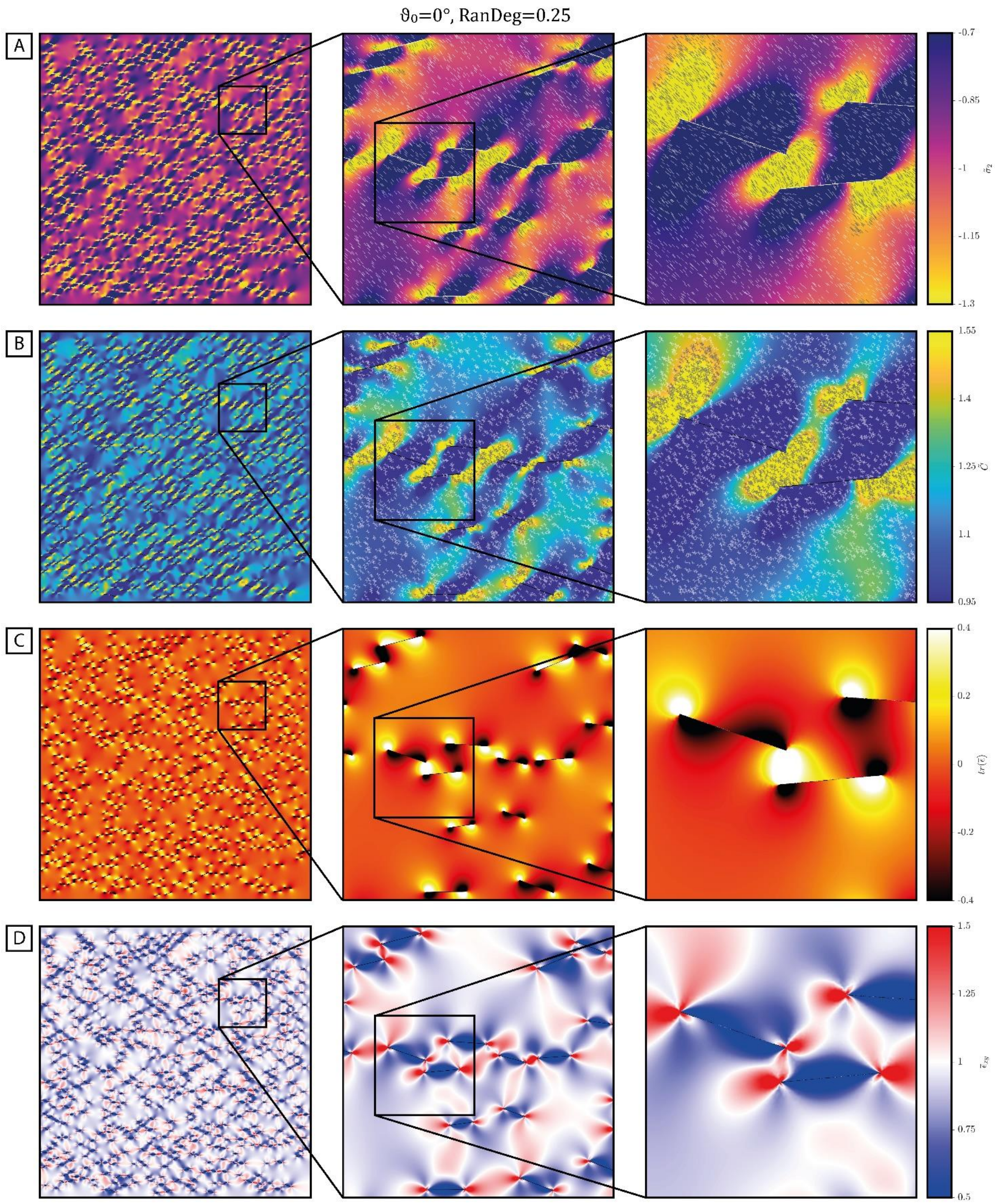

Fig. A8: Stress and strain fields in a system containing 500 cracks with base orientation $\vartheta_0 = 0°$ and $RanDeg = 0.25$ with random locations. In each row, the first inset illustrates a subdomain containing mechanically interacting cracks with different orientations. The second inset shows the interaction between the tips of two cracks. (a) Magnitude of the minor in-plane principal stress $\tilde{\sigma}_2$. White and black lines represent

https://doi.org/10.5194/egusphere-2026-4027
Preprint. Discussion started: 6 August 2026

the local trajectories of the major in-plane principal stress $\vec{\sigma}_1$. B) Normalized effective cohesion $\tilde{C}$. White and black lines indicate the potential orientations of conjugate shear fractures. C) Normalized first strain invariant $\bar{I}_1$. D) Normalized shear strain $\bar{\varepsilon}_{xy}$.

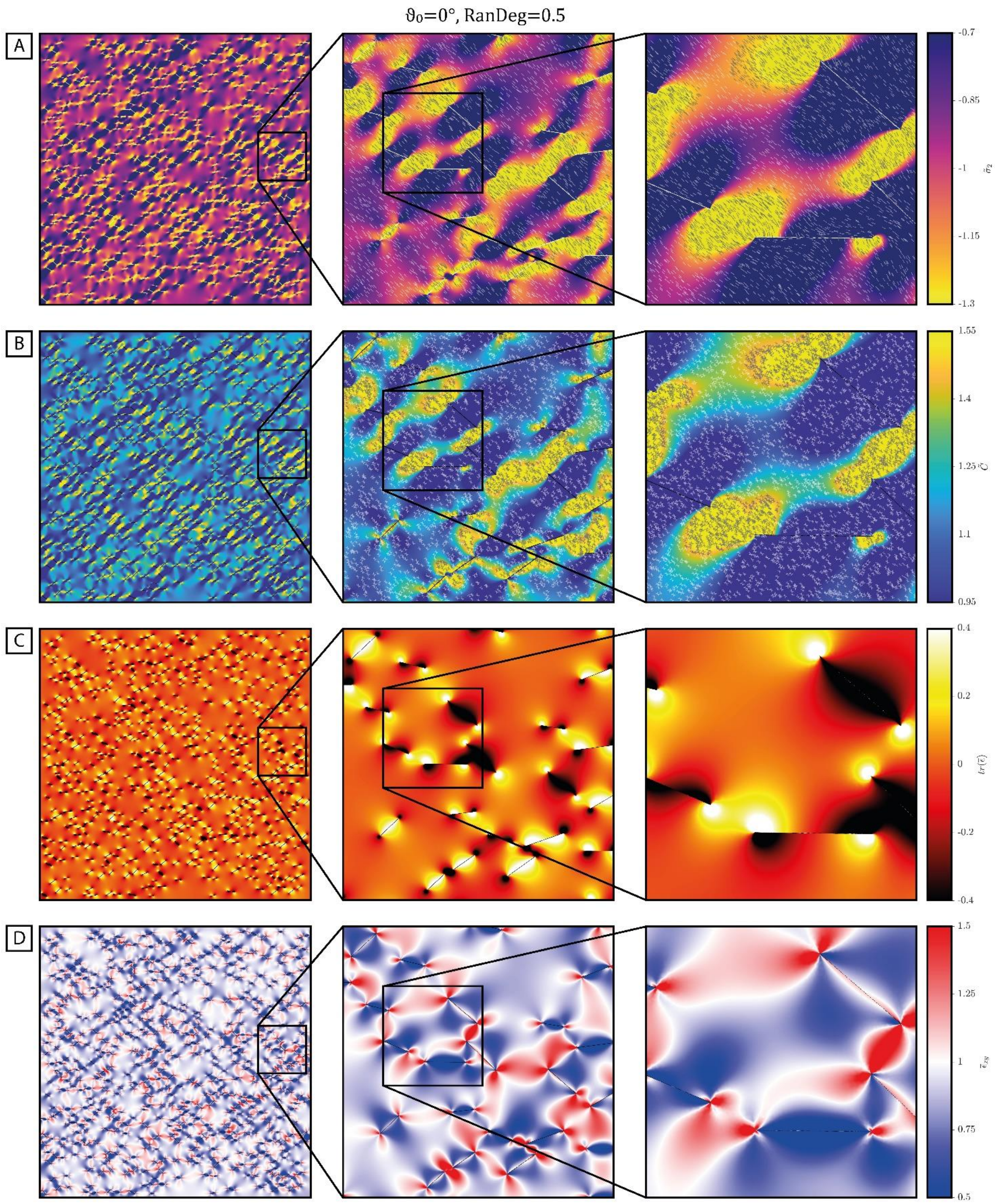

Fig. A9: Stress and strain fields in a system containing 500 cracks with base orientation $\vartheta_0 = 0°$ and $RanDeg = 0.5$ with random locations. In each row, the first inset illustrates a subdomain containing mechanically interacting cracks with different orientations. The second inset shows the interaction between the tips of two cracks. (a) Magnitude of the minor in-plane principal stress $\tilde{\sigma}_2$. White and black lines represent

https://doi.org/10.5194/egusphere-2026-4027
Preprint. Discussion started: 6 August 2026

the local trajectories of the major in-plane principal stress $\vec{\sigma}_1$. B) Normalized effective cohesion $\tilde{C}$. White and black lines indicate the potential orientations of conjugate shear fractures. C) Normalized first strain invariant $\bar{I}_1$. D) Normalized shear strain $\bar{\varepsilon}_{xy}$.

Data availability

The numerical results presented in this study are generated from the finite element model code and input parameters described in the manuscript. The full set of raw output files is not deposited in a public repository because the study involves a large parametric exploration of hundreds of geometric configurations, each producing separate numerical output files, and the complete dataset would be large and largely redundant with the reproducible model outputs. The data underlying the figures can be regenerated using the publicly available code provided in the Code availability section. Additional processed output files are available from the corresponding author upon reasonable request.

Code availability

To improve the reproducibility of this experiment, the codes used for FEM analysis are available at a Zenodo (Manna, 2025; retrievable at https://doi.org/10.5281/zenodo.15681017) and GitHub repository (https://github.com/LudoManna/CrackSystems.git).

Author contribution

LM conceived the work, developed numerical models, analyzed and interpreted the data. MM conceived the work and interpreted the data. LC developed numerical models. MD conceived the work, developed numerical models, and interpreted the data.

https://doi.org/10.5194/egusphere-2026-4027
Preprint. Discussion started: 6 August 2026

Competing interests

The authors declare that they have no conflict of interest.

Acknowledgements

We would like to express our gratitude to Prof. Alessandro Reali and Prof. David Peacock for the precious help and comments to the manuscript, and for providing us with interesting and useful suggestions. The authors used ChatGPT for language editing and stylistic suggestions during the preparation of the manuscript. All scientific content, interpretations, and wording were made by the authors.

Financial support

This research was supported in the frame of the Italian 1:50.000 Geological Mapping project - CARG Foglio 229 - Savona and Foglio 244 - Ormea (ISPRA, Regione Liguria, University of Pavia and Genova).

References

Amitrano, D.: Brittle-ductile transition and associated seismicity: Experimental and numerical studies and relationship with the b value, J. Geophys. Res.-Solid Earth, 108, https://doi.org/10.1029/2001JB000680, 2003.

Anders, M. H., Laubach, S. E., and Scholz, C. H.: Microfractures: A review, J. Struct. Geol., 69, 377–394, https://doi.org/10.1016/j.jsg.2014.05.011, 2014.

Anderson, E. M.: The dynamics of faulting, Trans. Edinb. Geol. Soc., 8, 387–402, https://doi.org/10.1144/transed.8.3.387, 1905.

https://doi.org/10.5194/egusphere-2026-4027
Preprint. Discussion started: 6 August 2026

Ashby, M. F. A., and Hallam, S. D.: The failure of brittle solids containing small cracks under compressive stress states, Acta Metall., 34, 497–510, https://doi.org/10.1016/0001-6160(86)90086-6, 1986.

Ashby, M. F., and Sammis, C. G.: The damage mechanics of brittle solids in compression, Pure Appl. Geophys., 133, 489–521, https://doi.org/10.1007/BF00878002, 1990.

Atkinson, B. K.: Subcritical crack propagation in rocks: theory, experimental results and applications, J. Struct. Geol., 4, 41–56, https://doi.org/10.1016/0191-8141(82)90005-0, 1982.

Atkinson, B. K. (Ed.): Fracture mechanics of rock. Elsevier, Elsevier, ISBN: 9780123822383, 2015.

Aydin, A., and Schultz, R. A.: Effect of mechanical interaction on the development of strike-slip faults with echelon patterns, J. Struct. Geol., 12, 123–129, https://doi.org/10.1016/0191-8141(90)90053-2, 1990.

Aydin, A., Borja, R. I., and Eichhubl, P.: Geological and mathematical framework for failure modes in granular rock, J. Struct. Geol., 28, 83–98, https://doi.org/10.1016/j.jsg.2005.07.008, 2006.

Bahat, D.: Tectonofractography, in: Tectonofractography 239–324 Berlin, Heidelberg: Springer Berlin Heidelberg, https://doi.org/10.1007/978-3-642-76162-1, 1991.

Bahat, D., Rabinovitch, A., and Frid, V.: Tensile fracturing in rocks: tectonofractographic and electromagnetic radiation methods, Berlin, Heidelberg: Springer Berlin Heidelberg, https://doi.org/10.1007/b137741 2005.

Bathe, K. J.: Finite element procedures, Klaus-Jurgen Bathe, ISBN: 978-0-9790049-5-7 2006.

Beach, A.: The geometry of en-echelon vein arrays, Tectonophysics, 28, 245–263, https://doi.org/10.1016/0040-1951(75)90040-2, 1975.

Bertoldi, K., Bigoni, D., and Drugan, W. J.: A discrete-fibers model for bridged cracks and reinforced elliptical voids, J. Mech. Phys. Solids, 55, 1016–1035, https://doi.org/10.1016/j.jmps.2006.10.007, 2007.

https://doi.org/10.5194/egusphere-2026-4027
Preprint. Discussion started: 6 August 2026

Biddle, K. I., and Christie-Blick, N. H.: Basin Formation, Structural Traps, and Controls on Hydrocarbon Occurrence Along Wrench-Fault Zones, in: Offshore Technology Conference OTC-4872 OTC, https://doi.org/10.4043/4872-MS, 1985.

Bobet, A., and Einstein, H. H.: Fracture coalescence in rock-type materials under uniaxial and biaxial compression, Int. J. Rock Mech. Min. Sci., 35, 863–888, https://doi.org/10.1016/S0148-9062(98)00005-9, 1998.

Bons, P. D., Elburg, M. A., and Gomez-Rivas, E.: A review of the formation of tectonic veins and their microstructures, J. Struct. Geol., 43, 33–62, https://doi.org/10.1016/j.jsg.2012.07.005, 2012.

Brace, W. F., and Bombolakis, E. G.: A note on brittle crack growth in compression, J. Geophys. Res., 68, 3709–3713, https://doi.org/10.1029/JZ068i012p03709, 1963.

Brace, W. F., Paulding Jr., B. W., and Scholz, C. H.: Dilatancy in the fracture of crystalline rocks, Journal of geophysical research, 71, 3939–3953, https://doi.org/10.1029/JZ071i016p03939, 1966.

Brace, W., Walsh, J. B., and Frangos, W. T.: Permeability of granite under high pressure, J. Geophys. Res., 73, 2225–2236, https://doi.org/10.1029/JB073i006p02225, 1968.

Brantut, N., Heap, M. J., Meredith, P. G., and Baud, P.: Time-dependent cracking and brittle creep in crustal rocks: A review, J. Struct. Geol., 52, 17–43, https://doi.org/10.1016/j.jsg.2013.03.007, 2013.

Bürgmann, R., Pollard, D. D., and Martel, S. J.: Slip distributions on faults: effects of stress gradients, inelastic deformation, heterogeneous host-rock stiffness, and fault interaction, J. Struct. Geol., 16, 1675–1690, https://doi.org/10.1016/0191-8141(94)90134-1,1994.

Caine, J. S., Evans, J. P., and Forster, C. B.: Fault zone architecture and permeability structure, Geology, 24, 1025–1028, https://doi.org/10.1130/0091-7613(1996)024%3C1025:FZAAPS%3E2.3.CO;2, 1996.

Cannon, N. P., Schulson, E. M., Smith, T. R., and Frost, H. J.: Wing cracks and brittle compressive fracture, Acta Metall. Mater., 38, 1955–1962, https://doi.org/10.1016/0956-7151(90)90307-3, 1990.

https://doi.org/10.5194/egusphere-2026-4027
Preprint. Discussion started: 6 August 2026

Carlson, J. M., Langer, J. S., and Shaw, B. E.: Dynamics of earthquake faults, Rev. Mod. Phys., 66, 657, https://doi.org/10.1103/RevModPhys.66.657, 1994.

Casini, L., Maino, M., Manna, L., and Funedda, A.: MYflow-A simple computer program for rheological modelling of mylonites, J. Struct. Geol., 177, 105006, https://doi.org/10.1016/j.jsg.2023.105006, 2023.

Castelletto, N., Hajibeygi, H., and Tchelepi, H. A.: Multiscale finite-element method for linear elastic geomechanics, J. Comput. Phys., 331, 337–356, https://doi.org/10.1016/j.jcp.2016.11.044, 2017.

Chang, X., Shan, Y., Zhang, Z., Tang, C., and Ru, Z.: Behavior of propagating fracture at bedding interface in layered rocks, Eng. Geol., 197, 33–41, https://doi.org/10.1016/j.enggeo.2015.08.010, 2015.

Chau, K. T., and Wang, G. S.: Condition for the onset of bifurcation in en echelon crack arrays, Int. J. Numer. Anal. Methods Geomech., 25, 289–306, https://doi.org/10.1002/nag.130, 2001.

Chen, J., Wang, W., and Chen, L.: A strain hardening and softening constitutive model for hard brittle rocks, Appl. Sci., 13, 2764, https://doi.org/10.3390/app13052764, 2023.

Chen, Z.: Finite element modelling of viscosity-dominated hydraulic fractures, J. Pet. Sci. Eng., 88, 136–144, https://doi.org/10.1016/j.petrol.2011.12.021, 2012.

Chester, F. M., and Logan, J. M.: Implications for mechanical properties of brittle faults from observations of the Punchbowl fault zone, California, Pure Appl. Geophys., 124, 79–106, https://doi.org/10.1007/BF00875720, 1986.

Childs, C., Manzocchi, T., Walsh, J. J., Bonson, C. G., Nicol, A., and Schöpfer, M. P.: A geometric model of fault zone and fault rock thickness variations, J. Struct. Geol., 31, 117–127, https://doi.org/10.1016/j.jsg.2008.08.009, 2009.

Chinnery, M. A.: The stress changes that accompany strike-slip faulting, Bull. Seismol. Soc. Am., 53, 921–932, https://doi.org/10.1785/BSSA0530050921, 1963.

https://doi.org/10.5194/egusphere-2026-4027
Preprint. Discussion started: 6 August 2026

Christie-Blick, N. and Biddle, K. T.: Deformation and basin formation along strike-slip faults, in: Strike-Slip Deformation, Basin Formation, and Sedimentation, edited by: Biddle, K. T. and Christie-Blick, N., SEPM Spec. Publ., 37, 1–34, https://doi.org/10.2110/pec.85.37.0001, 1985.

Cook, T. S., and Erdogan, F.: Stresses in bonded materials with a crack perpendicular to the interface, International Journal of Engineering Science, 10, 677–697, https://doi.org/10.1016/0020-7225(72)90063-8, 1972.

Cosgrove, J. W., and Engelder, T. (Eds.): The initiation, propagation, and arrest of joints and other fractures. Geological Society of London, https://doi.org/10.1017/S0016756805231709, 2004.

Cox, S. J. D., and Scholz, C. H.: On the formation and growth of faults: an experimental study, J. Struct. Geol., 10, 413–430, https://doi.org/10.1016/0191-8141(88)90019-3, 1988.

Crider, J. G.: The initiation of brittle faults in crystalline rock, J. Struct. Geol., 77, 159–174, https://doi.org/10.1016/j.jsg.2015.05.001, 2015.

Crider, J. G., and Peacock, D. C.: Initiation of brittle faults in the upper crust: a review of field observations, J. Struct. Geol., 26, 691–707, https://doi.org/10.1016/j.jsg.2003.07.007, 2004.

Cunningham, W. D. and Mann, P.: Tectonics of strike-slip restraining and releasing bends, Geol. Soc. London Spec. Publ., 290, 1–12, https://doi.org/10.1144/SP290.1, 2007.

Dabrowski, M., Krotkiewski, M., and Schmid, D. W.: MILAMIN: MATLAB-based finite element method solver for large problems, Geochemistry, Geophysics, Geosystems, 9(4), https://doi.org/10.1029/2007GC001719, 2008.

Dasgupta, S., and Mukherjee, S.: Brittle shear tectonics in a narrow continental rift: Asymmetric nonvolcanic Barmer Basin (Rajasthan, India), J. Geol., 125, 561–591, https://www.jstor.org/stable/26547022, 2017.

De Joussineau, G., and Aydin, A.: The evolution of the damage zone with fault growth in sandstone and its multiscale characteristics, J. Geophys. Res.-Solid Earth, 112, https://doi.org/10.1029/2006JB004711, 2007.

https://doi.org/10.5194/egusphere-2026-4027
Preprint. Discussion started: 6 August 2026

Du, Y., and Aydin, A.: Interaction of multiple cracks and formation of echelon crack arrays, Int. J. Numer. Anal. Methods Geomech., 15, 205–218, https://doi.org/10.1002/nag.1610150305, 1991.

Erdogan, F. and Sih, G. C.: On the crack extension in plates under plane loading and transverse shear, J. Basic Eng., 85, 519–527, https://doi.org/10.1115/1.3656897, 1963.

Evans, A. G.: The strength of brittle materials containing second phase dispersions, Philos. Mag., 26, 1327–1344, https://doi.org/10.1080/14786437208220346, 1972.

Fattaruso, L., Cooke, M., and McBeck, J.: The influence of fracture growth and coalescence on the energy budget leading to failure, Front. Earth Sci., 10, 853030, https://doi.org/10.3389/feart.2022.853030, 2022.

Faulkner, D. R., Jackson, C. A. L., Lunn, R. J., Schlische, R. W., Shipton, Z. K., Wibberley, C. A. J., and Withjack, M. O.: A review of recent developments concerning the structure, mechanics and fluid flow properties of fault zones, J. Struct. Geol., 32, 1557–1575, https://doi.org/10.1016/j.jsg.2010.06.009, 2010.

Feng, X. Q., and Gross, D.: On the coalescence of collinear cracks in quasi-brittle materials, Eng. Fract. Mech., 65, 511–524, https://doi.org/10.1016/S0013-7944(99)00139-3, 2000.

Feves, M., and Simmons, G.: Effects of stress on cracks in Westerly granite, Bull. Seismol. Soc. Am., 66, 1755–1765, https://doi.org/10.1785/BSSA0660051755, 1976.

Fossen, H.: Structural Geology, Cambridge University Press, ISBN: 1107057647, 9781107057647, 2016.

Goodier, J. N., and Hodge Jr., P. G.: Elasticity and plasticity: The mathematical theory of elasticity and the mathematical theory of plasticity, courier dover publications, ISBN: 9780486806044, 2016.

Gottschalk, R. R., Kronenberg, A. K., Russell, J. E., and Handin, J.: Mechanical anisotropy of gneiss: failure criterion and textural sources of directional behavior, J. Geophys. Res.-Solid Earth, 95, 21613–21634, https://doi.org/10.1029/JB095iB13p21613, 1990.

https://doi.org/10.5194/egusphere-2026-4027
Preprint. Discussion started: 6 August 2026

Graham, C. C., Stanchits, S., Main, I. G., and Dresen, G.: Comparison of polarity and moment tensor inversion methods for source analysis of acoustic emission data, Int. J. Rock Mech. Min. Sci., 47, 161–169, https://doi.org/10.1016/j.ijrmms.2009.05.002, 2010.

Granier, T.: Origin, damping, and pattern of development of faults in granite, Tectonics, 4, 721–737, https://doi.org/10.1029/TC004i007p00721, 1985.

Griffith, A. A.: The theory of rupture, in: International Congress for Applied Mechanics, https://hal.science/hal-04771599v1, 1924.

Griffith, A. A.: The phenomena of rupture and flow in solids, Philos. T. R. Soc. A, 221, 163–198, https://doi.org/10.1098/rsta.1921.0006 1920.

Gudmundsson, A.: Deflection of dykes into sills at discontinuities and magma-chamber formation, Tectonophysics, 500, 50–64, https://doi.org/10.1016/j.tecto.2009.10.015, 2011.

Gudmundsson, A., Berg, S. S., Lyslo, K. B., and Skurtveit, E.: Fracture networks and fluid transport in active fault zones, J. Struct. Geol., 23, 343–353, https://doi.org/10.1016/S0191-8141(00)00100-0, 2001.

Hallbauer, D. K., Wagner, H. N. G. W., and Cook, N. G. W.: Some observations concerning the microscopic and mechanical behaviour of quartzite specimens in stiff, triaxial compression tests, in: International Journal of Rock Mechanics and Mining Sciences & Geomechanics Abstracts (vol. 10, no. 6, 713–726 Pergamon, https://doi.org/10.1016/0148-9062(73)90015-6, 1973.

Handy, M. R., Hirth, G., and Bürgmann, R.: Continental fault structure and rheology from the frictional-to-viscous transition downward, in: Tectonic Faults: Agents of Change on a Dynamic Earth, edited by: Handy, M. R., Hirth, G., and Hovius, N., MIT Press, Cambridge, Massachusetts, USA, 139–181, https://doi.org/10.7551/mitpress/6703.003.0008, 2007.

Harris, R. A.: Large earthquakes and creeping faults, Rev. Geophys., 55, 169–198, https://doi.org/10.1002/2016RG000539, 2017.

Healy, D., Jones, R. R., and Holdsworth, R. E.: Three-dimensional brittle shear fracturing by tensile crack interaction, Nature, 439, 64–67, https://doi.org/10.1038/nature04346, 2006.

Hickman, S., Sibson, R., and Bruhn, R.: Introduction to special section: Mechanical involvement of fluids in faulting, J. Geophys. Res.-Solid Earth, 100, 12831–12840, https://doi.org/10.1029/95JB01121, 1995.

Hoek, E., and Bieniawski, Z. T.: Brittle fracture propagation in rock under compression, Int. J. Fract. Mech., 1, 137–155, https://doi.org/10.1007/bf00186851, 1965.

Hooper, E. C. D.: Fluid migration along growth faults in compacting sediments, J. Pet. Geol., 14, 161–180, https://doi.org/10.1111/j.1747-5457.1991.tb00360.x, 1991.

Horii, H., and Nemat-Nasser, S.: Compression-induced microcrack growth in brittle solids: Axial splitting and shear failure, J. Geophys. Res.-Solid Earth, 90, 3105–3125, https://doi.org/10.1029/JB090iB04p03105, 1985.

Hughes, T. J.: The finite element method: linear static and dynamic finite element analysis, Courier Corporation, ISBN: 0486135020, 9780486135021, 2003.

Irwin, G. R.: Analysis of stresses and strains near the end of a crack traversing a plate, Journal of applied mechanics, 24, 361–364, https://doi.org/10.1115/1.4011547, 1957.

Irwin, G. R., and de Wit, R.: A summary of fracture mechanics concepts, J. Test. Eval., 11, 56–65, https://doi.org/10.1115/1.4011547, 1983.

Jackson, R. R.: Vein arrays and their relationship to transpression during fold development in the Culm Basin, central south-west England, Proc. Ussher Soc., 7, 356–362, 1991.

Jaeger, J. C., Cook, N. G., and Zimmerman, R.: Fundamentals of rock mechanics, John Wiley & Sons, https://doi.org/10.1017/CBO9780511735349, 2009.

Johnson, K. L.: Contact mechanics, Cambridge university press, ISBN: 0 521 34796 3 1987.

https://doi.org/10.5194/egusphere-2026-4027
Preprint. Discussion started: 6 August 2026

Kachanov, M.: Effective elastic properties of cracked solids: critical review of some basic concepts, Appl. Mech. Rev., 45, 304–335, https://doi.org/10.1115/1.3119761, 1992.

Kanaya, T., and Hirth, G.: Role of crack interaction on shear localization in porous granular rocks deformed in the brittle and ductile fields, J. Geophys. Res.-Solid Earth, 129, e2023JB027316, https://doi.org/10.1029/2023JB027316, 2024.

Kelly, P. G., Sanderson, D. J., and Peacock, D. C. P.: Linkage and evolution of conjugate strike-slip fault zones in limestones of Somerset and Northumbria, J. Struct. Geol., 20, 1477–1493, https://doi.org/10.1016/S0191-8141(98)00049-6, 1998.

Kim, Y. S., and Sanderson, D. J.: The relationship between displacement and length of faults: a review, Earth-Science Reviews, 68, 317–334, https://doi.org/10.1016/j.earscirev.2004.06.003, 2005.

Kim, Y. S., Peacock, D. C. P., and Sanderson, D. J.: Mesoscale strike-slip faults and damage zones at Marsalforn, Gozo Island, Malta, J. Struct. Geol., 25, 793–812, http://dx.doi.org/10.1016/S0191-8141(02)00200-6, 2003.

Kim, Y. S., Peacock, D. C., and Sanderson, D. J.: Fault damage zones, J. Struct. Geol., 26, 503–517, http://dx.doi.org/10.1016/j.jsg.2003.08.002, 2004.

Kranz, R. L.: Crack growth and development during creep of Barre granite, in: International Journal of Rock Mechanics and Mining Sciences & Geomechanics Abstracts (vol. 16, no. 1, 23–35 Pergamon, https://doi.org/10.1016/0148-9062(79)91441-2, 1979.

Kranz, R. L.: Microcracks in rocks: a review, Tectonophysics, 100, 449–480, https://doi.org/10.1016/0040-1951(83)90198-1, 1983.

Kristensen, M. B., Childs, C. J., and Korstgård, J. A.: The 3D geometry of small-scale relay zones between normal faults in soft sediments, J. Struct. Geol., 30, 257–272, https://doi.org/10.1016/j.jsg.2007.11.009, 2008.

https://doi.org/10.5194/egusphere-2026-4027
Preprint. Discussion started: 6 August 2026

La Pointe, P. R. and Hudson, J. A.: Characterization and interpretation of rock mass joint patterns, Geol. Soc. Am. Spec. Pap., 199, 37 pp., https://doi.org/10.1130/SPE199-P1, 1985.

Lawn, B.: Fracture of Brittle Solids 2nd ed, Cambridge University Press, Cambridge, https://doi.org/10.1017/CBO9780511623127, 1993.

Lee, H. P., Schultz, R. A., and Olson, J. E.: Inferring friction and stress states from the angle between wing fractures and solution surfaces, J. Struct. Geol., 162, 104706, https://doi.org/10.1016/j.jsg.2022.104706, 2022.

Li, Q., Liu, M., and Zhang, H.: A 3-D viscoelastoplastic model for simulating long-term slip on non-planar faults, Geophys. J. Int., 176, 293–306, https://doi.org/10.1111/j.1365-246X.2008.03962.x, 2009.

Liebowitz, H., Harris, D. W., and Vanderveldt, H.: Fracture of long and short notched columns: Tests were performed on notched and unnotched columns of various lengths, Different failure criteria were examined. Experimental Mechanics, 8, 49–55, https://doi.org/10.1007/BF02326126, 1968.

Lisle, R. J.: Geological strain analysis: A manual for the Rf/ø method, Elsevier, ISBN: 0080325904, 9780080325903, 2013.

Liu, H. W.: Shear fatigue crack growth: a literature survey, Fatigue Fract. Eng. M., 8, 295–313, https://doi.org/10.1111/j.1460-2695.1985.tb00429.x, 1985.

Liu, S., Lan, H., and Martin, C. D.: Progressive transition from extension fracture to shear fracture of altered granite during uniaxial tensile tests, Rock Mech. Rock Eng., 55, 5355–5375, https://doi.org/10.1007/s00603-022-02897-6, 2022.

Lockner, D., Byerlee, J. D., Kuksenko, V., Ponomarev, A., and Sidorin, A.: Quasi-static fault growth and shear fracture energy in granite, Nature, 350, 39–42, https://doi.org/10.1038/350039a0, 1991.

Maino, M., Casini, L., Boschi, C., Di Giulio, A., Setti, M., and Seno, S.: Time-dependent heat budget of a thrust from geological records and numerical experiments, J. Geophys. Res.-Solid Earth, 125, e2019JB018940, https://doi.org/10.1029/2019JB018940, 2020.

https://doi.org/10.5194/egusphere-2026-4027
Preprint. Discussion started: 6 August 2026

Mandal, N.: Mode of development of sigmoidal en echelon fractures, Proc. Indian Acad. Sci.-Earth Planet. Sci., 104, 453–464, https://doi.org/10.1007/BF02843409, 1995.

Mann, P.: Global catalogue, classification and tectonic origins of restraining- and releasing bends on active and ancient strike-slip fault systems, Geol. Soc. London Spec. Publ., 290, 13–142, https://doi.org/10.1144/SP290.2, 2007.

Mann, P., Hempton, M. R., Bradley, D. C., and Burke, K.: Development of pull-apart basins, J. Geol., 91, 529–554, https://doi.org/10.1086/628803, 1983.

Manna, L., Perozzo, M., Menegoni, N., Tamburelli, S., Crispini, L., Federico, L., ... and Maino, M.: Anatomy of a km-scale fault zone controlling the Oligo-Miocene bending of the Ligurian Alps (NW Italy): integration of field and 3D high-resolution digital outcrop model data, Swiss J. Geosci., 116, 15, https://doi.org/10.1186/s00015-023-00444-1, 2023.

Manna, L.: CrackSystems, Zenodo [code], https://doi.org/10.5281/zenodo.15681018, 2025.

Martel, S. J., Pollard, D. D., and Segall, P.: Development of simple strike-slip fault zones, Mount Abbot quadrangle, Sierra Nevada, California, Geol. Soc. Am. Bull., 100, 1451–1465, https://doi.org/10.1130/0016-7606(1988)100<1451:DOSSSF>2.3.CO;2, 1988.

Maugis, D.: Stresses and displacements around cracks and elliptical cavities: exact solutions, Engineering fracture mechanics, 43, 217–255, https://doi.org/10.1016/0013-7944(92)90126-5, 1992.

McBeck, J. A., Zhu, W., and Renard, F.: The competition between fracture nucleation, propagation, and coalescence in dry and water-saturated crystalline rock, Solid Earth, 12, 375–387, https://doi.org/10.5194/se-12-375-2021, 2021.

McBeck, J., Cordonnier, B., Cooke, M., Fattaruso, L., and Renard, F.: Deformation evolves from shear to extensile in rocks due to energy optimization, Commun. Earth Environ., 4, 352, https://doi.org/10.1038/s43247-023-01023-w, 2023.

McBeck, J., Cordonnier, B., Zhu, W., and Renard, F.: Transition from fracture propagation to coalescence in Westerly granite during the preparation process of macroscopic failure, J. Geophys. Res.-Solid Earth, 131, https://doi.org/10.1029/2025JB032676, 2026.

Meguid, S. A., Gaultier, P. E., and Gong, S. X.: A comparison between analytical and finite element analysis of main crack-microcrack interaction, Engineering fracture mechanics, 38, 451–465, https://doi.org/10.1016/0013-7944(91)90044-B, 1991.

Menegoni, N., Manna, L., Maino, M., and Perotti, C.: Finite element analysis of early deformations of carbonate platforms driven by differential compaction of basinal unit, Basin Res., 36, e12903, https://doi.org/10.1111/bre.12903, 2024.

Milnes, A. G.: Albert Heim's general theory of natural rock deformation (1878), Geology, 7, 99–103, https://doi.org/10.1130/0091-7613(1979)7%3C99:AHGTON%3E2.0.CO;2, 1979.

Miskovsky, K.: Effect of heat on the mechanical properties of selected rock types–a laboratory study, Harmonising Rock Engineering and the Environment, https://doi.org/10.1201/B11646-149, 2011.

Mitchell, T. M., and Faulkner, D. R.: The nature and origin of off-fault damage surrounding strike-slip fault zones with a wide range of displacements: A field study from the Atacama fault system, northern Chile, J. Struct. Geol., 31, 802–816, https://doi.org/10.1016/j.jsg.2009.05.002, 2009.

Moës, N., Dolbow, J., and Belytschko, T.: A finite element method for crack growth without remeshing, International journal for numerical methods in engineering, 46, 131–150, https://doi.org/10.1002/(SICI)1097-0207(19990910)46:1<131::AID-NME671>3.0.CO;2-J, 1999.

Moir, H., Lunn, R. J., Shipton, Z. K., and Kirkpatrick, J. D.: Simulating brittle fault evolution from networks of pre-existing joints within crystalline rock, J. Struct. Geol., 32, 1742–1753, https://doi.org/10.1029/2007JB005388, 2010.

Moore, D. E., and Lockner, D. A.: The role of microcracking in shear-fracture propagation in granite, J. Struct. Geol., 17, 95–114, https://doi.org/10.1038/350039a0, 1995.

https://doi.org/10.5194/egusphere-2026-4027
Preprint. Discussion started: 6 August 2026

Mueller, P., Tamburelli, S., Menegoni, N., Perozzo, M., Amadori, C., Crispini, L., ... and Maino, M.: Concurrence of load-and-flame structures, balls-and-pillows, clastic injectites and shear deformation bands as indicator of seismicity in mixed siliciclastic-carbonate successions (Finale Ligure Basin, Italy), Mar. Pet. Geol., 155, 106345, https://doi.org/10.1016/j.marpetgeo.2023.106345, 2023.

Myer, L. R.: Fractures as collections of cracks, Int. J. Rock Mech. Min. Sci., 37, 231–243, https://doi.org/10.1016/S1365-1609(99)00103-3, 2000.

Nabavi, S. T., Alavi, S. A., Mohammadi, S., Ghassemi, M. R., and Frehner, M.: Analysis of transpression within contractional fault steps using finite-element method, J. Struct. Geol., 96, 1–20, https://doi.org/10.1016/j.jsg.2017.01.004, 2017.

Nemat-Nasser, S., and Horii, H.: Compression-induced nonplanar crack extension with application to splitting, exfoliation, and rockburst, J. Geophys. Res.-Solid Earth, 87, 6805–6821, 1982.

Nevitt, J. M.: Fault-Related Deformation within the Brittle-Ductile Transition: Field Observations, Microstructural Analysis and Mechanical Modeling, Stanford University, http://purl.stanford.edu/nd893sm0307, 2015.

Nevitt, J. M., Pollard, D. D., and Warren, J. M.: Evaluation of transtension and transpression within contractional fault steps: Comparing kinematic and mechanical models to field data, J. Struct. Geol., 60, 55–69, https://doi.org/10.1016/j.jsg.2013.12.011, 2014.

Nicholson, R., and Pollard, D. D.: Dilation and linkage of echelon cracks, J. Struct. Geol., 7, 583–590, https://doi.org/10.1016/0191-8141(85)90030-6, 1985.

Nicksiar, M., and Martin, C. D.: Crack initiation stress in low porosity crystalline and sedimentary rocks, Eng. Geol., 154, 64–76, https://doi.org/10.1016/j.enggeo.2012.12.007, 2013.

Niu, Z., Wang, X., Zhang, L., Wang, J., Chang, Z., Qian, C., and Chen, X.: Investigation into the failure characteristics and mechanism of rock with single elliptical defects under ultrasonic vibrations, Fractal Fract., 8, 261, https://doi.org/10.3390/fractalfract8050261, 2024.

https://doi.org/10.5194/egusphere-2026-4027
Preprint. Discussion started: 6 August 2026

Nunes, K., Quevedo, R., Roehl, D., and Carvalho, B. R.: Assessment of linking damage zones of geological faults through numerical modeling, J. Struct. Geol., 195, 105381, https://doi.org/10.1016/j.jsg.2025.105381, 2025.

Nur, A.: The origin of tensile fracture lineaments, J. Struct. Geol., 4, 31–40, https://doi.org/10.1016/0191-8141(82)90004-9, 1982.

Obreimoff, J. W.: The splitting strength of mica, P. R. Soc. Lond. A, 127, 290–297, https://doi.org/10.1098/rspa.1930.0058, 1930.

Orowan, E.: Fracture and strength of solids, Reports on Progress in Physics, 12, https://doi.org/10.1088/0034-4885/12/1/309 185, 1949.

Osborne, M. J., and Swarbrick, R. E.: Mechanisms for generating overpressure in sedimentary basins: A reevaluation, AAPG Bull., 81, 1023–1041, https://doi.org/10.1306/522B49C9-1727-11D7-8645000102C1865D, 1997.

Paterson, M. S., and Wong, T. F.: Experimental Rock Deformation: the Brittle Field (Vol, 348). Berlin: Springer, https://doi.org/10.1016/0148-9062(82)91631-8, 2005.

Peacock, D. C. P., and Sanderson, D. J.: Pull-aparts, shear fractures and pressure solution, Tectonophysics, 241, 1–13, https://doi.org/10.1016/0040-1951(94)00184-B, 1995.

Peacock, D. C. P., and Sanderson, D. J.: Effects of propagation rate on displacement variations along faults, J. Struct. Geol., 18, 311–320, https://doi.org/10.1016/S0191-8141(96)80052-6, 1996.

Peacock, D. C. P., Nixon, C. W., Rotevatn, A., Sanderson, D. J., and Zuluaga, L. F.: Interacting faults, J. Struct. Geol., 97, 1–22, https://doi.org/10.1016/j.jsg.2017.02.008, 2017.

Peacock, D. C. P., Nixon, C. W., Rotevatn, A., Sanderson, D. J., and Zuluaga, L. F.: Glossary of fault and other fracture networks, J. Struct. Geol., 92, 12–29, https://doi.org/10.1016/j.jsg.2016.09.008, 2016.

https://doi.org/10.5194/egusphere-2026-4027
Preprint. Discussion started: 6 August 2026

Perozzo, M., Menegoni, N., Foletti, M., Poggi, E., Benedetti, G., Carretta, N., ... and Maino, M.: Evaluation of an innovative, open-source and quantitative approach for the kinematic analysis of rock slopes based on UAV based Digital Outcrop Model: A case study from a railway tunnel portal (Finale Ligure, Italy), Eng. Geol., 340, 107670, https://doi.org/10.1016/j.enggeo.2024.107670, 2024.

Petit, J. P., and Barquins, M.: Can natural faults propagate under mode II conditions?, Tectonics, 7, 1243–1256, https://doi.org/10.1016/0148-9062(89)90987-x, 1988.

Pollard, D. D.: Theoretical displacements and stresses near fractures in rock: with applications to faults, joints, veins, dikes, and solution surfaces, Fracture mechanics of rock, 277-349, https://doi.org/10.1016/B978-0-12-066266-1.50013-2, 1987.

Pollard, D. D., and Fletcher, R. C.: Fundamentals of Structural Geology, Cambridge University Press, https://www.cambridge.org/core/books/fundamentals-of-structural-geology/preface/6048A69964742D63FB376A4C9E50C5A2, 2005.

Pollard, D. D., Segall, P. A. U. L., and Delaney, P. T.: Formation and interpretation of dilatant echelon cracks, Geol. Soc. Am. Bull., 93, 1291–1303, https://doi.org/10.1130/0016-7606(1982)93%3C1291:FAIODE%3E2.0.CO;2, 1982.

Price, N. J.: Brittle fracture, Fault and Joint Development in Brittle and Semi-brittle Rock, 2, 1–56, https://doi.org/10.1016/C2013-0-05410-2, 1966.

Ramsey, J. M., and Chester, F. M.: Hybrid fracture and the transition from extension fracture to shear fracture, Nature, 428, 63–66, https://doi.org/10.1038/nature02333, 2004.

Reches, Z. E., and Lockner, D. A.: Nucleation and growth of faults in brittle rocks, J. Geophys. Res.-Solid Earth, 99, 18159–18173, https://doi.org/10.1038/350039a0, 1994.

Renard, F., Cordonnier, B., Kobchenko, M., Kandula, N., Weiss, J., and Zhu, W.: Microscale characterization of rupture nucleation unravels precursors to faulting in rocks, Earth Planet. Sci. Lett., 476, 69–78, https://doi.org/10.1016/j.epsl.2017.08.002, 2017.

https://doi.org/10.5194/egusphere-2026-4027
Preprint. Discussion started: 6 August 2026

Renard, F., Weiss, J., Mathiesen, J., Ben-Zion, Y., Kandula, N., and Cordonnier, B.: Critical evolution of damage toward system-size failure in crystalline rock, J. Geophys. Res.-Solid Earth, 123, 1969–1986, https://doi.org/10.1002/2017JB014964, 2018.

Resor, P. G., and Flodin, E. A.: Forward modeling synsedimentary deformation associated with a prograding steep-sloped carbonate margin, J. Struct. Geol., 32, 1187–1200, https://doi.org/10.1016/j.jsg.2009.04.015, 2010.

Rice, J. R.: A path independent integral and the approximate analysis of strain concentration by notches and cracks (No, ARPAE39), https://doi.org/10.1115/1.3601206, 1968.

Rodgers, D. A.: Analysis of pull-apart basin development produced by en echelon strike-slip faults, Sedimentation in oblique-slip mobile zones, 27-41, https://doi.org/10.1002/9781444303735.ch3, 1980.

Roering, C.: The geometrical significance of natural en-echelon crack-arrays, Tectonophysics, 5, 107–123, https://doi.org/10.1016/0040-1951(68)90084-X, 1968.

Rothery, E.: En échelon vein array development in extension and shear, J. Struct. Geol., 10, 63–71, https://doi.org/10.1016/0191-8141(88)90128-9, 1988.

Sánchez-Roa, C., Faulkner, D. R., boulton, C., Jimenez-Millan, J., and Nieto, F.: How phyllosilicate mineral structure affects fault strength in Mg-rich fault systems, Geophys. Res. Lett., 44, 5457–5467, https://doi.org/10.1002/2017GL073055, 2017.

Sanderson, D. J., and Nixon, C. W.: The use of topology in fracture network characterization, J. Struct. Geol., 72, 55–66, http://dx.doi.org/10.1016/j.jsg.2015.01.005, 2015.

Sanderson, D. J., and Peacock, D. C.: Measurement of geometry and linkage in vein arrays, J. Struct. Geol., 118, 104–113, https://doi.org/10.1016/J.JSG.2018.10.001, 2019.

Savage, H. M., and Cooke, M. L.: Unlocking the effects of friction on fault damage zones, J. Struct. Geol., 32, 1732–1741, https://doi.org/10.1016/j.jsg.2009.08.014, 2010.

https://doi.org/10.5194/egusphere-2026-4027
Preprint. Discussion started: 6 August 2026

Schmid, D. W., and Podladchikov, Y. Y.: Analytical solutions for deformable elliptical inclusions in general shear, Geophys. J. Int., 155, 269–288, https://doi.org/10.1046/j.1365-246X.2003.02042.x, 2003.

Schmittbuhl, J., Delaplace, A., Måløy, K. J., Perfettini, H., and Vilotte, J. P.: Slow crack propagation and slip correlations, Pure Appl. Geophys., 160, 961–976, https://doi.org/10.1007/PL00012575, 2003.

Scholz, C. H.: The frequency-magnitude relation of microfracturing in rock and its relation to earthquakes, Bull. Seismol. Soc. Am., 58, 399–415, https://doi.org/10.1785/BSSA0580010399, 1968.

Scholz, C. H.: The Mechanics of Earthquakes and Faulting, Cambridge University Press, https://doi.org/10.1017/9781316681473, 2019.

Segall, P., and Pollard, D. D.: Mechanics of discontinuous faults, J. Geophys. Res.-Solid Earth, 85, 4337–4350, https://doi.org/10.1029/JB085iB08p04337, 1980.

Segall, P., and Pollard, D. D.: Nucleation and growth of strike slip faults in granite, J. Geophys. Res.-Solid Earth, 88, 555–568, https://doi.org/10.1029/JB088iB01p00555, 1983.

Seyum, S., and Pollard, D. D.: The mechanics of intersecting echelon veins and pressure solution seams in limestone, J. Struct. Geol., 89, 250–263, https://doi.org/10.1016/j.jsg.2016.06.009, 2016.

Shewchuk, J. R.: Triangle: Engineering a 2D quality mesh generator and Delaunay triangulator, in: Workshop on Applied Computational Geometry 203–222 Berlin, Heidelberg: Springer Berlin Heidelberg, https://doi.org/10.1007/BFb0014497, 1996.

Shewchuk, J. R.: Delaunay refinement algorithms for triangular mesh generation, Comput. Geom., 22, 21–74, https://doi.org/10.1016/S0925-7721(01)00047-5, 2002.

Shipton, Z. K., and Cowie, P. A.: Damage zone and slip-surface evolution over µm to km scales in high-porosity Navajo sandstone, Utah, J. Struct. Geol., 23, 1825–1844, https://doi.org/10.1016/S0191-8141(01)00035-9, 2001.

https://doi.org/10.5194/egusphere-2026-4027
Preprint. Discussion started: 6 August 2026

Shipton, Z. K., and Cowie, P. A.: A conceptual model for the origin of fault damage zone structures in high-porosity sandstone, J. Struct. Geol., 25, 333–344, https://doi.org/10.1016/s0191-8141(02)00037-8, 2003.

Sibson, R. H.: Fault rocks and fault mechanisms, J. Geol. Soc. London, 133, 191–213, https://doi.org/10.1144/gsjgs.133.3.0191, 1977.

Sibson, R. H.: Earthquakes and rock deformation in crustal fault zones, Annual Review of Earth and Planetary Sciences, Vol. 14, p. 149, 14, 149, https://doi.org/10.1146/annurev.ea.14.050186.001053, 1986.

Siegmund, T., Fleck, N. A., and Needleman, A.: Dynamic crack growth across an interface, Int. J. Fract., 85, 381–402, https://doi.org/10.1023/A:1007460509387, 1997.

Stanchits, S., Vinciguerra, S., and Dresen, G.: Ultrasonic velocities, acoustic emission characteristics and crack damage of basalt and granite, Pure Appl. Geophys., 163, 975–994, https://doi.org/10.1007/s00024-006-0059-5, 2006.

Strijker, G., Beekman, F., Bertotti, G., and Luthi, S. M.: FEM analysis of deformation localization mechanisms in a 3-D fractured medium under rotating compressive stress orientations, Tectonophysics, 593, 95–110, https://doi.org/10.1016/j.tecto.2013.02.031, 2013.

Sylvester, A. G.: Strike-slip faults, Geol. Soc. Am. Bull., 100, 1666–1703, https://doi.org/10.1130/0016-7606(1988)100%3C1666:SSF%3E2.3.CO;2, 1988.

Tal, Y., Hager, B. H., and Ampuero, J. P.: The effects of fault roughness on the earthquake nucleation process, J. Geophys. Res.-Solid Earth, 123, 437–456, https://doi.org/10.1002/2017JB014746, 2018.

Tang, C. A., Lin, P., Wong, R. H. C., and Chau, K. T.: Analysis of crack coalescence in rock-like materials containing three flaws–Part II: Numerical approach, Int. J. Rock Mech. Min. Sci., 38, 925–939, https://doi.org/10.1016/S1365-1609(01)00064-8, 2001.

Tapponnier, P., and Brace, W. F.: Development of stress-induced microcracks in Westerly granite, in: International Journal of Rock Mechanics and Mining Sciences & Geomechanics Abstracts (vol. 13, no. 4, 103–112, https://doi.org/10.1016/0148-9062(76)91947-7, 1976.

https://doi.org/10.5194/egusphere-2026-4027
Preprint. Discussion started: 6 August 2026

Tesei, T., Collettini, C., Carpenter, B. M., Viti, C., and Marone, C.: Frictional strength and healing behavior of phyllosilicate-rich faults, J. Geophys. Res.-Solid Earth, 117, https://doi.org/10.1029/2012JB009216, 2012.

Thatcher, W.: Strain accumulation and release mechanism of the 1906 San Francisco earthquake, J. Geophys. Res., 80, 4862–4872, https://doi.org/10.1029/JB080i035p04862, 1975.

Twiss, R. J., and Moores, E. M.: Structural geology, Macmillan, ISBN-10: 0716722526, 1992.

Van der Pluijm, B. A. and Marshak, S.: Earth structure: an introduction to structural geology and tectonics, W. W. Norton, New York, USA, ISBN-10: 039392467X, 2004.

Vermilye, J. M., and Scholz, C. H.: The process zone: A microstructural view of fault growth, J. Geophys. Res.-Solid Earth, 103, 12223–12237, https://doi.org/10.1029/98JB00334, 1998.

Volpe, G., Pozzi, G., Carminati, E., Barchi, M. R., Scuderi, M. M., Tinti, E., ... and Collettini, C.: Frictional controls on the seismogenic zone: Insights from the Apenninic basement, Central Italy, Earth Planet. Sci. Lett., 583, 117444, https://doi.org/10.1016/j.epsl.2022.117444, 2022.

Westaway, R.: Deformation around stepovers in strike-slip fault zones, J. Struct. Geol., 17, 831–846, https://doi.org/10.1016/0191-8141(94)00104-E, 1995.

Wibberley, C. A. J., Yielding, G., and Di Toro, G.: Recent advances in the understanding of fault zone internal structure: a review, Geol. Soc. London Spec. Publ., 299, 5–33, https://doi.org/10.1144/SP299.2, 2008.

Willemse, E. J.: Segmented normal faults: Correspondence between three-dimensional mechanical models and field data, J. Geophys. Res.-Solid Earth, 102, 675–692, https://doi.org/10.1029/96JB03100, 1997.

Willemse, E. J., Pollard, D. D., and Aydin, A.: Three-dimensional analyses of slip distributions on normal fault arrays with consequences for fault scaling, J. Struct. Geol., 18, 295–309, https://doi.org/10.1016/S0191-8141(96)80051-4, 1996.

https://doi.org/10.5194/egusphere-2026-4027
Preprint. Discussion started: 6 August 2026

Wilson, J. E., Chester, J. S., and Chester, F. M.: Microfracture analysis of fault growth and wear processes, Punchbowl Fault, San Andreas system, California, J. Struct. Geol., 25, 1855–1873, https://doi.org/10.1016/S0191-8141(03)00037-2, 2003.

Wiltschko, D. V., Lambert, G. R., and Lamb, W.: Conditions during syntectonic vein formation in the footwall of the Absaroka Thrust Fault, Idaho–Wyoming–Utah fold and thrust belt, J. Struct. Geol., 31, 1039–1057, https://doi.org/10.1016/j.jsg.2009.06.012, 2009.

Winn, K., Ng, M., and Wong, L. N. Y.: Stability analysis of underground storage cavern excavation in Singapore, Procedia Eng., 191, 1040–1047, https://doi.org/10.1016/j.proeng.2017.05.277, 2017.

Wong, R. H. C., Chau, K. T., Tang, C. A., and Lin, P.: Analysis of crack coalescence in rock-like materials containing three flaws–part I: experimental approach, Int. J. Rock Mech. Min. Sci., 38, 909–924, https://doi.org/10.1016/S1365-1609(01)00064-8, 2001.

Wong, T. F.: Micromechanics of faulting in Westerly granite, in: International journal of rock mechanics and mining sciences & geomechanics abstracts (vol. 19, no. 2, 49–64 Pergamon, https://doi.org/10.1016/0148-9062(82)91631-8, 1982.

Woodcock, N. H., and Fischer, M.: Strike-slip duplexes, J. Struct. Geol., 8, 725–735, https://doi.org/10.1016/0191-8141(86)90021-0, 1986.

Woodcock, N. H., and Schubert, C.: Continental strike-slip tectonics, in: Continental deformation 251–263, ISBN-10: 0080379311, 1994.

Yang, C. H., and Soh, A. K.: Modeling of voids/cracks and their interactions, Theor. Appl. Fract. Mec., 38, 81–101, https://doi.org/10.1016/S0167-8442(02)00111-9, 2002.

Zhang, Y., Jiang, Y., Asahina, D., and Wang, Z.: Structural effect of en-echelon fractures on shear behavior of rock mass under constant normal load conditions: an experimental study, Rock Mech. Rock Eng., 54, 4825–4849, https://doi.org/10.1007/s00603-021-02555-3?urlappend=%3Futm_source%3Dresearchgate.net%26utm_medium%3Darticle, 2021.

https://doi.org/10.5194/egusphere-2026-4027
Preprint. Discussion started: 6 August 2026

Zhao, H., Wang, X., Liu, Z., Yan, Y., and Yang, H.: Investigation on the hydraulic fracture propagation of multilayers-commingled fracturing in coal measures, J. Pet. Sci. Eng., 167, 774–784, https://doi.org/10.1016/S0167-8442(02)00111-9, 2018.

Zhou, X. P., Bi, J., and Qian, Q. H.: Numerical simulation of crack growth and coalescence in rock-like materials containing multiple pre-existing flaws, Rock Mech. Rock Eng., 48, 1097–1114, https://doi.org/10.1007/s00603-014-0657-2, 2015.

Zoback, M. D., and Byerlee, J. D.: Effect of high-pressure deformation on permeability of Ottawa sand, AAPG Bull., 60, 1531–1542, https://doi.org/10.1306/C1EA3798-16C9-11D7-8645000102C1865D, 1976.